The Search for Rare Non-hadronic B-meson Decays with Final-state Neutrinos using the *BABAR* Detector

Dana Lindemann

Doctor of Philosophy

Physics Department

McGill University

Montréal, Québec

April 2012

A thesis submitted to McGill University in partial fulfillment of the requirements of the degree of Doctor of Philosophy.

ACKNOWLEDGEMENTS

I am grateful to the members of the *BABAR* Collaboration and the PEP-II staff for their dedicated years of work and service to provide the luminosity and detector quality that enables me to analyse a wealth of data in these analyses. I also thank my supervisor, Professor Steven Robertson, for all of his excellent guidance, knowledge, and advice with which he has provided me over the course of my schooling. In addition, I am grateful to Paul Mercure, for his knowledgeable and frequent computing help; Malachi Schram, for the many fun and helpful conversations on our analyses; Miika Klemetti, whose code was an invaluable reference for me when I first began my analyses; and Racha Cheaib, with whom it has been a pleasure to collaborate and share an office. I also thank the members of the Leptonic analysis working group, not only for developing and improving the hadronic-tag reconstruction algorithm, but also for all their feedback on my analyses — particularly Steven Sekula, Guglielmo DeNardo, Silke Nelson, Aidan Randle-Conde, and Owen Long. Thank you to my two review committees, consisting of Ingrid Ofte, Elisabetta Baracchini, David Hilton, Kevin Flood, and Francesca De Mori, for the amount of work and time they spent on reviewing and improving my results and publication. I am also grateful to my many colleagues in the SuperB Collaboration, who contributed to my appreciation of the considerations, challenges, and excitement involved in designing a B Factory. Finally, I thank Marc-André Gingras, for all of his support, patience, and kindness during my schooling. Also, I thank my parents, Mark and Vivian Lindemann, and my brother, Erik Lindemann, for their lifetime of love, encouragement, and confidence in all of my endeavours, including this one.

ABSTRACT

This thesis presents the searches for two rare B meson decays: the radiative leptonic decay $B^+ \to \ell^+ \nu_\ell \gamma$ ($\ell = e, \mu$) and the flavor-changing neutral current $B \to K^{(*)} \nu \overline{\nu}$. These searches use the full dataset collected by the BABAR experiment, which corresponds to almost 500 million $B\overline{B}$ pairs. After fully reconstructing the hadronic decay of one of the B mesons in $\Upsilon(4S) \to B\overline{B}$ decays, evidence of $B^+ \to \ell^+ \nu_\ell \gamma$ or $B \to K^{(*)} \nu \overline{\nu}$ is looked for in the rest of the event. No significant evidence of either signal decay is observed. Model-independent branching-fraction upper limits are set at $\mathcal{B}(B^+ \to e^+ \nu_e \gamma) < 17 \times 10^{-6}$, $\mathcal{B}(B^+ \to \mu^+ \nu_\mu \gamma) < 24 \times 10^{-6}$, and $\mathcal{B}(B^+ \to \ell^+ \nu_\ell \gamma) < 15.6 \times 10^{-6}$, all at the 90% confidence level. These are currently the most stringent published upper limits for $B^+ \to \ell^+ \nu_\ell \gamma$. In addition, branching-fraction upper limits are set at $\mathcal{B}(B^+ \to K^+ \nu \overline{\nu}) < 3.7 \times 10^{-5}$, $\mathcal{B}(B^0 \to K^0 \nu \overline{\nu}) < 8.0 \times 10^{-5}$, $\mathcal{B}(B^+ \to K^{*+} \nu \overline{\nu}) < 11.5 \times 10^{-5}$, and $\mathcal{B}(B^0 \to K^{*0} \nu \overline{\nu}) < 9.2 \times 10^{-5}$, all at the 90% confidence level. For additional sensitivity to New Physics contributions, partial $B \to K^{(*)} \nu \overline{\nu}$ branching-fraction upper limits are also determined over the full kinematic range.

ABRÉGÉ

Cette thèse présente l'étude de deux désintégrations rares de mésons B: la désintégration radiative leptonique $B^+ \to \ell^+\nu_\ell\gamma$ ($\ell = e, \mu$) et le courant neutre qui change la saveur $B \to K^{(*)}\nu\overline{\nu}$. Ces études utilisent l'ensemble des données recueuillies par l'expérience *BABAR* ce qui correspond à près de 500 millions paires $B\overline{B}$. Après la reconstruction totale de la désintégration hadronique de l'un des mésons B dans la désintégration $\Upsilon(4S) \to B\overline{B}$, la manifestation de $B^+ \to \ell^+\nu_\ell\gamma$ ou $B \to K^{(*)}\nu\overline{\nu}$ est recherché dans le reste de l'événement. Aucune preuve significative de la désintégration du signal n'a été observée. Les limites supérieures du rapport d'embranchement indépendantes du modèle sont évaluées à $\mathcal{B}(B^+ \to e^+\nu_e\gamma) < 17 \times 10^{-6}$, $\mathcal{B}(B^+ \to \mu^+\nu_\mu\gamma) < 24 \times 10^{-6}$, et $\mathcal{B}(B^+ \to \ell^+\nu_\ell\gamma) < 15,6 \times 10^{-6}$, à un niveau de confiance de 90%. Ce sont actuellement les limites supérieures les plus strictes publiés pour $B^+ \to \ell^+\nu_\ell\gamma$. De plus, les limites supérieure du rapport d'embranchement sont évaluées à $\mathcal{B}(B^+ \to K^+\nu\overline{\nu}) < 3,7 \times 10^{-5}$, $\mathcal{B}(B^0 \to K^0\nu\overline{\nu}) < 8,0 \times 10^{-5}$, $\mathcal{B}(B^+ \to K^{*+}\nu\overline{\nu}) < 11,5 \times 10^{-5}$, et $\mathcal{B}(B^0 \to K^{*0}\nu\overline{\nu}) < 9,2 \times 10^{-5}$, à un niveau de confiance de 90%. Pour demeurer réceptives aux contributions de la nouvelle physique, les limites supérieures du rapport d'embranchement partiel de $B \to K^{(*)}\nu\overline{\nu}$ sont déterminés dans le spectre cinématique complet.

TABLE OF CONTENTS

LIST OF TABLES

LIST OF FIGURES

CHAPTER 1
Introduction

Throughout the ages, humanity has searched for an ever-deeper understanding of the underlying structures and forces of the physical world. In recent centuries, matter was discovered to be built from molecules and atoms, which are now known to be made of subatomic particles: electrons, protons, and neutrons. The discovery of the electromagnetic force and the particle-wave duality of the photon soon followed. As the 20th century progressed, newer and more exotic particles were discovered, initially from the study of cosmic rays. Physicists sought to understand the relationship between these additional particles, their underlying structure, if they have any, and how they interact with each other. This quest has led particle physicists to design modern-day particle colliders that challenge our current limits of both technology and global collaboration, aiming for more precise measurements and ever higher particle-beam energies and luminosities. The study of particles and their interactions can provide a backward glimpse in time to the first seconds after the Big Bang, when all of the space, matter, and energy within the universe was formed. Thus, Particle Physics studies can offer an understanding of the underlying fabric of reality itself.

The *Standard Model* (SM) of Particle Physics was developed in the 1960–70's and is still today's most consistent and commonly accepted theory that successfully explains almost all of the experimental results in particle physics. In addition, as clean as the SM formulation is, there are some requirements that still lack adequate explanation. For example, the many input parameters needed in the SM, the large matter-antimatter asymmetry in the universe, the unaccounted cause of dark matter, and the huge difference in magnitudes between the realm of the gravitation force and that of the fundamental forces in the SM, are a few of the reasons why the SM is considered by many to be an incomplete part of a larger theory. Therefore, one aim of particle physics experiments is to precisely measure the SM parameters in order to look for deviations from the theoretically expected values that might indicate *New Physics*, a catch-all term describing any theoretical physics model or experimental evidence that is beyond the scope and/or predictions of the current Standard Model. Evidence of New Physics would hopefully be a directional guide for new experiments in order to address some of the most fundamental questions that remain unanswered about our universe.

This thesis is devoted to the search for two decay processes, $B^+ \to \ell^+\nu_\ell\gamma$ and $B \to K^{(*)}\nu\overline{\nu}$, that are predicted in the SM to be rare, occurring on the order of once in every one million B-meson decays. The goal of such analyses is to either observe evidence of the decays or to constrain their *branching fractions* ($\mathcal{B}$, the fraction of all decays which result in a specific final state). Both these searches use data collected by the *BABAR* experiment at the PEP-II e^+e^- collider in California.

The structure of this thesis is as follows. The thesis begins, in Chapter 2, with a theoretical introduction to the Standard Model, its particles, forces, and other relevant key features. Also in Chapter 2 is an overview of the $B^+ \to \ell^+\nu_\ell\gamma$ and $B \to K^{(*)}\nu\overline{\nu}$ analyses,[1] and the phenomenological theory that motivates the searches. Chapter 3 introduces the *BABAR* detector, its components, and the tools and techniques that are used to perform these rare B-decay searches. Chapter 4 discusses the full hadronic reconstruction of one of the two B mesons, which is employed in both the $B^+ \to \ell^+\nu_\ell\gamma$ and $B \to K^{(*)}\nu\overline{\nu}$ analyses. Chapter 5 describes in detail the analysis procedure for identifying the signal $B^+ \to \ell^+\nu_\ell\gamma$ decay, modeling the expected kinematics, estimating the background contribution, measuring the process in the data, and determining

[1]Charge conjugate modes are implied throughout this thesis, unless otherwise noted.

the systematic uncertainties associated with the measurement. Chapter 6 addresses the same aspects for the $B \to K^{(*)}\nu\overline{\nu}$ decay. Chapter 7 presents the conclusions of this thesis. A description of the author's personal contributions to the *BABAR* experiment and these analyses is provided in the Appendix.

CHAPTER 2
Analysis Motivations

2.1 Standard Model of Particle Physics

2.1.1 Overview

The Standard Model describes the known elementary particles that make up all the visible matter in the universe, the fundamental forces involved in their interaction via the exchange of force-carrying particles, and the mechanism that provides these particles with mass. It is built on a foundation of relativistic quantum field theory, which incorporates both the space-time structure of special relativity and the probabilistic framework of quantum mechanics. Within the SM, particles are mathematically represented as fields in space-time, and their interactions as *Lagrangian* (or dynamic-describing) functions of the fields and their first derivatives. Upon this foundation, a few common-sense constraints are added, namely *unitarity* (the sum of probabilities equals one), *locality and causality* (physical influence between two locally-independent points cannot travel faster than c, the speed of light), stability, and *renormalizability* (addresses a theory's predictive power above some minimum cut-off energy). The Standard Model also requires *Lorentz invariance* (conserved space-time quantities in different inertial reference frames) and local gauge symmetries, such that the Lagrangian remains invariant after various transformations. Just as a translation in space or time, which otherwise leaves a system unchanged, corresponds directly to the conservation of momentum or energy respectively [1], the conservation laws and resulting particles that naturally arise in the SM are also merely a result of its simple symmetries. For example, *Quantum Electrodynamics* (QED), the theory describing electromagnetism, can be expressed neatly as a quantum field theory with local gauge invariance under the symmetry group $U(1)$, a one-dimensional phase rotation.

Similarly, the SM, which incorporates QED, is based on $SU(3)_C \times SU(2)_L \times U(1)_Y$ gauge symmetries which leads to two fundamental SM interactions: the strong and electroweak interactions.[1] However, the symmetry is spontaneously broken by a non-zero-valued vacuum state of the scalar "Higgs" field, which is required in the SM to generate the masses of all the fundamental particles and to account for the differentiation of the electroweak force into the weak and electromagnetic forces at low energies.

2.1.2 Fundamental Particles in the Standard Model

In the SM, matter consists of twelve flavours of spin-1/2 *fermions*, including six *leptons* and six *quarks*. Quarks are defined as particles that can interact via the strong force, while leptons cannot. The fermions are categorized into three generations, consisting of a doublet of quarks and a doublet of leptons each. The properties of the particles are consistent between generations, except for their masses which increase between successive generations.[2] Each fermion has a corresponding antiparticle with the same mass and spin, but opposite *quantum numbers*, or quantities that are conserved during interactions, such as electric charge.[3] For example, the positron (e^+) is the antiparticle of the electron (e^-), and the $\overline{u}$-quark is the antiparticle of the u-quark. Fermions and anti-fermions can only be created or destroyed in pairs. The fermions interact with one another via the electromagnetic, weak, and strong forces

[1]The other fundamental force, gravity, is so weak that its effects are considered negligible at the scale of the current particle physics experiments, and therefore it is not included in the Standard Model.

[2]The mass hierarchy between the generations is not confirmed for neutrinos.

[3]A few quantum numbers, such as strangeness (the number of s-quarks minus $\overline{s}$-antiquarks) and parity (see Section 2.1.6), are not conserved in the weak interaction.

by exchanging spin-1 *gauge bosons*.[4] There are twelve gauge bosons, including the photon (γ), $W^{\pm}$ and Z^0 bosons, and eight gluons. The SM also predicts a spin-0 (or *scalar*) Higgs boson, which has yet to be discovered. Tables 2–1 and 2–2 list the fundamental particles of the SM.

Table 2–1: Summary of the measured properties of the SM fermions [2]. The three fermion generations are separated by horizontal lines, and the antiparticle states are implied via charge conjugation. The masses of the light quarks are approximate. Within the SM, neutrinos have a mass of exactly zero. However, although the exact masses of the neutrinos are poorly known, it is well-established from neutrino oscillation measurements that their masses are non-zero [3], which indicates physics beyond the SM.

Fermions (spin 1/2)

Quarks				Leptons			
Flavour	Symbol	Charge	Mass (GeV/c^2)	Flavour	Symbol	Charge	Mass (GeV/c^2)
up	u	2/3	0.0025	electron	e^-	-1	0.000511
down	d	$-1/3$	0.0050	e neutrino	ν_e	0	~ 0
charm	c	2/3	1.29	muon	μ^-	-1	0.1057
strange	s	$-1/3$	0.10	μ neutrino	ν_μ	0	~ 0
top	t	2/3	172.9	tau	τ^-	-1	1.777
bottom	b	$-1/3$	4.19	τ neutrino	ν_τ	0	~ 0

Table 2–2: Summary of the measured properties of the SM bosons [2]. The Higgs boson has not been conclusively observed yet, but upper and lower limits are set at 95% confidence level [4, 5, 6].

Gauge Bosons (spin 1)

Force	Mediator	Symbol	Charge	Mass (GeV/c^2)
Electromagnetic	photon	γ	0	0
Weak	W	$W^{\pm}$	± 1	80.4
	Z	Z^0	0	91.2
Strong	8 gluons	g	0	0
Scalar Bosons (spin 0)				
—	Higgs	H	0	> 115.5, < 127

[4]The spins of fermions and bosons are actually $\hbar/2$ and $\hbar$, respectively. However "natural units" are assumed in this thesis, in which $\hbar = 1$ and $c = 1$.

2.1.3 Electromagnetic Interaction

Charged fermions can interact with each other via the electromagnetic force, which is mediated by the exchange of virtual photons. *Virtual* particles are those that are spontaneously created from the vacuum, temporarily breaking the law of the conservation of energy, which can only occur if their interaction time is limited by $\Delta E \Delta t \approx \hbar$ of the uncertainty principle. Since the photon is massless, the electromagnetic force is said to have an infinite range. This is also because the potential of the electromagnetic force is proportional to $1/r^2$, such that as distance increases, the force decreases without reaching zero.

The strength of the electromagnetic interaction is specified by the coupling constant α:

$$\alpha \equiv \frac{ke^2}{\hbar c} \sim \frac{1}{137} \tag{2.1}$$

where e is the charge of a positron and k is Coulomb's constant. This small value allows for *perturbative* calculations (approximation techniques in which a single quantum exchange is often taken as the first order) to a very high precision, resulting in an excellent description of the electromagnetic interaction in the theory of QED.

2.1.4 Strong Interaction and Hadrons

In addition to electromagnetic charge, quarks also carry one of three "colour" charges and antiquarks carry one of the three "anti-colours". The gluon[5] couples to the color charge, resulting in the interaction between quarks via the strong force, as well as gluon self-interaction. *Quantum Chromodynamics* (QCD), the theory describing the strong interaction as an $SU(3)$ local symmetry group, has a potential of the form [7, 8]:

$$V = -\frac{4}{3}\frac{\alpha_s}{r} + kr \tag{2.2}$$

[5]There are actually eight gluons, each carrying a different combination of colour and anti-colour charges.

where $k \approx 1\,\mathrm{GeV/fm}$ and α_s is the coupling strength of the strong force, which ranges from about 0.1 to 1 depending on the energy scale.[6] At short distances, which corresponds to high energy scales, the first term dominates, so a single-gluon exchange is a good approximation and perturbative calculations are possible down to $\Lambda_{\mathrm{QCD}} \approx 250\,\mathrm{MeV}$ [2]. However, at large distances (low energy), where the second term dominates, the force actually increases as the distance increases. The strong force is said to have a range of about $10^{-15}\,\mathrm{m}$; if the distance between a quark-antiquark pair exceeds this distance, another quark-antiquark pair is spontaneously created out of the vacuum and binds to the initial quark-antiquark pair. Because of this, free and isolated quarks or gluons are not possible in QCD. Instead, quarks and gluons are always confined inside *hadrons*, which are color-neutral bound states of two or three quarks. A combination of three quarks or three antiquarks is called a *baryon*, such as the proton or neutron, and a quark-antiquark pair is called a *meson*. Table 2–3 provides a list of the mesons that are relevant to this thesis.

2.1.5 The Higgs Mechanism and the Weak Interaction

The local gauge symmetries on which the SM are built require that all fundamental particles are massless. However, as this is not the case in nature, the electroweak gauge symmetry must be spontaneously broken. This is achieved by the *Higgs Mechanism* [9], which proposes the existence of a scalar Higgs field which has a non-zero-valued vacuum state, determined to be approximately 246 GeV [2]. This additional field causes the electroweak neutral gauge bosons to mix with each other through a rotation of the weak-mixing angle (θ_W) resulting in four mass eigenstates: one neutral and massless (the photon), one neutral and massive (Z^0), and two charged and massive ($W^\pm$) gauge bosons. The weak-mixing angle relates the $W^\pm$ and Z^0 masses

[6] At the B-physics energy scales, the strong force coupling strength is typically between 0.2 to 0.5.

Table 2–3: Summary of the mesons most relevant to this thesis [2]. The antiparticle states are implied via charge conjugation. Both the K^+ and π^+ (which primarily decay to $\mu^+\nu_\mu$) are longer-lived particles that are directly detected by the *BABAR* detector, and are therefore listed as "stable" in the last column. The four listed $K^{(*)}$ particles are also called *kaons* and the π^+ and π^0 particles are called *pions*. The K^0_S meson is actually a mix of the K^0 and $\overline{K}^0$ mesons, and therefore its quark content is a mixture of both symmetric and asymmetric terms.

Symbol	Quark Content	Charge	Mass (GeV/c^2)	Lifetime (s)	Main Decay Modes
$\Upsilon(4S)$	$b\,\overline{b}$	0	10.579	3.21×10^{-23}	B^+B^-, $B^0\overline{B}^0$
B^+	$u\,\overline{b}$	+1	5.2791	1.64×10^{-15}	many
B^0	$d\,\overline{b}$	0	5.2795	1.52×10^{-15}	many
D^+	$\overline{d}\,c$	+1	1.8696	1.04×10^{-12}	many
D^0	$\overline{u}\,c$	0	1.8648	4.10×10^{-13}	many
K^+	$u\,\overline{s}$	+1	0.4937	1.24×10^{-8}	stable
K^0_S	$(d\overline{s} \pm \overline{d}s)/\sqrt{2}$	0	0.4976	8.95×10^{-11}	$\pi^+\pi^-$, $\pi^0\pi^0$
K^{*+}	$u\,\overline{s}$	+1	0.8917	1.30×10^{-23}	$K^+\pi^0$, $K^0_S\pi^+$
K^{*0}	$d\,\overline{s}$	0	0.8959	1.35×10^{-23}	$K^+\pi^-$, $K^0_S\pi^0$
π^+	$u\,\overline{d}$	+1	0.1396	2.60×10^{-8}	stable
π^0	$(u\overline{u} - d\overline{d})/\sqrt{2}$	0	0.1350	8.4×10^{-17}	$\gamma\gamma$
η	$(u\overline{u} + d\overline{d} - 2s\overline{s})/\sqrt{6}$	0	0.5479	5.06×10^{-19}	$\gamma\gamma$, $\pi^0\pi^0\pi^0$, $\pi^+\pi^-\pi^0$
ω	$(u\overline{u} + d\overline{d})/\sqrt{2}$	0	0.7827	7.75×10^{-23}	$\pi^+\pi^-\pi^0$
η'	$(u\overline{u} + d\overline{d} + s\overline{s})/\sqrt{3}$	0	0.9578	3.31×10^{-21}	$\pi^+\pi^-\eta$, $\pi^+\pi^-\gamma$, $\pi^0\pi^0\eta$

by $M_W = M_Z \cos\theta_W$, such that $\sin^2\theta_W \approx 0.231$ [2]. Although at high energies, the electromagnetic and weak forces are unified into a single electroweak interaction with $SU(2) \times U(1)$ local gauge symmetry [10], the symmetry breaking causes the electroweak interaction to manifest itself as two separate forces at lower energies. The two forces are related by the *weak hypercharge*, $Y_W = 2(Q - T_3)$, where Q is electric charge and T_3 is the third component of weak isospin, both of which are the conserved quantities associated with the electromagnetic and weak interactions, respectively.

All of the leptons and quarks are capable of interacting with each other via the weak force, which is carried by the Z^0 and $W^\pm$ bosons. For example, Figure 2–1 shows a Feynman diagram of an e^+e^- annihilating into a $b\bar{b}$ quark pair via a *tree-level* process, in which a single virtual gauge boson is exchanged. Unlike the massless photon, the weak gauge bosons are quite massive, so their creation during a weak interaction is significantly limited in time, due to the uncertainty principle. Therefore, the weak interaction has a short-range, limited to 10^{-18} m. The weak coupling strength, as mediated by the $W^{\pm}$ at low energies, can be written as [2]:

$$\frac{G_F}{\sqrt{2}} = \frac{e^2}{8\sin^2\theta_W M_W^2} \tag{2.3}$$

where G_F is the Fermi coupling constant and M_W is the mass of the $W^{\pm}$ boson. This weak coupling corresponds to a strength of about $\alpha \cdot 10^{-3}$, so unless a strong or electromagnetic force is forbidden in a given interaction, the weak force is often drowned out by these other two processes.

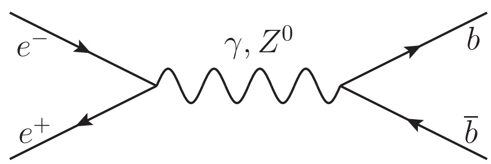

Figure 2–1: Feynman diagram of an $e^+e^- \to b\bar{b}$ process.

In addition, quarks and leptons interact with the Higgs field, described by *Yukawa couplings* (couplings of a scalar field to the left- and right-handed fermions). These couplings result in the existence of the fermion masses which are proportional to the vacuum expectation value of this field. The existence of quark masses enables the possibility of quark-flavour mixing, which will be discussed in the following section. The predicted Higgs field also implies the existence of the Higgs boson, a neutral spin-0 particle, which has not been conclusively observed.

2.1.6 CKM Matrix and CP Violation

Interactions involving a change in flavour, such as a b-quark transitioning to a u-quark, are only permitted via a charged-current weak interaction mediated by the $W^{\pm}$ boson. This curious phenomenon, known as *quark-mixing*, is possible because the quark mass eigenstates, which govern how physical particles propagate through space, are rotated with respect to their weak flavour eigenstates. In other words, the physical u- and d-quarks are seen within the charged-current weak interaction as actually mixtures of flavours. The coupling strengths between the six quarks are described using a 3×3 matrix of complex numbers, known as the *Cabbibo-Kobayashi-Maskawa* (CKM) matrix [11]:

$$V_{\text{CKM}} = \begin{pmatrix} V_{ud} & V_{us} & V_{ub} \\ V_{cd} & V_{cs} & V_{cb} \\ V_{td} & V_{ts} & V_{tb} \end{pmatrix} \tag{2.4}$$

such that the probabilities of down-type quarks (d,s,b) can be expressed in terms of their weak eigenstates (d',s',b') via:

$$\begin{pmatrix} d' \\ s' \\ b' \end{pmatrix} = V_{\text{CKM}} \begin{pmatrix} d \\ s \\ b \end{pmatrix} \tag{2.5}$$

This matrix can be described using four free parameters: three mixing angles and one complex phase. However, the only constraint naturally arising out of the SM is that the CKM matrix must be unitary ($(V_{\text{CKM}})^{\dagger} V_{\text{CKM}} = 1$), thus the actual value of these parameters must be determined experimentally. Experimental evidence shows that the magnitudes of the matrix elements decrease significantly as one moves further from the diagonal, and therefore these CKM parameters can be conveniently expressed using the Wolfenstein parametrization [12]:

$$V_{\text{CKM}} \approx \begin{pmatrix} 1 - \frac{\lambda_{\text{CKM}}^2}{2} & \lambda_{\text{CKM}} & A\lambda_{\text{CKM}}^3(\rho - i\eta) \\ -\lambda_{\text{CKM}} & 1 - \frac{\lambda_{\text{CKM}}^2}{2} & A\lambda_{\text{CKM}}^2 \\ A\lambda_{\text{CKM}}^3(1 - \rho - i\eta) & -A\lambda_{\text{CKM}}^2 & 1 \end{pmatrix} + O(\lambda_{\text{CKM}}^4) \tag{2.6}$$

where $\lambda_{\text{CKM}} \approx 0.225$ and $A \approx 8.0$ [2] have been relatively well-measured, while ρ and η, which correspond to the complex phase of the matrix, are less precisely measured. The matrix element $|V_{ub}| \approx |A\lambda_{\text{CKM}}^3(\rho - i\eta)|$, which describes the b-quark to u-quark coupling that occurs in the $B^+ \to \ell^+\nu_\ell\gamma$ decay, is the smallest of the elements at $(3.89 \pm 0.44) \times 10^{-3}$ [2].

Since the CKM matrix is required to be unitary, one can describe the relationship between the CKM matrix parameters as:

$$V_{ud}V_{ub}^* + V_{cd}V_{cb}^* + V_{td}V_{tb}^* = 0 \tag{2.7}$$

This relationship can be geometrically represented as a triangle in the complex plane, called the *Unitarity Triangle*, shown in Figure 2–2. Various particle decays can offer direct measurements of the angles and sides of the triangle, and thus one of the goals of the *BABAR* experiment is to determine these quantities redundantly through a variety of measurements. An inconsistency in any one measurement, compared with the triangular shape as determined from the other measurements, could be a clear indication of New Physics.

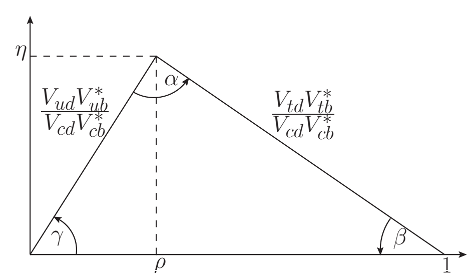

Figure 2–2: Unitarity Triangle of the CKM matrix, demonstrating the relationship between the CKM matrix elements.

The imaginary term in the CKM matrix has interesting implications on *charge-parity* (CP) symmetry, where charge and parity are two discrete symmetries, with time being a third. A charge operator (C) converts a particle into its antiparticle, by reversing not only the charge of the particle but also its other quantum numbers, although its spin orientation remains unchanged. A time operator (T) reverses the direction of the time component of a four-vector. A parity operator (P) causes the inversion of all three spatial coordinates; the four-vector of this process can be written as $P(x, y, z, t) = (-x, -y, -z, t)$. This causes an inversion in the particle's *handedness*, which is its spin orientation relative to its momentum. If the direction of a fermion (or anti-fermion) spin is in the same direction as its motion, it is considered right-handed; otherwise it is left-handed.

It is well-established that if the SM is Lorentz-invariant, it must be symmetric under the combination of all three discrete symmetries: CPT. In addition, both charge and parity are individually conserved in the strong and electromagnetic interactions, as originally was assumed to be the case for all the fundamental interactions. However, experiments have shown that the weak interaction only couples to left-handed fermions and right-handed anti-fermions, which maximally violates the parity symmetry. In addition, experimental evidence has also proven the violation of CP symmetry in the weak interaction [13], which can be quantified by the complex phase in the CKM matrix. Both C- and CP-violations are necessary conditions to explain the matter-antimatter asymmetry in the universe [14], although the measured size of CP-violation from quark-mixing is not adequate to account for the size of the observed amount of matter. Measuring the CP-violation in B-meson decays was the original purpose of the *BABAR* experiment.

2.1.7 Flavor-Changing Neutral Currents

Unlike the charged-current interaction, which can change one quark to another flavoured quark with differing electric charge, the neutral-current interaction mediated by the Z^0 boson is not permitted to change the flavour of the fermion at tree-level. However, at higher orders, loop processes exist, in which multiple virtual particles are produced and annihilated. Thus, effective *flavour-changing neutral currents* (FCNCs) are permitted, provided that they occur through one of these higher-order loops, in which a quark emits and re-absorbs a $W^{\pm}$ boson, thus changing flavour twice, as shown in the Feynman diagrams in Figure 2–3 which depict $B \to K^{(*)}\nu\overline{\nu}$ decays. Since the three possible quark flavours within a loop have differing masses, their individual loop contributions do not fully cancel, which is the reason that effective FCNCs are possible. In fact, the contributions from top quarks are significantly enhanced in such processes due to their enormous mass. Since FCNCs contain massive virtual particles within the loop, they are suppressed compared to tree-level processes, due to additional coupling constants and CKM matrix parameters. Thus, FCNC decays are relatively rare. However, New Physics particles could also enter into these loops and increase the expected branching fraction. In this way, even if these particles are sufficiently massive that they are out-of-reach at energy-frontier experiments, such as the LHC and Tevatron, measuring decays such as $B \to K^{(*)}\nu\overline{\nu}$ can provide alternative handles to study electroweak mixing and explore New Physics possibilities at higher mass scales.

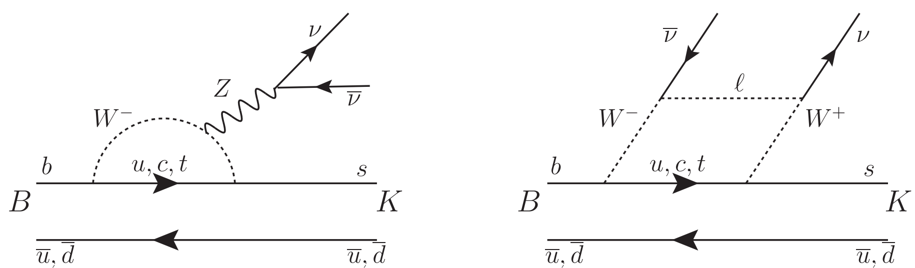

Figure 2–3: Feynman diagrams of $B \to K^{(*)}\nu\overline{\nu}$ decays via a (left) "penguin" loop and (right) "box" diagram.

2.1.8 Effective Field Theories

The precision measurements from the B Factories, like *BABAR*, are limited by the degree to which non-perturbative QCD effects can be controlled. Therefore, precision physics is characterized by a vibrant interplay and exchange between experiment and theory. The usefulness of measuring a given process is often contingent on the theoretical computations themselves, and are often used to compare and verify the use of various theoretical approximation techniques.

Quantum field theory requires that all possible virtual states be included in the calculation of an observable, including particles in higher-order loops, such as from self-interaction and from fermion-pair creation/annihilation. At low energy (large distances), these higher-order effects can become quite complex, particularly due to QCD corrections. Since these calculations often involve multiple energy scales due to the widely ranging particle masses, they can be exceedingly difficult to solve analytically. For example, B-meson physics is ultimately the study of the heavy b quark, which is surrounded by a complicated, strongly-interacting cloud of light quarks, antiquarks, and gluons. Therefore, B-meson decays typically consist of both short-distance electroweak interactions and long-distance QCD interactions. The short-distance interactions are conducive to analytic perturbative calculations, while the long-distance interactions must be estimated using non-perturbative numerical techniques such as QCD sum rules or lattice calculations. The Operator Product Expansion (OPE) offers a framework to conveniently separate out effects at various energy scales such that *Effective Field Theories* (EFTs) can be used at each energy scale by employing different theoretical approaches [15].

Using the uncertainty principle, a virtual particle of mass m can propagate a distance of $x \approx \hbar/mc$ before reabsorption, so if one assumes a resolution much greater than x, the exchange of the virtual particle is not distinguishable from a point-interaction. Thus, a cut-off energy scale Λ for an EFT is such that any particle more massive than this energy scale can be "integrated out" from the theory. This essentially removes the massive virtual intermediate states from the theory and leaves only the degrees of freedom relevant to the process at lowest orders, such as the initial- and final- state particles. To account for the removal of such particles, new "effective" interactions are introduced by Operator Product Expansion and renormalization group techniques, which factorize the short- and long-distance effects. Thus, the effective Lagrangian can be expressed as:

$$\mathcal{L}_{\text{eff}} = \sum_i \frac{c_i(\Lambda)}{\Lambda^{d_i-4}} \mathcal{O}_i \tag{2.8}$$

where $\mathcal{O}_i$ are local operators of dimension d_i, and c_i are complex dimensionless coefficients. Because operators with dimensions higher than four are suppressed by powers of $1/\Lambda$, the effective Lagrangian is often approximated for B physics by neglecting operators of dimensions higher than six.

Since most interactions at *BABAR* have momenta on the order of the B-meson mass, which is much less than M_W, B physics typically uses an energy scale of approximately $m_b \ll M_W$, where m_b is the b-quark mass. The massive electroweak gauge bosons can be factored out by setting a cut-off at $\Lambda = M_W$. The effective interactions, describing the $W^\pm$ exchange, can then be expressed in the form $\sum_{i=0}^{10} C_i(\mu)\mathcal{O}_i$ where μ is the four-momentum of the virtual $W^\pm$, $\mathcal{O}_i$ are local four-fermion (dimension-six) operators that contain the non-perturbative physics at scales lower than μ, and $C_i(\mu)$ are coupling constants, called *Wilson coefficients*, which contain the perturbative short-distance physics above μ [15].

Hadronic matrix elements (the mathematical description of a hadron's internal QCD interactions) are often evaluated at an even lower scale of approximately $\Lambda_{\rm QCD} \ll m_b$, in order to factor out the non-perturbative QCD corrections from the perturbative ones. The difficult-to-compute quantities that are based on non-perturbative QCD physics are encapsulated into functions called *form-factors*. Since the same underlying physics will often appear in similar processes, both these form-factors and the Wilson coefficients are defined such that they are process-independent and thus can be extracted from measurements of one process to make predictions in another.

2.1.9 Beyond the Standard Model

Although the Standard Model has been incredibly successful in accurately predicting and accounting for almost all of the experimental observations to date, the SM itself can be thought of as an EFT, with Λ at the electroweak scale of a few hundred GeV. New Physics, associated with some grander theory, would enter at a higher energy scale. In fact, this is largely believed to be the case, as there currently exist several limitations on the SM that have yet to be explained.

For example, the recently discovered neutrino oscillations[7] contradict the SM prediction that neutrinos are massless [3]. Since neutrinos have no electromagnetic or color charge, and the weak interaction couples only to left-handed fermions, right-handed neutrinos would not interact at all and are thus not included in the SM. This also results in neutrinos being massless. Therefore, the discovery of a neutrino mass hierarchy necessitates an extension of the current SM. One example of a theoretical possibility is the existence of very massive right-handed neutrinos [16].

In addition, the SM is somewhat ad-hoc, containing 19 input parameters[8] which are not derived from first principles, including particle masses, coupling constants, and mixing angles. One of these parameters is the mass of the predicted Higgs boson, which is currently unknown but is actively being sought. The mass is predicted to be at the same order as the vacuum expectation value ($\nu = (\sqrt{2}G_F)^{-1/2} \approx 246\,\mathrm{GeV}$) [2]. However, when higher-order contributions of massive particles are included in the calculations, such as a virtual top-quark creation/annihilation loop, the Higgs mass diverges. In order to maintain the expected Higgs mass around the electroweak scale, such that it is compatible with other SM constraints, a cancellation is required to almost 33 decimal places. This "fine-tuning" is considered unnatural, which suggests that New Physics might exist near the electroweak scale in order to account for such cancellations more naturally.

[7]Like quark mixing, the mixing between neutrino flavours can be described by a 3×3 matrix.

[8]This value assumes the original SM assumption that neutrinos are massless.

One such New Physics model, *Supersymmetry* (SUSY), is an extension of the SM with additional elementary particles paired with the currently known SM particles. The virtual contributions of these additional particles can reduce the fine-tuning problem of the Higgs mass. SUSY also suggests the possibility of a Grand Unified Theory since the coupling strength of the strong and electroweak interactions converge at a high energy, unlike in the current SM. Although there are many variations of SUSY, one of the most basic SUSY extensions is the *Minimal Supersymmetric Standard Model* (MSSM) [17], which serves as a benchmark for many experimental studies. MSSM requires the existence of two charged and two neutral spin-zero bosons in addition to the SM-predicted neutral Higgs boson, and predicts that every spin-1/2 quark and lepton has a spin-0 *squark* and *slepton* superpartner, respectively, and every integer-spin boson has an intuitively named spin-1/2 *chargino*, *neutralino*, or *gluino* superpartner.

SUSY also suggests a solution to another unexplained phenomenon. There is overwhelming astronomical evidence for *dark matter*, which does not interact via the electromagnetic force and is thus "invisible" [18]. Due to its interaction via the gravitational force, dark matter is known to be five times more populous in the universe than SM matter. Evidence also indicates that dark matter cannot interact via the strong force (if at all) with regular baryonic matter, and that it likely consists of massive particles, often called *Weakly Interacting Massive Particles* (WIMPs). However, no SM particle fits the dark matter description, which suggests that New Physics particles may exist. Many SUSY models predict the existence of a stable and massive particle that only interacts with the SM particles via the weak force, such as the lightest neutralino particle (χ_0) in the MSSM. Such particles are good candidates for dark-matter WIMPs, with the added bonus that they may be producible and indirectly detectable at particle physics colliders.

Finally, since quantum field theory has not been successfully combined with general relativity (the best physical model of gravity), the SM does not include the gravitational force. Within most particle physics experiments, this is of little concern, since the gravitational force is so small that it is negligible, but it nevertheless creates a significant hole in the SM theory.

2.2 Overview of Experimental Analyses

This thesis describes two separate but related B-meson decay studies of the processes $B^+ \to \ell^+\nu_\ell\gamma$ and $B \to K^{(*)}\nu\overline{\nu}$, where $\ell = e$ or μ. As neither process has ever been observed, limits on the branching fractions are determined. These analyses were performed using data collected at the BABAR detector at the SLAC National Accelerator Laboratory, in which large samples of B-meson pairs were produced. This was achieved by colliding electrons and positrons at the same energy as the mass of an $\Upsilon(4S)$ meson, such that this $b\overline{b}$ meson is formed through the process shown in Figure 2–1. An $\Upsilon(4S)$ meson almost always decays into a pair of B-mesons, either B^+B^- or $B^0\overline{B}^0$. These analyses fully reconstruct one of the two B mesons in any of a large number of hadronic decay modes, and then search for evidence of the signal B decays using the rest of the detected particles.

The $B^+ \to \ell^+\nu_\ell\gamma$ signal decays are identified by a single charged particle, consistent with either an electron or a muon, and a high-energy neutral particle consistent with a photon. The kinematics of the event must be consistent with the presence of an undetected massless neutrino produced within a three-body B meson decay. The $B \to K^{(*)}\nu\overline{\nu}$ signal decays are reconstructed in one of six channels, including $B^+ \to K^+\nu\overline{\nu}$, $B^0 \to K^0_S\nu\overline{\nu}$ (with $K^0_S \to \pi^+\pi^-$), and $B \to K^*\nu\overline{\nu}$ decays where K^* is reconstructed in four distinct modes. These decays are selected using charged particles that are identified as kaons or pions, and neutral-particle pairs that form π^0 candidates, all of which are used to reconstruct K^0_S and K^* candidates. In addition, the events must have *missing energy* within the event, or undetected energy that is known to be present due to both the conservation of energy and the summed energy of detected particles. Finally, the events are required to have little, if any, detected energy in the event that is not assigned to either of the two reconstructed B-meson decays.

The results of this $B^+ \to \ell^+\nu_\ell\gamma$ analysis, which were published in 2009 [19], are the most stringent published limits to-date. Prior to this, three searches for $B^+ \to \ell^+\nu_\ell\gamma$ had been performed, as outlined in Table 2–4, but only the results from the CLEO experiment have been published. In addition, the analysis described in this thesis is the first $B^+ \to \ell^+\nu_\ell\gamma$ search that has been performed using the hadronic-tag reconstruction method. By using this method, kinematic restrictions on the photon and lepton were able to be avoided, thus making these results the only model-independent limits for $B^+ \to \ell^+\nu_\ell\gamma$.

Table 2–4: Previously measured $B^+ \to \ell^+\nu_\ell\gamma$ branching-fraction upper limits at the 90% confidence level, not including the published results described in this thesis.

Collaboration	Year	$N_{B\bar{B}}$ pairs ($\times 10^6$)	$\mathcal{B}(B^+ \to e^+\nu_e\gamma)$ ($\times 10^{-6}$)	$\mathcal{B}(B^+ \to \mu^+\nu_\mu\gamma)$ ($\times 10^{-6}$)
CLEO [20]	1997	2.7	< 200	< 52
Belle [21]	2004	152	< 22	< 23
BABAR [22]	2006	232	< 3.8	

There have also been several published upper limits on $\mathcal{B}(B \to K^{(*)}\nu\overline{\nu})$, as outlined in Table 2–5. The results presented in this thesis provide an update to previous *BABAR* measurements. Particularly, an analysis of $B^0 \to K^0\nu\overline{\nu}$ using hadronic-tag reconstruction has never before been performed on the *BABAR* data, and the $B^+ \to K^+\nu\overline{\nu}$ measurement using hadronic tags was performed on less than one-fifth of the current *BABAR* dataset. One can potentially combine these updated hadronic-tag limits with those from the semileptonic-tag reconstruction (which is described in Section 4.1.1), since the two reconstruction methods produce essentially orthogonal datasets. Thus, an update to the hadronic-tag $B \to K\nu\overline{\nu}$ limits is important for obtaining the best possible limits from the full *BABAR* dataset. In addition, by providing partial branching fractions over the full kinematic range, the $B \to K^{(*)}\nu\overline{\nu}$ analysis described in this thesis is the first to be truly sensitive to New Physics distributions of the $B \to K^{(*)}\nu\overline{\nu}$ kinematics.

Table 2–5: Previously measured $B \to K^{(*)}\nu\overline{\nu}$ branching-fraction upper limits at the 90% confidence level. The "SL Tag" and "Had Tag" refer to semileptonic-tag and hadronic-tag analyses, respectively, which are fully described in Section 4.1.1. The results described in this thesis are not included.

Collaboration	Year	$N_{B\overline{B}}$ pairs ($\times 10^6$)	Tag	$\mathcal{B}(B \to K^+\nu\overline{\nu})$ ($\times 10^{-5}$)	$\mathcal{B}(B \to K^0_S\nu\overline{\nu})$ ($\times 10^{-5}$)	$\mathcal{B}(B \to K^{*+}\nu\overline{\nu})$ ($\times 10^{-5}$)	$\mathcal{B}(B \to K^{*0}\nu\overline{\nu})$ ($\times 10^{-5}$)
BABAR [23]	2005	89	SL	< 7	–	–	–
BABAR [23]	2005	89	Had	< 6.7	–	–	–
Belle [24]	2007	535	Had	< 1.4	< 16	< 14	< 34
BABAR [25]	2008	454	SL	–	–	< 9	< 18
BABAR [25]	2008	454	Had	–	–	< 21	< 11
BABAR [26]	2010	459	SL	< 1.3	< 5.6	–	–

2.3 $B^+ \to \ell^+\nu_\ell\gamma$ in the Standard Model

Leptonic decays of a B meson, which proceed via annihilation of the b- and u-quarks into a virtual $W^\pm$ boson, can provide direct experimental means of measuring SM parameters without the QCD-based uncertainties arising from hadrons in the final state. The purely leptonic decays $B^+ \to \ell^+\nu_\ell$ offer clean theoretical predictions of f_B, a form-factor known as the B-meson decay constant, which encapsulates the overlap of the quark wave-functions inside the B meson. This value ranges between 172–216 MeV, depending on the method of calculation [27, 28, 29, 30]. The SM branching fraction of $B^+ \to \ell^+\nu_\ell$ (and likewise $B^+ \to \tau^+\nu_\tau$) is given by:

$$\mathcal{B}(B^+ \to \ell^+\nu_\ell) = \frac{G_F^2}{8\pi}|V_{ub}|^2 f_B^2 m_B \tau_B m_\ell^2 \left(1 - \frac{m_\ell^2}{m_B^2}\right)^2 \tag{2.9}$$

where G_F is the Fermi coupling constant, m_B and m_ℓ are the masses of the B meson and lepton respectively, and τ_B is the B-meson lifetime. V_{ub} is the CKM matrix element that describes the coupling of b- and u-quarks and can be cleanly extracted from semileptonic B-meson decays, such as $B^+ \to \pi^0\ell^+\nu_\ell$. The branching fraction can also be enhanced or suppressed by New Physics particles such as a SUSY-model charged Higgs boson in place of the $W^\pm$ exchange.

However, the purely leptonic decay rate is suppressed by *helicity* (handedness), such that it has a branching fraction that is proportional to m_ℓ^2. This arises due to the fact that the B is a spin-zero meson, so when the ℓ^+ and ν_ℓ decay with opposite momentum in the W^+ rest frame, their spins are required to sum to zero to conserve the angular momentum of the B meson. Therefore, the helicities of both the final-state ℓ^+ antiparticle and ν_ℓ particle are left-handed, yet the weak-interacting $W^\pm$ boson only couples to left-handed particles and right-handed antiparticles. However, helicity depends on the reference frame of the observer, such that if an observer travels faster than a particle, it would appear to be moving backwards and thus with reversed helicity. Therefore, particles that are more massive and thus slower, such as the τ^+, are less helicity-suppressed than the lighter e^+. The SM branching fractions are predicted to be of the order 10^{-4}, 10^{-7}, and 10^{-11} for the tau, muon, and electron channels respectively. Only the $B^+ \to \tau^+ \nu_\ell$ decay has been observed at the current B factories [31, 32], although the short lifetime of the τ produces additional experimental challenges compared to the clean two-body final-states of $B^+ \to \ell^+\nu_\ell$, since τ decays produce at least one additional undetectable neutrino.

Although the radiative mode $B^+ \to \ell^+\nu_\ell\gamma$ is additionally suppressed by the electromagnetic coupling constant α, the presence of the photon can remove the helicity suppression. This is because the photon radiation can cause the production of a spin-one intermediate *off-shell* (or virtual) B state to which the $W^\pm$ boson couples directly [33]. The diagram in Figure 2–4 shows the dominant $B^+ \to \ell^+\nu_\ell\gamma$ decay, in which the photon couples to the light quark [34, 35], although a diagram in which the photon couples to the b-quark also contributes. The intermediate B state can correspond to either an off-shell vector (parity$= -1$) or an off-shell axial-vector (parity$= +1$) meson. The predicted branching fraction of $B^+ \to \ell^+\nu_\ell\gamma$, at an order of 10^{-6}, is larger than that of $B^+ \to \ell^+\nu_\ell$ ($\ell = \mathrm{e}, \mu$) and is independent of the lepton type.[9] Therefore, the radiative decay is potentially accessible at the current and future B Factories and, unlike in purely leptonic searches, the τ channel reconstruction can be avoided. A second "internal bremsstrahlung" scenario is also possible in $B^+ \to \ell^+\nu_\ell\gamma$ production, in which the photon is radiated off the final-state lepton. However, this is also helicity suppressed and therefore considered negligible at the current expected sensitivity of $B^+ \to \ell^+\nu_\ell\gamma$.

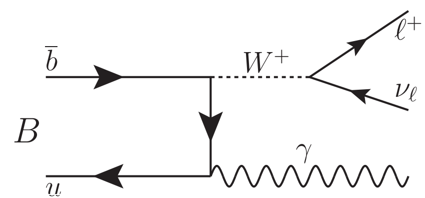

Figure 2–4: The dominant Feynman diagram of $B^+ \to \ell^+\nu_\ell\gamma$ decays.

Unfortunately, this otherwise clean three-body decay has additional theoretical uncertainties due to the non-perturbative strong-interaction physics within the hadronic matrix element. Although the uncertainties in the hadronic physics of $B^+ \to \ell^+\nu_\ell\gamma$ limit the extraction of SM quantities like f_B and V_{ub}, studying the $B^+ \to \ell^+\nu_\ell\gamma$ decays can serve as a probe of the underlying B-meson internal dynamics. Using factorization techniques, the tree-level hadronic matrix element can be written as:

$$\frac{m_B}{\sqrt{4\pi\alpha}}\langle\gamma|\overline{u}\gamma^\alpha(1-\gamma^5)b|B\rangle = f_V \varepsilon^{\alpha\beta\gamma\delta} v_\beta p_\gamma \epsilon^*_\delta + i f_A[\epsilon^{*\alpha}(v\cdot p) - p^\alpha(\epsilon^*\cdot v)] \tag{2.10}$$

where v_β is the B-meson four-velocity, p_γ is the four-momentum of the photon, ϵ^* is the polarization four-vector of the photon, and $E_\gamma = v \cdot p_\gamma$ is the energy of the

[9]The branching fraction of $B^+ \to \tau^+\nu_\tau\gamma$ would actually be slightly lower due to phase-space suppression.

radiated photon in the B-meson rest frame. The form-factors f_V and f_A contain the long-distance contributions of the vector and axial-vector currents, respectively, in the $B \to \gamma$ coupling, and are inversely proportional to E_γ. The differential branching fraction of $B^+ \to \ell^+\nu_\ell\gamma$ versus E_γ can be written in terms of the form-factors as:

$$\frac{d\mathcal{B}(B^+ \to \ell^+\nu_\ell\gamma)}{dE_\gamma} = \frac{\alpha G_F^2}{48\pi^2}|V_{ub}|^2 m_B^4 \tau_B \left[f_A^2(E_\gamma) + f_V^2(E_\gamma)\right] x(1-x)^3 \tag{2.11}$$

where $x \equiv 1 - 2E_\gamma/m_B$ such that x is between 0 and 1. Although most models conclude that $f_A = f_V$, some models predict $f_A = 0$ [36], while others predict a small difference between the two form-factors at higher orders [37]. Unfortunately, this results in model-dependent distributions of the predicted photon energy in $B^+ \to \ell^+\nu_\ell\gamma$ decays, which will be discussed further in Section 5.2.1.

The differential branching fraction is theoretically uncertain for soft photons with energies below $\Lambda_{\mathrm{QCD}} \approx 250\,\mathrm{MeV}$ [38]. However, at leading order for the tree-level process in the kinematical region $E_\gamma \gg \Lambda_{\mathrm{QCD}}$, Equation (2.11) can be integrated as [38]:

$$\mathcal{B}(B^+ \to \ell^+\nu_\ell\gamma) = \frac{\alpha G_F^2}{288\pi^2}|V_{ub}|^2 f_B^2 m_B^5 \tau_B \left(\frac{Q_u}{\lambda_B} - \frac{Q_b}{m_b}\right)^2 \tag{2.12}$$

where Q_i is the quark charge and λ_B is the first inverse moment of the B-meson distribution amplitude. The B-meson distribution amplitude, Φ_{B^+}, is a non-perturbative quantity that describes the probability amplitudes of finding the B meson in its valence "Fock" state of quark-antiquark with small transverse separation. The first moment of this distribution amplitude is perhaps the most relevant for B physics, especially at low order, which is defined as [39]:

$$\lambda_B^{-1} = \int_0^\infty \frac{d\omega}{\omega}\Phi_{B^+}(\omega) \tag{2.13}$$

where ω is the momentum carried by the light spectator quark, in this case the u-quark.

The B-meson distribution amplitude is a universal quantity that presents itself in many decays. For example, λ_B also enters into calculations of the $B \to \pi$ form-factor at high pion energies, such as in $B \to \pi \ell \nu_\ell$ decays, and into the branching fractions of two-body hadronic B-meson decays, such as $B \to D\pi$ and $B \to \pi\pi$ [40], the latter being a benchmark channel for measuring the angle α of the CKM Unitarity Triangle. However, the value of λ_B currently suffers from significant theoretical uncertainty, with estimates ranging from 150–700 MeV [41, 40, 42, 43]. Therefore, a tighter constraint on λ_B is vital for improved theoretical descriptions of such decays. In addition, measuring the value of λ_B can prove and improve QCD factorization theory itself [44]. Measuring $B^+ \to \ell^+ \nu_\ell \gamma$ is probably the cleanest way to access this parameter. In addition, since $B^+ \to \ell^+ \nu_\ell \gamma$ is a possible background for $B^+ \to \ell^+ \nu_\ell$, a measurement of $\mathcal{B}(B^+ \to \ell^+ \nu_\ell \gamma)$ over the full photon energy spectrum is needed for an accurate measurement of $\mathcal{B}(B^+ \to \ell^+ \nu_\ell)$ [45], which would consequently improve the measurements of f_B.

Depending on the method of calculation and the values used for $|V_{ub}|$, f_B, and λ_B, as well as the method used to approximate the form-factors, the predicted SM branching fraction for $B^+ \to \ell^+ \nu_\ell \gamma$ varies greatly, ranging between 0.32×10^{-6} and 5×10^{-6} [39, 38, 34, 36, 46]. Rate enhancements or suppressions from New Physics, similar to those suggested for $B^+ \to \ell^+ \nu_\ell$, could be possible in the $B^+ \to \ell^+ \nu_\ell \gamma$ decay. However, the relative enhancement would be harder to detect since $B^+ \to \ell^+ \nu_\ell \gamma$ lacks the helicity suppression that characterizes $B^+ \to \ell^+ \nu_\ell$, and the uncertainty on λ_B limits the sensitivity to New Physics that can be obtained from a $B^+ \to \ell^+ \nu_\ell \gamma$ branching fraction measurement. Therefore, the literature for $B^+ \to \ell^+ \nu_\ell \gamma$ offers no additional New Physics possibilities, but rather focuses on the role that this decay can play in improving theoretical approximation techniques and SM parameter measurements.

2.4 $B \to K^{(*)}\nu\overline{\nu}$ in the Standard Model and Beyond

Since FCNCs are prohibited in the SM at tree-level, the rare decays $B \to K^{(*)}\nu\overline{\nu}$ can only occur either via penguin diagrams, with a radiating virtual Z^0 boson, or via one-loop box diagrams, with two virtual $W^{\pm}$ bosons. Both of these diagrams are dominated by a top-quark exchange, and are shown in Figure 2–3. Therefore, the branching fractions of these decays are suppressed by the off-diagonal CKM matrix element, V_{ts}, describing the t- to s-quark transition. The SM branching fractions for $B \to K\nu\overline{\nu}$ are predicted to be between $(3.6 \pm 0.47) \times 10^{-6}$ and $(5.29 \pm 0.75) \times 10^{-6}$, while those for $B \to K^{*}\nu\overline{\nu}$ are predicted between $(6.8^{+1.0}_{-1.1}) \times 10^{-6}$ and $(13^{+4}_{-3}) \times 10^{-6}$ [47, 48, 49, 50, 51]. The branching fractions are assumed to be the same for both charged and neutral channels.[10] Massive New Physics particles could enter into the loops as well, contributing at the same order as the SM particles. Thus even relatively small contributions from New Physics would be noticeable, and various scenarios predict significant enhancements in the observed rates [47, 50]. Therefore, the $B \to K^{(*)}\nu\overline{\nu}$ decays offer an excellent indirect probe for testing the SM and looking for New Physics particles and interactions. In addition, because the final state has missing four-momentum from the two undetectable neutrinos, other exotic sources of undetectable New Physics can also contribute to the missing momentum [47, 52].

The inclusive quark-level process $b \to s\nu\overline{\nu}$ is considered one of the theoretically cleanest FCNC processes due to the lack of non-perturbative contributions from low-energy QCD and from photon exchanges. However, an experimental search for the inclusive modes ($B \to X_s\nu\overline{\nu}$) is difficult due to the two undetectable neutrinos. This analysis instead focuses on the exclusive search in the K and K^* modes. Unlike the inclusive decays, which sum all final s-quark states, exclusive decays require additional

[10] Although most of the literature seems to either imply or outright state their equality, some papers claim small deviations [51].

understanding of the quark-level interactions among and between the initial- and final-state particles. Although this makes the exclusive decays less theoretically clean, the non-perturbative contributions from these QCD interactions can be conveniently encoded into $B \to K^{(*)}$ form-factors.

In terms of $s_B \equiv q^2/(m_B c)^2$, where q^2 is the four-momentum transferred from the B meson to the neutrinos, the $B \to K\nu\overline{\nu}$ differential branching fraction versus s_B can be written as:

$$\frac{d\mathcal{B}(B \to K\nu\overline{\nu})}{ds_B} = \frac{G_F^2 \alpha^2 m_B^5 \tau_B}{256\pi^5} |V_{ts}V_{tb}|^2 \lambda_K^{3/2}(s_B) f_+^2(s_B) |C_L^\nu + C_R^\nu|^2 \tag{2.14}$$

where $\lambda_K(s_B)$ is a function describing the *phase-space* (the allowable kinematics of the decay):

$$\lambda_{K^{(*)}}(s_B) = 1 + \frac{m_{K^{(*)}}^4}{m_B^4} + s_B^2 - 2\left(\frac{m_{K^{(*)}}^2}{m_B^2} - s_B - \frac{m_{K^{(*)}}^2}{m_B^2} s_B\right) \tag{2.15}$$

and V_{ts} and V_{tb} are CKM elements describing the transition of the b-quark to the s-quark via the top-quark. The contributions via the c- or u-quarks ($V_{cs}V_{cb}$ or $V_{us}V_{ub}$, respectively) are much smaller and thus considered negligible. The $B \to K$ transition form-factor $f_+(s_B)$ contains the long-distance dynamics of the matrix elements, and is valid over the full phase-space. The value of $f_+(0)$ is calculated to be 0.304 ± 0.042 [53, 48]. Finally, the factorization coefficient contains the short-distance Wilson coefficients ($C_{L,R}^\nu$), which correspond to the left- and right-handed weak currents, respectively, coupling two quarks to two neutrinos via an EFT four-fermion point interaction. Since only left-handed weak currents exist in the SM, $C_{R,\mathrm{SM}}^\nu = 0$, while [47]:

$$C_{L,\mathrm{SM}}^\nu = -\frac{1}{\sin^2\theta_W} \frac{x_t}{8(x_t-1)^2}\left[x_t^2 + x_t - 2 + 3(x_t - 2)\ln x_t\right] \approx -6.38 \pm 0.06 \tag{2.16}$$

where $x_t = \frac{m_t^2}{M_W^2}$. Except for the form-factor, all of the parameters entering into the SM calculations are known with good accuracy such that the theoretical uncertainty is actually dominated by the mass of the top-quark m_t.

The $B \to K\nu\overline{\nu}$ channels have only one observable: their branching fractions. However, the $B \to K^*\nu\overline{\nu}$ channels have an additional observable relating to the polarization of the K^* meson, which can be extracted from the angular distribution of its daughter particles. The differential branching fraction can be written in terms of three $B \to K^*$ transversity amplitudes $A_{\perp,\parallel,0}$, which in turn depend on three form-factors and on a combination of both $|C_L^\nu + C_R^\nu|$ and $|C_L^\nu - C_R^\nu|$ [47]:

$$\frac{d\mathcal{B}(B \to K^*\nu\overline{\nu})}{ds_B} = 3m_B^2\tau_B(|A_0|^2 + |A_\perp|^2 + |A_\parallel|^2) \tag{2.17}$$

where the factor of 3 corresponds to the sum over the three neutrino flavours. The longitudinal polarization fraction is defined as:

$$F_L = \frac{|A_0|^2}{(|A_0|^2 + |A_\perp|^2 + |A_\parallel|^2)}. \tag{2.18}$$

The main theoretical uncertainty on the $B \to K^*\nu\overline{\nu}$ branching fraction arises from the three $B \to K^*$ form-factors.

The $B \to K^*\nu\overline{\nu}$ modes are sensitive to $|C_L^\nu \pm C_R^\nu|$, which suggests they are excellent probes into the right-handed currents from New Physics couplings. This sensitivity is better seen if the complex Wilson coefficients are rewritten as [47]:

$$\epsilon = \frac{\sqrt{|C_L^\nu|^2 + |C_R^\nu|^2}}{|C_{L,\mathrm{SM}}^\nu|} \tag{2.19}$$

$$\eta = \frac{-\mathrm{Re}(C_L^\nu C_R^{\nu *})}{|C_L^\nu|^2 + |C_R^\nu|^2} \tag{2.20}$$

such that η lies between $-1/2$ and $1/2$. In the SM, this simply reduces to $\epsilon = 1$ and $\eta = 0$, so one can express the relevant branching fractions as:

$$\mathcal{B}(B \to K^*\nu\overline{\nu}) = \mathcal{B}(B \to K^*\nu\overline{\nu})_{\mathrm{SM}}(1 + 1.31\eta)\epsilon^2 \tag{2.21}$$

$$\mathcal{B}(B \to K\nu\overline{\nu}) = \mathcal{B}(B \to K\nu\overline{\nu})_{\mathrm{SM}}(1-2\eta)\epsilon^2 \tag{2.22}$$

$$\mathcal{B}(B \to X_s\nu\overline{\nu}) = \mathcal{B}(B \to X_s\nu\overline{\nu})_{\mathrm{SM}}(1+0.09\eta)\epsilon^2 \tag{2.23}$$

$$\langle F_L \rangle = \langle F_L \rangle_{\mathrm{SM}} \frac{1+2\eta}{1+1.31\eta} \tag{2.24}$$

Measuring these observables can over-constrain the Wilson coefficient values, thus any deviation would be a clear indicator of New Physics. Recent experimental limits of the η and ϵ values are shown in Figure 2–5.

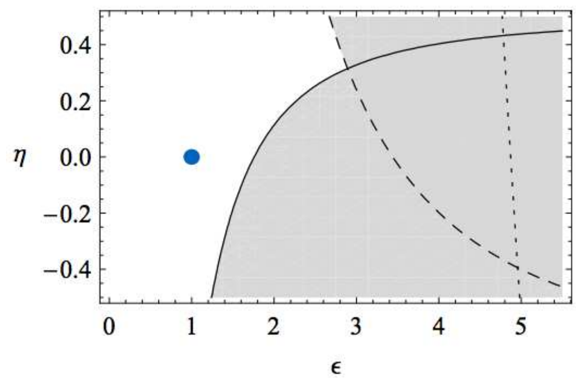

Figure 2–5: Existing constraints at 90% confidence level on ϵ and η from Equations (2.19) and (2.20) [47]. The constraints are taken from experimental upper limits of $\mathcal{B}(B \to K\nu\overline{\nu})$ (solid), $\mathcal{B}(B \to K^*\nu\overline{\nu})$ (dashed), $\mathcal{B}(B \to X_s\nu\overline{\nu})$ (dotted). The dot shows the SM expected values. A limit on $\langle F_L \rangle$ would be represented by a horizontal line, since F_L depends only on η.

Modified $C^{\nu}_{L,R}$ values arise in a variety of New Physics models involving non-SM Z^0 penguin couplings. Such examples include FCNC tqZ couplings within the loop (depicted in Figure 2–6) [51], fourth generation quarks within the loop [50], and FCNC $b \to s$ transitions via a non-SM U(1) gauge boson Z' either at tree level or within the loop [47, 54]. These New Physics scenarios could potentially increase branching fractions by factors of up to ten [50]. In addition, models with a single universal extra dimension, where all the SM particle fields can propagate through a compactified extra dimension, could also change the Wilson coefficients and enhance the observed rate, especially with a large compactification radius [55]. Finally, MSSM particles can also contribute within the penguin diagram in place of the u-type quark-$W^{\pm}$ coupling, including: u-type squark-chargino couplings, top-quark to charged Higgs couplings, d-type squark-gluino couplings, and d-type squark-neutralino couplings, with the first two being the dominant [47]. These are depicted in Figure 2–6. All of these New Physics scenarios can contribute to corrections on the Wilson coefficients and thus be detectable by decay-rate enhancements.

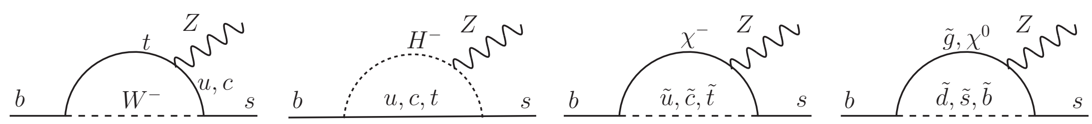

Figure 2–6: Feynman diagrams showing possible New Physics contributions to the b- to s-quark transition involved in $B \to K^{(*)}\nu\overline{\nu}$ decays, including (from left to right): FCNC tqZ, MSSM charged Higgs, u-type squark-chargino, and d-type squark-gluino or squark-neutralino couplings.

The diagrams of the $B \to K^{(*)}\nu\overline{\nu}$ decays are similar to those of $B \to K^{(*)}\ell^+\ell^-$, except that the latter can also have contributions from a radiating photon in place of the Z^0, since the final state contains charged leptons. This electromagnetic coupling can add additional long-distance effects, resulting in the dependence on three Wilson coefficients, whereas $B \to K^{(*)}\nu\overline{\nu}$ only depends on one. Nevertheless, $B \to K^{(*)}\ell^+\ell^-$ decays are predicted to have similar branching fraction enhancements in various New Physics scenarios and, therefore, often appear in the literature together as complementary probes of such models.[11]

There is also a class of New Physics scenarios that predicts significant branching fraction enhancements in the $B \to K^{(*)}\nu\overline{\nu}$ modes, but not in the $B \to K^{(*)}\ell^+\ell^-$ modes, so ratios of the two could provide additional sensitivity to New Physics. These

[11]Even though $\mathcal{B}(B \to K\ell^+\ell^-)$ is predicted to be at the same magnitude as $\mathcal{B}(B \to K\nu\overline{\nu})$, and $\mathcal{B}(B \to K^*\ell^+\ell^-)$ about an order of magnitude less than $\mathcal{B}(B \to K^*\nu\overline{\nu})$, the $B \to K^{(*)}\ell^+\ell^-$ decays have already been observed at the B factories since they are fully reconstructible [56].

scenarios involve replacing the two final-state neutrinos with undetectable non-SM sources of missing energy, such that they would have the same experimental signal as $B \to K^{(*)}\nu\overline{\nu}$ decays. A variety of sources of missing energy in New Physics models have been proposed. For example, recent astronomical observations suggest the presence of low-mass dark matter, which has lead to several proposals of stable scalar particles, with masses of less than a few GeV, originating from SUSY models or from hidden dark sectors [57, 58, 52, 59, 47]. Therefore, a search for a kaon plus missing energy, such as is performed in this $B \to K^{(*)}\nu\overline{\nu}$ analysis, could be sensitive to these (or other similar) low-mass dark matter candidates. In addition, scale-invariant "unparticles" [60], right-handed neutrinos in tree-level decays via a leptophobic Z' [54], or other SUSY particles [57] could contribute as missing energy. Many of these scenarios would not only manifest as branching fraction enhancements that are not reflected in the $B \to K^{(*)}\ell^+\ell^-$ modes, but also in significant modifications to the expected SM distribution of the $B \to K^{(*)}\nu\overline{\nu}$ kinematics, as shown in Figure 2–7. Therefore, measuring $\mathcal{B}(B \to K^{(*)}\nu\overline{\nu})$ over the full kinematic range can help ensure sensitivity to a variety of New Physics models.

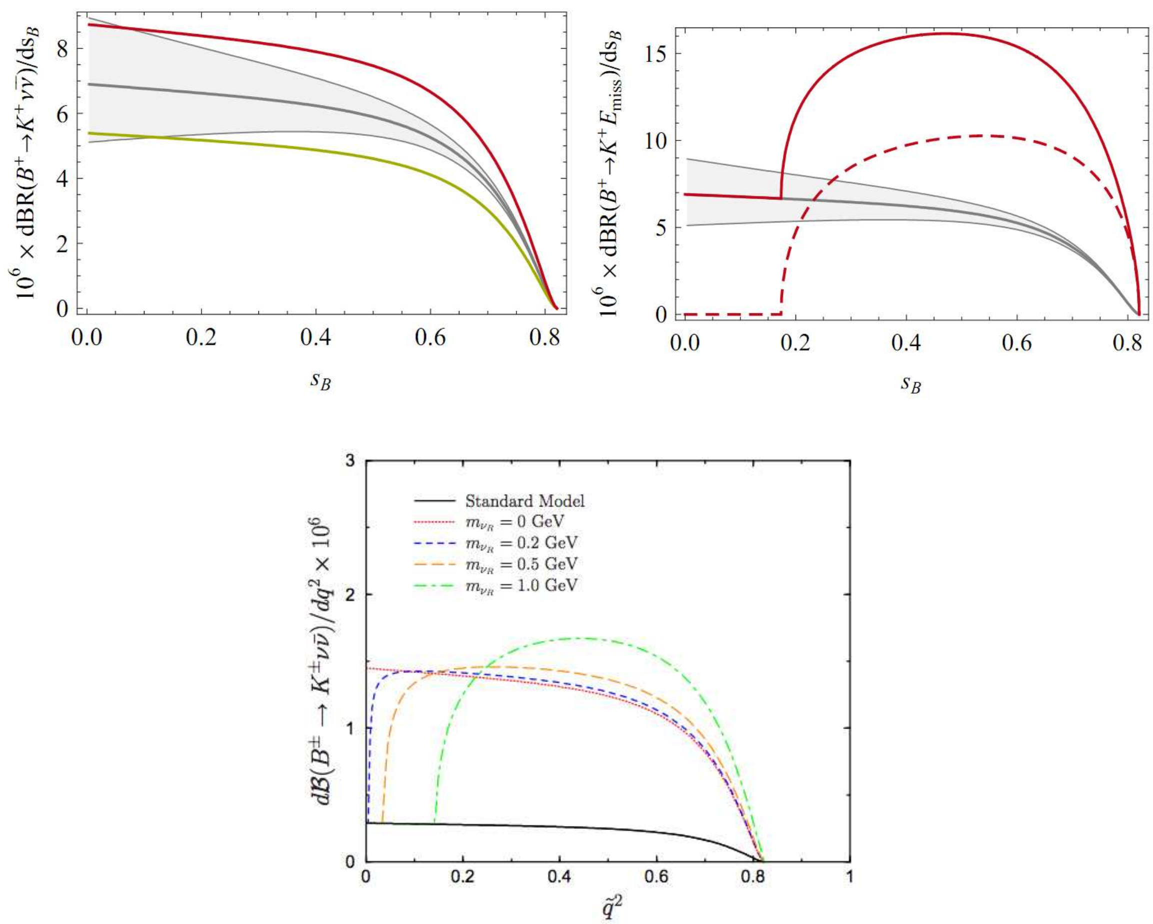

Figure 2–7: Effect on the $s_B \equiv q^2/(m_B c)^2$ distribution of $B^+ \to K^+\nu\overline{\nu}$ from New Physics effects. Other $B \to K^{(*)}\nu\overline{\nu}$ channels show similar effects. (top left) The distribution from two MSSM parameter sets (red and green), with the SM curve and uncertainties (grey) [47]. (top right) The distribution from $B^+ \to K^+ +$ two invisible scalar particles (solid red) compared the SM curve (grey) [47]. (bottom) The effect of a leptophobic Z' contribution (normalized to have decays rates five times larger than in the SM), with various mass hypotheses for a right-handed neutrino [54].

CHAPTER 3
Experimental Environment

3.1 The *BABAR* Experiment

Although the *BABAR* experiment is currently active in a variety of precision measurements of CKM matrix and other Standard Model parameters, as well as New Physics searches, it was originally designed to study CP-violating asymmetries in the decay of neutral B mesons. Achieving this goal required the production of hundreds of millions of $B\overline{B}$ pairs within an environment that is relatively free of background. Thus, the *Positron-Electron Project* (PEP-II) accelerator was built to collide electrons and positrons head-on at a fixed energy. Between 1999 and 2007, PEP-II ran at a *center-of-mass* (CM) energy of 10.58 GeV, which corresponds to the mass of the $\Upsilon(4S)$ resonance particle.[1] Figure 3–1 shows the *cross-section* (production rate probability) of Υ resonances at various CM energies. The $\Upsilon(4S)$, whose mass is only

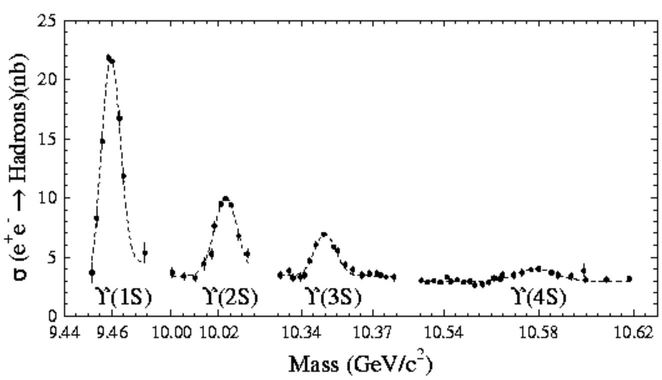

Figure 3–1: The cross-section of Υ resonances as a function of e^+e^- energy, as measured by the CUSB detector [61].

[1] In 2008, *BABAR* also collected data at the $\Upsilon(2S)$ and $\Upsilon(3S)$ resonances, as well as a scan above the $\Upsilon(4S)$ resonance, before shutting down operations.

about 20 MeV/c^2 above the threshold for B-meson pair production, decays into a $B\overline{B}$ pair over 96% of the time [2], about half of which are B^+B^- and half $B^0\overline{B}^0$. Thus, the collision energy of PEP-II was chosen in order to mass-produce B mesons, giving credence to its designation as a *B Factory*.

Hadron colliders, like the LHC and Tevatron, result in collisions of their constituent quarks and gluons, each carrying an unknown fraction of the hadron beam energy, thereby resulting in an unknown initial momentum in the z-direction (which is directed along the beam-axis). Conversely, at a lepton accelerator such as PEP-II, the initial momentum of each collision is well-defined, making it ideal for studying decays involving missing momentum, such as from the neutrinos in $B^+ \to \ell^+\nu_\ell\gamma$ and $B \to K^{(*)}\nu\overline{\nu}$. In addition, the relatively low-energy leptonic collisions at PEP-II provide a clean event reconstruction environment, which makes *BABAR* excellent for precision measurements, such as CP-violation studies. Due to the general purpose nature of the *BABAR* detector design and the high *luminosity* (a measure of the collisions per second per area) from PEP-II, the *BABAR* experiment is also conducive to a variety of other precision measurements of bottom meson, charm meson, and tau lepton decays, as well as searches for rare decays such as $B^+ \to \ell^+\nu_\ell\gamma$ and $B \to K^{(*)}\nu\overline{\nu}$. Such precision measurements can place tight constraints on fundamental parameters of the SM and provide sensitivity to evidence of New Physics.

3.2 The PEP-II Accelerator and Collider

The PEP-II B Factory [62] is an asymmetric e^+e^- collider operating at the SLAC National Accelerator Laboratory in California. It consists of a 3 km-long linear accelerator (Linac) which accelerates the electrons and positrons before injecting them into two counter-rotating storage rings, the High Energy Ring (HER) containing the electron beam at an energy of 9.0 GeV, and the Low Energy Ring (LER) containing the positron beam at 3.1 GeV. A cartoon of the Linac is shown in Figure 3–2.

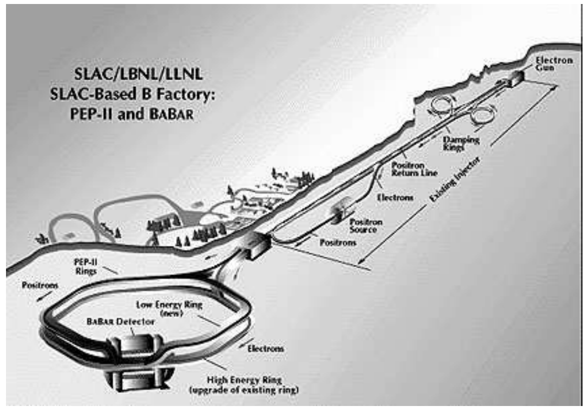

Figure 3–2: Cartoon of the PEP-II Linac, which accelerates electrons and positrons, and the two counter-rotating storage rings. The e^+e^- collisions occur within the *BABAR* detector, which is depicted in the lower left (Courtesy of SLAC National Accelerator Laboratory).

The beams are brought to collision within the *BABAR* detector using a series of large magnets located around the ring and near the interaction region. The asymmetry of the beam energies produces a Lorentz boost of $\beta\gamma = 0.56$ between the lab and $\Upsilon(4S)$ rest frames, resulting in $B\overline{B}$ pairs that are moving forward with respect to the laboratory frame. Since the two $B\overline{B}$ pairs are produced almost at rest in the CM frame (which is also the $\Upsilon(4S)$ rest frame), with momenta of only about $320\,\mathrm{MeV}/c$, this boost is crucial in separating the decay vertices of the two B mesons in order to measure their relative decay times for CP-violation measurements. This results in an average vertex separation of about $250\,\mu\mathrm{m}$ in the z-direction, as opposed to about $30\,\mu\mathrm{m}$ if the beam energies were symmetric.

During the *BABAR* lifetime from 1999-2008, PEP-II reached a peak luminosity of $1.2 \times 10^{34}\,\mathrm{cm}^{-2}\mathrm{s}^{-1}$, which was about four times the design luminosity of $3 \times 10^{33}\,\mathrm{cm}^{-2}\mathrm{s}^{-1}$. A total integrated luminosity of $557\,\mathrm{fb}^{-1}$ of data was delivered by PEP-II, with *BABAR* recording $531.43\,\mathrm{fb}^{-1}$, which includes data taken at energies other than the $\Upsilon(4S)$ resonance. The PEP-II luminosity versus time is provided in Figure 3–3.

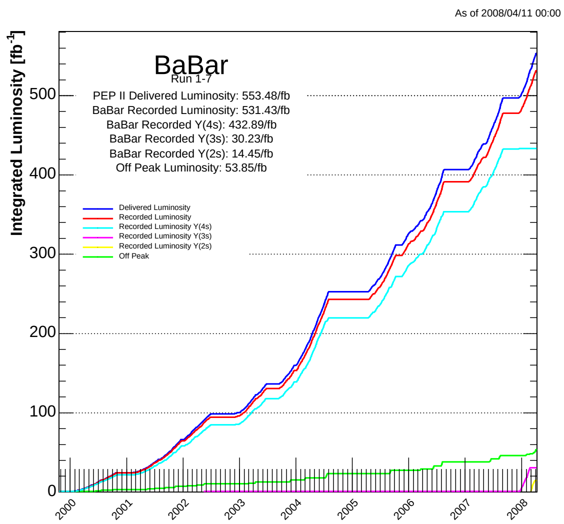

Figure 3–3: The luminosity, as a function of time, that was delivered by PEP-II (blue) and recorded by *BABAR* (red). The other lines represent the amount of data recorded at various energies, including at the $\Upsilon(4S)$ resonance (cyan).

3.3 The *BABAR* detector

The *BABAR* detector was designed to satisfy specific performance criteria to achieve the physics goals of the experiment. It was built to provide a large and uniform acceptance of particles, especially in the forward direction. Because of the beam asymmetry needed for $B\overline{B}$ vertex separation, the detector itself is slightly asymmetric around the interaction region (0.37 m offset) to ensure maximum geometric acceptance.

It was also designed for high performance in particle tracking, calorimetry, particle identification, and vertex resolution in order to fully and accurately reconstruct a B-meson decay back to its decay vertex. Because the average momentum of charged particles decaying from B mesons is less than $1\,\mathrm{GeV}/c$, the detector was designed to minimize the amount of material within its active volume in order to reduce the effects of multiple Coulomb scattering on charged particles and to ensure high detection efficiency and energy resolution. A measure of the amount of material is often given in terms of *radiation lengths* (X_0), which is the average distance over which an electron loses all but $1/e$ of its energy by bremsstrahlung. *Bremsstrahlung* occurs when an electron electromagnetically interacts with a nearby atomic nucleus and subsequently loses energy by radiating a photon.

The *BABAR* detector consists of layers of concentrically-arranged sub-detectors, with an outside radius of about 3.5 meters. Closest to the beam axis is the inner detector, which contains a Silicon Vertex Tracker (SVT) to provide precision position measurements on charged particle trajectories (or *tracks*), a multi-wire Drift Chamber (DCH) to measure the momentum and position of charged particles, a ring-imaging Cherenkov detector (DIRC) for charged hadron *particle identification* (PID), and an Electromagnetic Calorimeter (EMC) to measure particle energy. This is all surrounded by a superconducting solenoid magnet, which has a magnetic field strength of 1.5 T, in order to bend charged particle trajectories for momentum measurements and PID. Outside this is the steel flux return (IFR) for the solenoidal magnetic field, instrumented for muon identification. Diagrams of the *BABAR* detector are provided in Figure 3–4. The accelerator and detector have been documented in detail elsewhere [63].

Long-lived charged particles within the detector (e, μ, π, K, and protons) are reconstructed using the tracking system of the *BABAR* detector, consisting of the SVT and DCH. This system is specifically designed to sense "hits" of deposited energy with minimal alteration to the four-momentum of the particle. When a charged particle traverses these sub-detectors, it excites and displaces atomic orbital electrons which subsequently produce ionization that is measured by the sub-detector. Although such interaction has relatively little effect on the traversing particle, some energy loss over distance is expected, measured as $\mathrm{d}E/\mathrm{d}x$. The energy loss via ionization is characterized by the Bethe-Bloch formula, which is shown in Figure 3–5 at various charged particle masses. Therefore, measurements of $\mathrm{d}E/\mathrm{d}x$ within the tracking system are

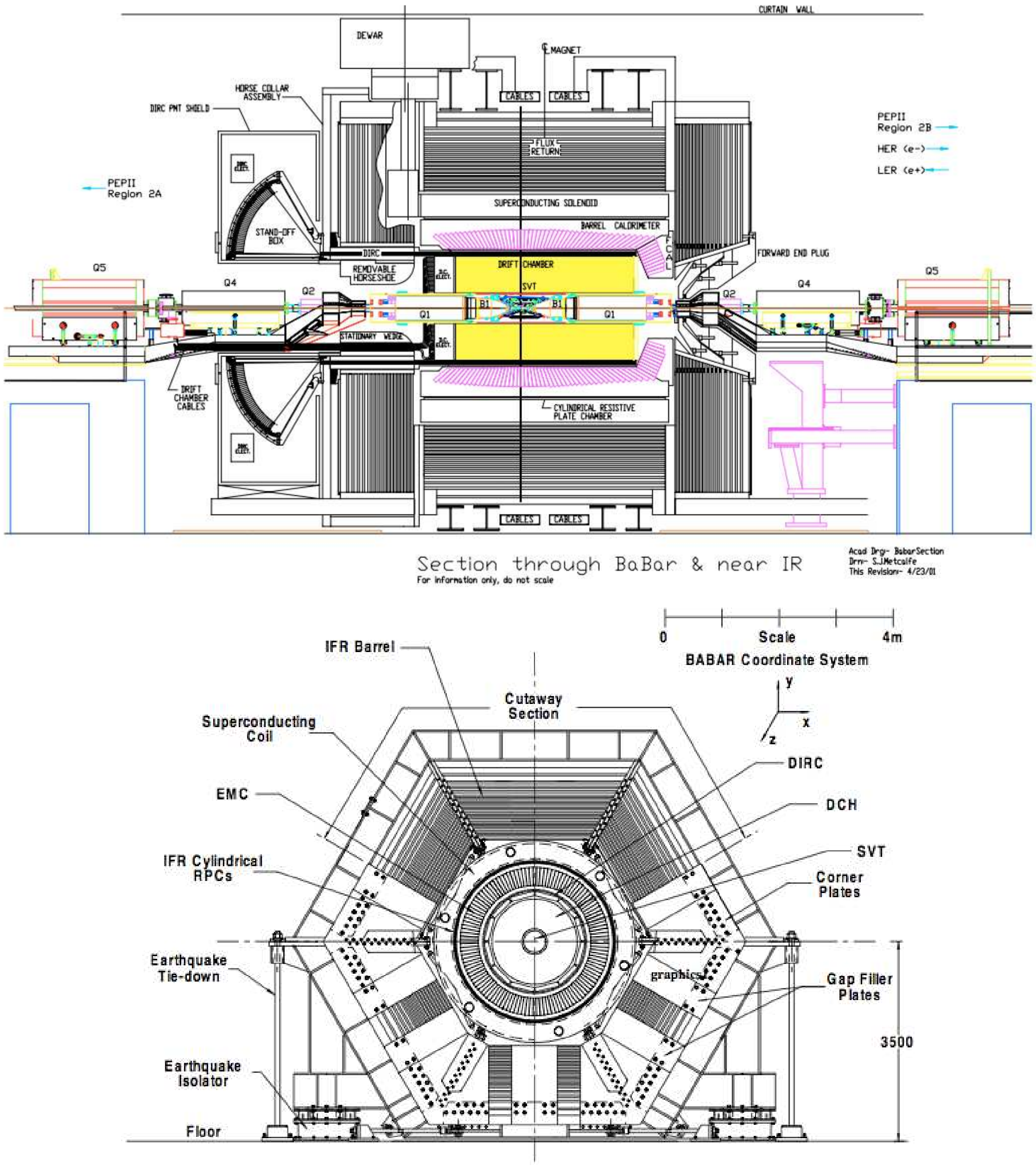

Figure 3–4: A schematic of the *BABAR* detector in the (top) side view parallel to the beam-axis and (bottom) end view [63].

useful to distinguish particle types. Additional event reconstruction and particle identification descriptions are discussed in Section 3.4.

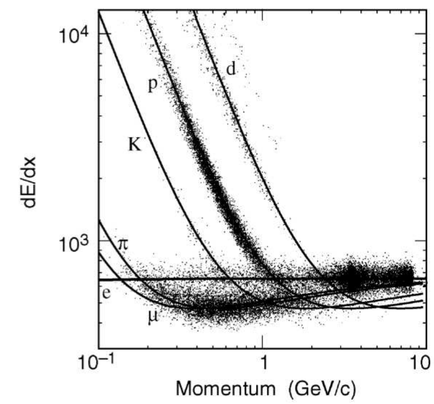

Figure 3–5: Measurements of dE/dx in the drift chamber as a function of momenta, overlaid with the Bethe-Bloch formula predictions for various charged particle types [63].

3.3.1 The Silicon Vertex Tracker (SVT)

The SVT consists of 340 double-sided silicon strip detectors arranged in five concentric layers surrounding the 2.78 cm beryllium beam-pipe, as shown in Figure 3–6. The strips on the inner sides of each layer are positioned perpendicularly to the beam-axis to provide z-coordinate measurements, while the outer sides have longitudinal strips for ϕ-coordinate measurements. The silicon strip detectors are composed of 300 μm thick wafer sensors built on a high-resistivity silicon substrate, with p+ and n+ strips forming a p-n junction with an applied bias voltage. As a charged particle traverses the sensor, it ionizes the medium, producing free electrons and positive "holes" which move in opposite directions in the electric field from the bias voltage, thus producing current. These electric signals are fed to 150,000 channels located on either side of the SVT.

The main purpose of the SVT is to provide high-resolution position measurements for B- and D-meson vertex reconstruction as close to the interaction region as possible. This is achieved using the first three layers, which provide a resolution of 10–15 μm

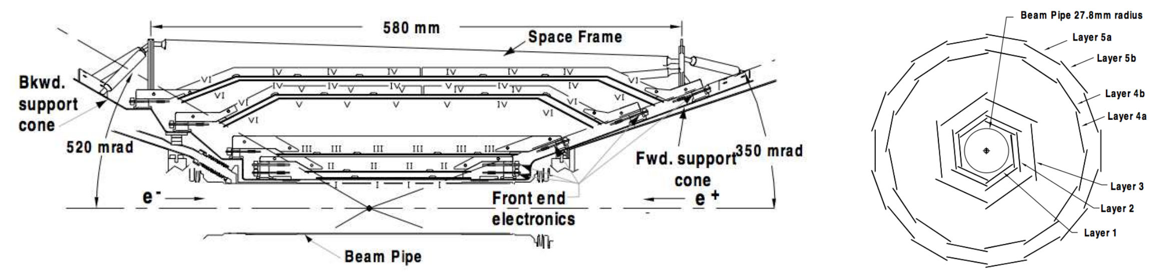

Figure 3–6: A schematic of the Silicon Vertex detector in the (left) longitudinal and (right) transverse views. The Roman numerals label different types of sensors [63].

for tracks at normal incidence. In addition, the SVT works in tandem with the DCH to provide tracking information of charged particles, recording up to ten three-dimensional position hits for a track before it enters the DCH. However, because the inner detector is within a magnetic field, low-momentum particles will form tight spirals without exiting the SVT, making this sub-detector the sole tracking device for charged particles with a transverse momentum less than about 120 MeV/c. The outermost two layers provide alignment with DCH measurements, as well as tracking of low-momentum particles that never reach the DCH. These layers are more limited by multiple Coulomb scattering and thus provide a lower resolution of 40 μm for tracks at normal incidence. Altogether, the SVT provides a B-vertex resolution of 60–100 μm, depending on the decay mode. The SVT covers 90% of the total solid angle in the CM frame, while its constituent material only contributes 4% of a radiation length.

3.3.2 The Drift Chamber (DCH)

Along with the SVT, the drift chamber is responsible for efficient tracking of charged particles within the detector. It provides the main momentum and angular measurement for charged particles with transverse momenta (p_t) greater than about 120 MeV/c, providing up to 40 spatial and dE/dx measurements for tracks with $p_t > 180$ MeV/c. For particles with momenta less than about 700 MeV/c and for particles in the extreme forward and background directions (which are not well measured by the DIRC), it also provides particle identification through ionization energy-loss measurements. Finally, it is the sole sub-detector responsible for vertex reconstruction of longer-lived particles that decay outside the SVT.

Located between the SVT support tube and the DIRC barrel, the DCH consists of 40 layers of wires in a 280 cm-long cylinder filled with a 80:20 helium-isobutane gas mixture. In addition to measuring the transverse momenta and positions using the "axial" wires parallel to the beam-axis, 24 of the 40 wire layers have a small stereo angle with respect to the z-axis to enable the measurement of the longitudinal positions of tracks. The wires form a total of 7104 small hexagonal drift cells of dimensions $\sim$ 19.0 mm $\times$ 11.9 mm, depicted in Figure 3–7. Each cell consists of one

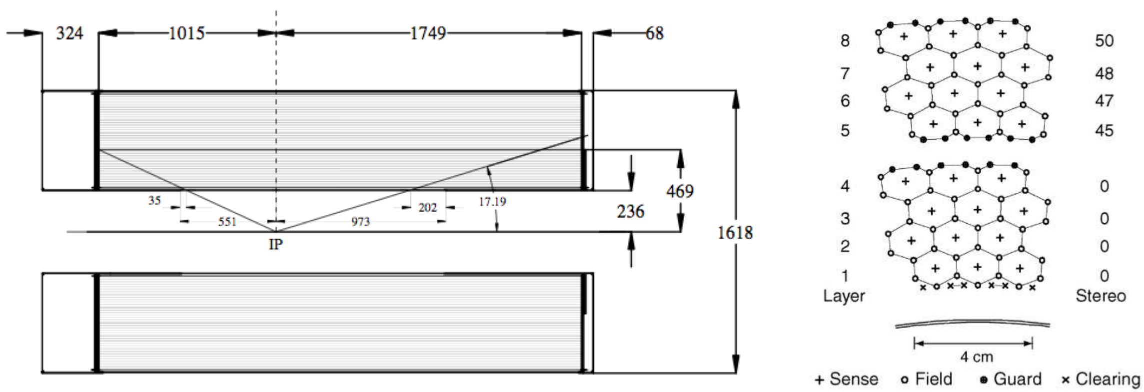

Figure 3–7: (left) Longitudinal schematic of the drift chamber, with dimensions given in mm [63]. (right) Transverse schematic of the layout of drift cells, formed as sense wires surrounded by field wires, for the innermost eight wires. The cell boundary lines are only a visualization aid. The stereo angles are given in mrad [64].

20 μm sense wire made of gold-plated tungsten-rhenium surrounded by six 120 μm field wires of gold-plated aluminum with a high positive voltage (2 kV).[2] As a track passes through the drift chamber, it interacts with atomic electrons in the gas mixture, leaving a trail of freed electrons (ions) which drift toward (away from) the sense wires due to the electric field from the field wires. As the electrons approach the sense

[2]A third type of wire, the guard wire, is used to adjust the electric fields of boundary cells to improve uniformity.

wire, they avalanche to form more ionizations, thus increasing the electric signal that ultimately is collected by the sense wire. The total charge collected in the cell provides $\mathrm{d}E/\mathrm{d}x$ measurements of the traversing charged particle, with an average resolution of about 7%. The drift time of the ionization electrons provides the radial distance from the sense wire to where within the cell the track actually passed, with an average resolution of about 140 μm.

The resolution on the DCH momentum measurements is $\sigma_{p_t}/p_t = (0.13\%)p_t(GeV/\mathrm{c})+0.45\%$. The first resolution term is due to the track curvature measurements and the second is from multiple scattering. Thus, the resolution on low-momentum tracks is limited by multiple scattering. To reduce the multiple scattering and the amount of material a particle traverses before reaching the EMC, the DCH was constructed with aluminum field wires, thin inner and outer cylindrical walls, a thin forward end plate, and the electronics placed outside the geometrical acceptance of the detector. This is also why the helium-isobutane gas mixture was chosen, as well as to quench photons from excited helium atoms that would otherwise be problematic with a high purity of helium. At normal incidence, the DCH thickness corresponds to 1.08% X_0, with 0.2% X_0 of this solely due to the wires and gas.

3.3.3 The Detector of Internally Reflected Cherenkov light (DIRC)

Although the DCH can use $\mathrm{d}E/\mathrm{d}x$ and momentum measurements for particle identification at low momentum, the separation between pions and kaons is inadequate above about 700 MeV/c. For analyses such as the $B \to K^{(*)}\nu\overline{\nu}$ search, for example, positively identifying kaons with high purity is necessary. Therefore, *BABAR* designed a novel detector which uses internally-reflected Cherenkov light for the sole purpose of providing hadron PID for particles with momenta between 500 MeV/c and the kinematic limit of 4.5 GeV/c. *Cherenkov radiation* is produced when a charged particle travels faster than light in a given medium, and is emitted as a cone of light at an angle θ_c relative to the direction of the particle. This angle is directly related to the particle velocity $\beta(= pc/E = v/c)$ by $\cos\theta_c = 1/n\beta$, where n is the index of refraction of the medium. Therefore, using the particle momentum and incident angle as determined from the tracking system, together with a measurement of the Cherenkov angle, one can determine the mass of the particle and thus a PID hypothesis. The distribution of θ_c values for various particle types, as measured in the *BABAR* DIRC, are provided in Figure 3–8.

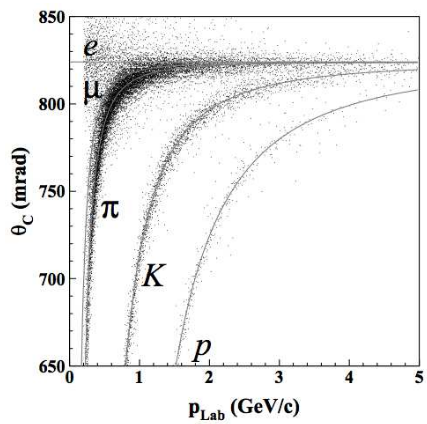

Figure 3–8: Measurements of the Cherenkov angle as a function of momenta, overlaid with the predicted angles for various charged particle types [65].

The DIRC is designed to be as thin as possible, both geometrically and in radiation lengths, in order to reduce the radial size (and thus cost) and the energy resolution degradation, respectively, of the EMC. Therefore, much of the detection mechanism for the Cherenkov photons lies outside the active detector volume. The barrel consists of 144 bars of fused silica, 4.9 m long and only 17.25 mm thick, arranged in a 12-sided polygonal barrel requiring only 8 cm of radial space. These quartz bars not only radiate Cherenkov light, but also have a high index of refraction ($n = 1.473$) which reduces the critical angle for total internal reflection. Thus, about 80% of the Cherenkov light that is produced within the bars will propagate through internal reflection, while preserving θ_c, toward the backward end of the bar (a mirror is located at the forward end of the bar to ensure backward exit). Upon exiting the bars, the light travels about 1.17 m through a conical "standoff box", located outside the solenoidal magnetic field, to an array of 29 mm-diameter photomultiplier tubes (PMTs) which measure the Cherenkov angle and timing of the Cherenkov photons. The stand-off box is filled with about 6000 liters of purified water, which was chosen because it is inexpensive and produces relatively little total internal reflection at the quartz-water interface, since both surfaces have similar indices of refraction. The DIRC provides a total geometrical acceptance of 94% in the azimuthal angle and 83% in the polar angle in the CM frame. The material in the detector volume corresponds to 17% X_0. A schematic of the DIRC is provided in Figure 3–9.

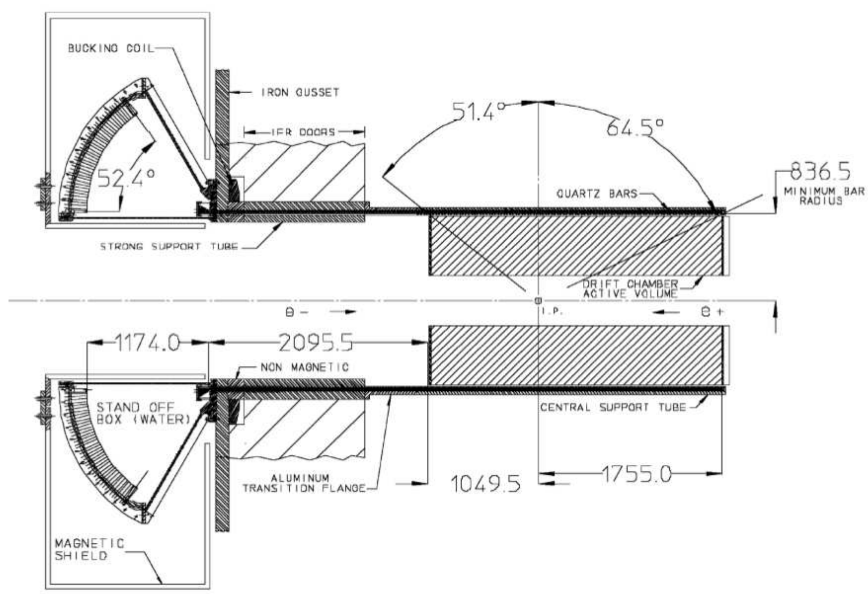

Figure 3–9: Longitudinal schematic of the DIRC, with dimensions given in mm [63].

Using the position and angular information from the tracking system, along with the position and timing signals from the large number of PMTs which detect the Cherenkov light cone, the θ_c measurement is extrapolated and used to determine a likelihood value for e, μ, π, K, and proton particle hypotheses. The resolution for a single photon ($\sigma_{c,\gamma}$) is limited by the PMT resolution. However, the resolution on θ_c scales as $\sigma_{c,\text{track}} = \sigma_{c,\gamma}/\sqrt{N_{pe}}$, where N_{pe} is the number of detected photons, which typically ranges between 20–65 per track. This results in an average θ_c resolution of about 2.5 mrad per track. The DIRC is able to separate pions from kaons between the ranges of about 460 MeV/c to 4 GeV/c, with about a $4\,\sigma$ separation over most of that range. In addition, below about 750 MeV/c, the IFR is insufficient for muon identification, so the DIRC is also used to separate low-energy muons and pions.

3.3.4 The Electromagnetic Calorimeter (EMC)

The EMC is a total absorption calorimeter designed to detect electromagnetic showers with excellent energy and angular resolution from particles within the energy range of 20 MeV to 4 GeV. Located within the solenoidal magnetic field, it is the innermost sub-detector capable of detecting neutral particles, making it vital for photon detection, π^0 and η reconstruction, and improved electron identification. The EMC is the most expensive component of the *BABAR* detector, consisting of 6580 cesium iodide (CsI) salt crystals which are doped with thallium (Tl) at 0.1%. When a photon or electron of at least a few MeV passes through the crystal, it interacts with the electric field produced by the large atoms (*i.e.* with high atomic number Z) within the crystal material. This causes photons to undergo e^+e^- pair production and causes electrons (or positrons) to emit bremsstrahlung photons, which in turn produce a shower of more photons and e^+e^- pairs. This type of cascading particle production is called an *electromagnetic shower*. Meanwhile, the crystals produce scintillation light that is proportional to the amount of energy that they absorb. This light is contained within the crystal by total internal reflection, due to its highly polished surface, and collected by silicon photo-diodes mounted on the back of each crystal.

The EMC consists of 5760 crystals arranged in 48 rings around the cylindrical barrel, and 820 crystals in a conical forward endcap arranged in eight azimuthal rings, as depicted in Figure 3–10. In total, the EMC provides 90% coverage of the solid angle in the CM frame and full azimuthal coverage. CsI(Tl) crystals provide a high light yield, producing 50,000 photons per MeV of particle energy. They also

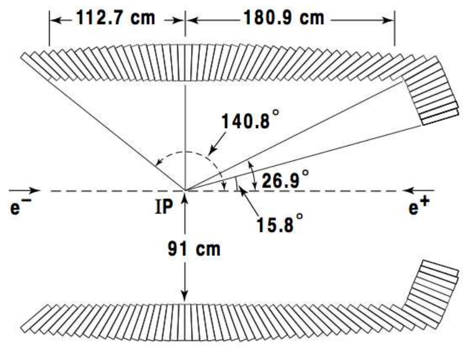

Figure 3–10: Longitudinal schematic of the layout of the crystals within one of the 56 axially symmetric rings of the electromagnetic calorimeter. Both the barrel and endcap are depicts. The dimensions are given in mm [64].

have a short radiation length of 1.8 cm, which allows for shower containment within a compact EMC design, as well as a small *Molière radius* (the average transverse radius that contains 90% of an electromagnetic shower) of 3.8 cm for position resolution. Each crystal is machined into tapered trapezoids, with a front-face area of about $4.7 \times 4.7\,\mathrm{cm}^2$ and a rear-face area of $6.1 \times 6.0\,\mathrm{cm}^2$, making the crystals slightly smaller than one Molière diameter. This fine segmentation of the calorimeter also enables photon separation and angular resolution. The crystals have lengths of about 30 cm, corresponding to 16–17.5 radiation lengths, with the higher X_0 in the forward region to minimize leakage out of the EMC. The EMC crystals are supported from the outside to minimize material in front of the EMC, resulting in a total amount of material from the interaction point to the EMC of only 0.3–0.6 X_0 in the barrel region and the five outer rings of the endcap.[3]

The photo-electric charge yield of the diodes must be translated into a measurement of deposited energy using calibration, which is performed on each crystal

[3]The inner three rings of the forward endcap have 3.0 radiation lengths of material in front of them due to the presence of SVT support structures and electronics, as well as the innermost dipole accelerator magnet.

individually using opposite ends of the relevant energy scale. On the low energy threshold, a radioactive source which emits 6.13 MeV photons is used. For GeV range calibration, the well-defined kinematics of Bhabha scattering events ($e^+e^- \to e^+e^-$), which are collected at a high rate during normal data-taking collisions, are compared with simulations. These calibrations are also used to determine the EMC resolution, given as two terms summed in quadrature: $\sigma_E/E = 2.3\%/\sqrt[4]{E(GeV)} \oplus 1.9\%$, where E is the incident particle energy and σ_E is the corresponding uncertainty on the particle energy. The first term stems from fluctuations in photon statistics but is also affected by noise from electronics and beam-related backgrounds. The second term dominates at energies greater than about 1 GeV and is due to detector imperfections such as non-uniformity in light collection, leakage, and calibration uncertainties. The reconstructed invariant masses of $\pi^0 \to \gamma\gamma$ and $\eta \to \gamma\gamma$ are used to infer the energy dependence of the angular resolution, which is found to be $\sigma_\phi = \sigma_\theta = 3.9mrad/\sqrt{E(GeV)}$. For a typical $B\overline{B}$ event, the π^0 resolution is about 7 MeV.

3.3.5 The Instrumented Flux Return (IFR)

The IFR is designed to identify muons down to about 600 MeV and to detect neutral hadrons, such as K_L^0 and neutrons, which can leak out of the EMC. Located outside of the 1.5 T solenoid magnet, the IFR is a large hexagonal iron structure that is not only capable of absorbing energy, but also responsible for directing the field lines for the return of the magnetic flux from the solenoid. The IFR consists of a barrel and two end-doors, each segmented into layers ranging in thickness from 2 to 10 cm for the outermost layers. Alternating between the 19 layers of steel within the barrel (and 18 layers in the end-doors) are either resistive plate chambers (RPCs) or limited streamer tubes (LSTs) to detect “streamers” from ionizing particles. An additional 2 layers of detectors are located between the EMC and solenoid. The multiple layers provide a radial coordinate for tracking. A schematic of the IFR is shown in Figure 3–11.

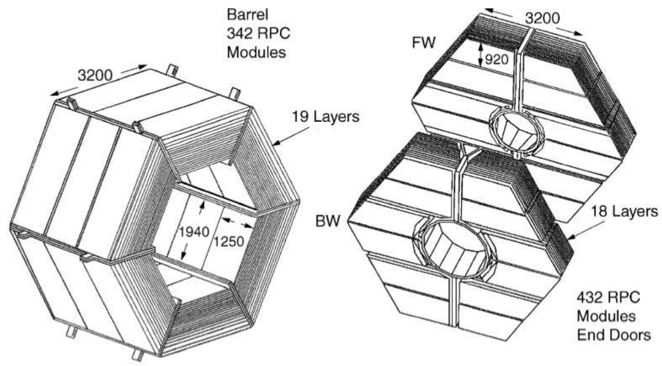

Figure 3–11: A schematic of the Instrumented Flux Return, specifically depicting the shape and instrumented layers of the (left) barrel and (right) two end doors. The dimensions are given in mm [63].

The RPCs consist of two highly resistive plates (10^{11}–$10^{12}\,\Omega\,\mathrm{cm}$) held at a large potential voltage of about 8 kV and separated by a small 2 mm gap filled with an argon-based gas mixture. As in the DCH, when a particle ionizes as it passes through the gas, the electric field accelerates the resulting electrons into an avalanche. However, the stronger electric field in the RPCs results in a controlled gas-discharge avalanche with significantly more gain, called a *streamer*, which produces an electric signal that is less dependent on the size of the initial ionization (unlike in the DCH, which employs the proportional ionization for $\mathrm{d}E/\mathrm{d}x$ measurements). The streamer signal then induces a charge on two sets of aluminum read-out strips, which are positioned outside the plates and perpendicular to each other, to provide ϕ- and z-coordinates. Initially, only RPCs were installed. However, their performance quickly degraded during the first year of detector operation, due to construction flaws and other factors, and were replaced by improved RPCs in the endcaps and by LSTs in the barrel.

The LSTs consist of $15\,\mathrm{mm} \times 17\,\mathrm{mm}$ cells, each 3.75 m long [66]. Seven or eight of these cells are laid flat into a plastic (PVC) tube, and several of these tubes are placed side-by-side within each layer. There are about 1200 tubes in total, located within 12 of the 18 barrel gaps which originally housed the RPCs.[4] Each cell is coated internally with graphite paint for grounding, contains a 100 μm high voltage ($\sim$5500 V) wire in the cell center, and is filled with a non-flammable CO_2-based gas mixture with argon and isobutane. As with the RPCs, the gas operates in the streamer mode when ionized. Charge is collected on the central anode while simultaneous charge is induced on z-coordinate copper strips located outside the tubes and perpendicular to the wire. The muon identification efficiency, using a high-purity PID selector that corresponds to a 1.2% pion mis-identification rate, improved from 63% to 83% after the IFR upgrade.

3.4 Event Reconstruction

3.4.1 Charged Particle Tracking

Within the magnetic field of the solenoid, which is directed along the z-axis, charged particles will travel along a curved trajectory in the transverse plane. The resulting radius of curvature for each charged particle provides the measurement of its transverse momentum (p_t), with the direction of the curvature indicating its charge. Using the position measurements obtained from the tracking system hits, charged particle tracks are reconstructed using pattern recognition software designed to find all of the hits that are likely from a single particle. This is done using the DCH information first, due to both the higher number of hits expected within the DCH and the lower background rates. The hits within the DCH are characterized as circles of radii, corresponding to the drift-time of the ionization electrons, such that tracks are reconstructed as traveling along the tangents of the circles. Afterwards, the SVT hits are combined with the DCH tracks, and the low p_t tracks that do not exit the SVT are identified from the remainder. The helix parameters of the tracks are fitted with a Kalman filter algorithm [67] to determine the momentum from the curvature,

[4] The other six layers are filled with brass to provide additional absorption material.

as well as the position and direction at both the interaction region for vertexing and the DCH exit for PID. The filter accounts for such effects as multiple scattering, measured inhomogeneities in the magnetic field, and energy loss in the detector material. Finally, a second-pass tracking algorithm is employed to improve reconstruction, such as identifying secondary tracks from daughter particles and removing duplicate tracks from low p_t particles that loop within the tracking system. A simulated example of a reconstructed $B^+ \to \ell^+\nu_\ell\gamma$ event is shown in Figure 3–12.

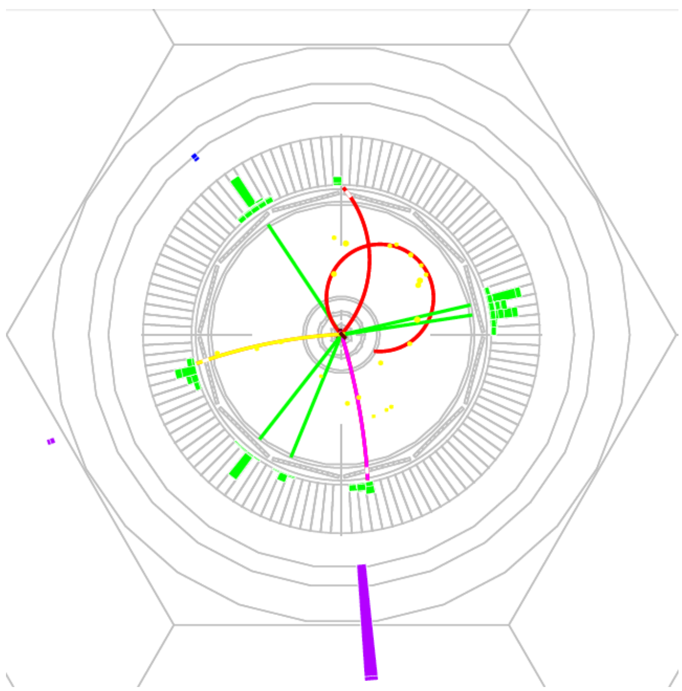

Figure 3–12: A Monte Carlo simulation of a $B^+ \to \mu^+\nu_\mu\gamma$ signal event within the detector, where the second B meson decays to $B^- \to D^0\rho^-$, $D^0 \to K^-\pi^+\pi^0$, $\rho^- \to \pi^-\pi^0$. The red, yellow, and purple lines represent the $\pi^\pm$, K^-, and μ^+ tracks, respectively. The green lines represent the undetected but assumed trajectory of the photons from $B^+ \to \mu^+\nu_\mu\gamma$ and the π^0 decays. The yellow dots depict the DCH tracking hits of various radii, the green bars represent the EMC showers, and the purple bar represents the muon detection in the IFR.

3.4.2 Charged Particle Identification

Since the energy deposits in the tracking system are proportional to the $\mathrm{d}E/\mathrm{d}x$ of the passing particle, low-momentum tracks are mainly differentiated into particle type by the dE/dx measurements. Above 500 MeV/c, the DIRC also provides separation between kaons and pions using Cherenkov angle information. It also provides some separation between low-energy muons and charged pions.

The information provided by the EMC crystals are also employed for PID. The momentum as measured by the DCH, along with the energy as measured in the EMC, are used to find the energy-momentum ratio E/p of a particle shower. For electrons and positrons, this ratio is approximately one, since they generally deposit all of their energy through electromagnetic showers. Conversely, hadrons will produce hadronic showers with E/p ratios of less than one, since a large fraction of hadronic showers contain non-visible energy such as from interactions with atomic nuclei and neutrino production. In addition, the energy deposited by electrons will tend to be concentrated in two or three crystals, while hadronic showers tend to have more spread-out shower shapes.

Finally, since the muons produced at *BABAR* are minimum-ionizing particles, with momenta too low to be likely to produce bremsstrahlung, they retain most of their energy through the tracking system and EMC. Therefore, muons are identifiable by their passage through the IFR. Hadrons can also pass into the IFR, but they tend to be recognizable by the wider transverse size and shallower penetration depth of the IFR hits (as compared with muons), as well as "missing" hits due to neutral particles within the hadronic shower.

All of these above factors are combined into multivariate selectors to identify the type of charged particle associated with a given track. The mass and energy of that track are then recalculated to match the PID hypothesis using the well-measured momentum values.

3.4.3 Neutral Cluster Reconstruction

Neutral particles leave no tracks but can nevertheless be reconstructed. Photons are identifiable by the presence of an electromagnetic shower, like that of an electron, but with no track leading to the energy deposit. Likewise, neutral hadrons, namely neutrons and K_L^0 mesons, can be identified by hadronic showers within the EMC and/or IFR, with no associated tracks. Since K_S^0 and π^0 mesons will usually decay within the detector, they typically can be reconstructed from two charged pions and from two photons, respectively.

Energy deposits in adjacent crystals are combined into “bumps” by looking for local maxima. A bump is required to have at least one crystal with an energy deposit greater than 10 MeV. Adjacent crystals are included if they have an energy above 1 MeV or if a crystal adjacent to them has an energy above 3 MeV. The total energy of a bump is required to be greater than 20 MeV, as electronic noise and beam-related backgrounds tend to dominate below this. All of the reconstructed tracks are extrapolated to the EMC, and if the position of a bump center is not consistent with originating from any tracks, it is assumed to originate from a neutral particle and is termed a *cluster*. Clusters with more than one local maxima can be produced by π^0 daughters that land close to each other in the EMC and, therefore, EMC shower shapes can help distinguish such π^0 clusters from photon clusters. In addition, shower fluctuations from hadrons can also result in multiple maxima or produce additional clusters from shower fragments that were not properly reconstructed into the primary cluster.

3.5 *BABAR* Dataset and Simulation

3.5.1 The *BABAR* Dataset

The $B^+ \to \ell^+ \nu_\ell \gamma$ and $B \to K^{(*)} \nu \overline{\nu}$ analyses use all of the *BABAR* data collected at the $\Upsilon(4S)$ resonance, which corresponds to an integrated luminosity of about $430\,\mathrm{fb}^{-1}$. *BABAR* recorded about 470 million $B\overline{B}$ pairs. The cross-section of $e^+e^- \to \Upsilon(4S)$ is about 1.05 nb, as outlined in Table 3–1. The total cross-section from the other $q\overline{q}$ and $\tau^+\tau^-$ background events (referred to as *continuum events*) is about four times larger than that of $b\overline{b}$ events. These background events can largely be distinguished from $B\overline{B}$ decays by particle multiplicity and event-shape characteristics, resulting in a high signal-to-background ratio for studying $B\overline{B}$ decays.

Table 3–1: Production cross-sections (σ) in e^+e^- annihilation at a CM energy of 10.58 GeV [64].

$e^+e^- \to$	$b\overline{b}$	$c\overline{c}$	$s\overline{s}$	$u\overline{u}$	$d\overline{d}$	$\tau^+\tau^-$	$\mu^+\mu^-$	e^+e^-
σ (nb)	1.05	1.30	0.35	1.39	0.35	0.94	1.16	~ 40

The data samples used in the $B^+ \to \ell^+\nu_\ell\gamma$ ($B \to K^{(*)}\nu\overline{\nu}$) analysis consist of data collected at the $\Upsilon(4S)$ resonance, with a total integrated luminosity of 423.46 (429.059) fb^{-1} which corresponds to approximately 465.04 ± 5.12 (470.97 ± 2.84) million $B\overline{B}$ pairs. The data sample is split into six "runs", or time periods, each accounting for differences in the PEP-II and *BABAR* conditions and performance at the time of data-taking. The luminosities and the estimated number of B mesons produced during each of the six runs are given in Table 3–2.

Table 3–2: The data luminosity and estimated number of $B\overline{B}$ pairs ($N_{B\overline{B}}$) within each run of *BABAR* data-taking. The processed *BABAR* data samples used in the $B^+ \to \ell^+\nu_\ell\gamma$ and $B \to K^{(*)}\nu\overline{\nu}$ analyses are slightly different.

	$B^+ \to \ell^+\nu_\ell\gamma$		$B \to K^{(*)}\nu\overline{\nu}$	
Run	Luminosity (pb^{-1})	$N_{B\overline{B}}$ ($\times 10^6$)	Luminosity (pb^{-1})	$N_{B\overline{B}}$ ($\times 10^6$)
1	20403	22.40±0.14	20597	22.56±0.14
2	61076	67.39±0.41	62076	68.44±0.41
3	32278	35.57±0.22	32669	35.75±0.22
4	100282	110.45±0.67	100809	111.43±0.67
5	133263	147.19±0.89	133887	147.62±0.89
6	76156	82.04±0.51	79022	85.17±0.51

3.5.2 Event Simulation

The $B^+ \to \ell^+\nu_\ell\gamma$ and $B \to K^{(*)}\nu\overline{\nu}$ analyses use *Monte Carlo* simulations (MC) in order to develop the event selection and test the understanding of the selected data. In order to determine the branching fractions, the MC is also used to estimate the amount of remaining background in the selected data sample and to calculate the absolute selection efficiencies. The MC and data distributions are compared to ensure that the data and the MC are in agreement, as discrepancies can lead to systematic uncertainties in the measurement of the branching fraction.

The MC algorithms use a computing method in which random numbers are generated to produce a sampling that simulates the probabilistic nature of particle physics decays and detector responses. The decays of $B\overline{B}$ events are generated using `EvtGen` [68], while continuum events are generated using `JETSET` [69]. QED corrections are also applied in the production of the MC, via the `PHOTOS` generator [70], to incorporate photon radiation into the pre-defined decay chains, such as from bremsstrahlung photons or initial-state radiation. Using the `Geant4` software package [71], the detector response of the generated particles is simulated within a detailed model of the *BABAR* detector geometry and conditions during any given data run. Beam-related background and detector noise are extracted from the data and overlaid on the MC simulations to improve agreement with data. The simulated energies of the EMC clusters are also smeared to improve the agreement with data [72].

MC samples with high statistics are used to simulate the full expected background in order to optimize the signal selection. The generic background MC samples are split into five categories of events: $e^+e^- \to B^+B^-$, $e^+e^- \to B^0\overline{B}^0$, $e^+e^- \to c\overline{c}$, $e^+e^- \to (u\overline{u}, d\overline{d}, s\overline{s})$, and $e^+e^- \to \tau^+\tau^-$. The $B\overline{B}$ events are simulated to decay *generically* (to all allowed SM B-meson modes), with branching fractions defined from a database that combines experimental measurements and theoretical predictions. Events from $c\overline{c}$ decays are considered separately from the other $q\overline{q}$ modes since they tend to produce D mesons, which are used in the hadronic reconstruction algorithm of B mesons (which will be discussed in Section 4.1), and are thus more likely to produce *combinatoric* (incorrectly reconstructed) B-meson candidates. Since the τ lepton can decay hadronically, it can also produce mis-reconstructed B-meson candidates, but the presence of $e^+e^- \to \tau^+\tau^-$ decays is largely suppressed by kinematic and event-shape restrictions placed on these candidates.

Each MC sample is normalized to the data luminosity for the corresponding run by weighting it according to:

$$\frac{\mathcal{L}\sigma}{N_{\text{gen}}} \tag{3.1}$$

where $\mathcal{L}$ is the data luminosity given in Table 3–2, σ is the cross-section of the generated process, and N_{gen} is the number of events generated in that MC sample. The cross-sections and number of generated events within the generic MC samples are given in Table 3–3, with all six runs combined. The $B^+ \to \ell^+\nu_\ell\gamma$ analysis uses a set of generic MC samples that provide about three times the number of generated $B\overline{B}$ events as expected in data, two times the number of $c\overline{c}$ events, and approximately an equal number of $(u\overline{u}, d\overline{d}, s\overline{s})$ and $\tau^+\tau^-$ events as expected in data. Since the $B \to K^{(*)}\nu\overline{\nu}$ analysis was performed a few years after the $B^+ \to \ell^+\nu_\ell\gamma$ analysis, it uses a later version of the simulation and reconstruction software. The MC sample is much larger, with approximately ten times more statistics than in the data for $B\overline{B}$ and $c\overline{c}$ events, and about four times more than in the data for $(u\overline{u}, d\overline{d}, s\overline{s})$ and $\tau^+\tau^-$ events. The statistical uncertainty of a large MC sample scales as $\sqrt{N}$, where N is the number of (pseudo)random numbers used to generate the MC statistics.

Table 3–3: The cross-sections and numbers of generated events in the generic background MC samples that are used in the $B^+ \to \ell^+\nu_\ell\gamma$ and $B \to K^{(*)}\nu\overline{\nu}$ analyses. All six runs are combined here for conciseness.

MC Sample	$B^+ \to \ell^+\nu_\ell\gamma$ Cross Section (nb)	$B^+ \to \ell^+\nu_\ell\gamma$ Generated Events ($\times 10^6$)	$B \to K^{(*)}\nu\overline{\nu}$ Cross Section (nb)	$B \to K^{(*)}\nu\overline{\nu}$ Generated Events ($\times 10^6$)
Generic B^+B^-	0.550	702.9	0.549	2342.7
Generic $B^0\overline{B}^0$	0.550	690.3	0.549	2387.9
Generic $e^+e^- \to c\overline{c}$	1.30	1088.2	1.30	5496.5
Generic $e^+e^- \to (u\overline{u}, d\overline{d}, s\overline{s})$	2.09	902.6	2.09	3401.0
Generic $e^+e^- \to \tau^+\tau^-$	0.94	382.6	0.94	1605.7

Finally, signal $B^+ \to \ell^+\nu_\ell\gamma$ and $B \to K^{(*)}\nu\overline{\nu}$ MC samples, as well as exclusive MC samples of dominant background decays, are also employed to provide very high statistics for the specific processes studied in these analyses, typically simulating one pre-defined B-meson decay while the second B meson decays generically. The numbers of generated events for signal and exclusive background MC samples are given in Table 3–4.

Table 3–4: The number of generated signal MC and exclusive background MC samples for both analyses. The samples used in the $B^+ \to \ell^+\nu_\ell\gamma$ ($B \to K^{(*)}\nu\overline{\nu}$) analysis are listed above (below) the double line. The "$f_A = 0$" $B^+ \to \ell^+\nu_\ell\gamma$ signal MC is discussed in the text.

Description	Generated Events
$B^+ \to e^+\nu_e\gamma$ vs. generic B^-	7859000
$B^+ \to \mu^+\nu_\mu\gamma$ vs. generic B^-	7871000
$B^+ \to e^+\nu_e\gamma$ ($f_A = 0$) vs. generic B^-	7851000
$B^+ \to \mu^+\nu_\mu\gamma$ ($f_A = 0$) vs. generic B^-	7853000
$B^+ \to \pi^0\ell^+\nu_\ell$ vs. generic B^-	1962000
$B^+ \to \eta\ell^+\nu_\ell$ vs. generic B^-	1962000
$B^+ \to \eta'\ell^+\nu_\ell$ vs. generic B^-	1962000
Inclusive $B \to X_u\ell\nu_\ell$ vs. generic B	17132000
$B \to X_u\ell\nu_\ell$ vs. $B \to D^{(*)}X$	4500000
$B^+ \to K^+\nu\overline{\nu}$ vs. generic B^-	8571000
$B^0 \to K^0\nu\overline{\nu}$ vs. generic $\overline{B}^0$	8427000
$B^+ \to K^{*+}\nu\overline{\nu}$ vs. generic B^-	8595000
$B^0 \to K^{*0}\nu\overline{\nu}$ vs. generic $\overline{B}^0$	8532000
$B^+ \to \tau^+\nu_\tau$ vs. generic B^-	6520000

The signal MC samples of $B^+ \to \ell^+\nu_\ell\gamma$ are generated using the tree-level hadronic matrix element for $B^+ \to \ell^+\nu_\ell\gamma$, as described in Equation (2.12). Since the theoretical uncertainty is large in the soft photon region due to integral divergence at low photon energies, the MC is generated with a minimum signal photon energy of 350 MeV. Although the photon energy spectrum for $B^+ \to \ell^+\nu_\ell\gamma$ peaks well above 1 GeV (as will be shown in Figure 5–3), this low energy cut-off is significant since it may be possible for signal events to have photon energies below 350 MeV, contributing to $B^+ \to \ell^+\nu_\ell$ backgrounds [45], even though the MC does not model such events. In addition, two form-factor models are simulated for the $B^+ \to \ell^+\nu_\ell\gamma$ signal MC: one in which the axial-vector form-factor (f_A of Equation (2.10)) is equal to the vector form-factor (f_V) and one in which $f_A = 0$. Although most theoretical models claim $f_A = f_V$, which is used as the default signal model in $B^+ \to \ell^+\nu_\ell\gamma$ analysis, the signal efficiency in the analysis is also compared with the $f_A = 0$ assumption. Since these two models represent the two kinematic extremes of $B^+ \to \ell^+\nu_\ell\gamma$, comparing the two models provides a useful systematic check to ensure that the $B^+ \to \ell^+\nu_\ell\gamma$ analysis is independent of the $B \to \gamma$ theoretical modeling and any kinematic differences between the models. Additional kinematic information on the signal MC and exclusive background MC samples, for the $B^+ \to \ell^+\nu_\ell\gamma$ analysis, is discussed in detail in Section 5.2.

The $B \to K^{(*)}\nu\overline{\nu}$ signal MC samples are generated using a simple "phase-space" model, which is an equal representation of all the possible kinematic distributions that are allowed by mere four-momentum conservation within the decay. In addition, the $B \to K^*\nu\overline{\nu}$ signal MC assumes that the K^* mesons decay with non-preferential helicity. These samples are reweighted in the analysis to more accurately reflect the SM-predicted kinematic distributions, which is discussed in detail in Section 6.2.1.

3.5.3 Optimization and Blinding

Both the $B^+ \to \ell^+\nu_\ell\gamma$ and $B \to K^{(*)}\nu\overline{\nu}$ branching fractions are expected to be on the order of 10^{-6} to 10^{-5}. Therefore, with the current size of the *BABAR* dataset, several hundred events are expected to decay via these signal channels. However, after event reconstruction and background suppression, only a handful of these events, if any, are likely to be observed. Therefore, the primary objectives in these analyses are to set upper limits on the branching fractions of these decays and to maximize sensitivity to a possible observation of the SM-predicted processes. These goals require maximizing the efficiency of reconstructing and selecting a signal decay, while minimizing the background. This is accomplished by carefully choosing signal selection criteria and their values. Although much of the selection is defined by studying the expected distributions of various histograms of observable quantities, the specific values in the final selection are determined objectively by maximizing a quantitative metric. These analyses use the *Punzi figure of merit*, which is specifically proposed for selection optimization in order to both set upper limits and make an observation discovery. The Punzi figure of merit is defined as [73]:

$$P_{\rm fom} = \frac{\epsilon_{\rm sig}}{\frac{n_\sigma}{2} + \sqrt{N^{\rm MC}_{\rm bkg}}} \tag{3.2}$$

where $\epsilon_{\rm sig}$ is the signal efficiency and $N^{\rm MC}_{\rm bkg}$ is the normalized number of surviving MC background events. The number of standard deviations n_σ is assigned as 1.285, which corresponds to a 90% confidence level for branching-fraction upper limits. One of the advantages of using Equation (3.2) is its independence from the branching fractions of the signal decays, which are the very quantities these analyses are trying to measure. Conversely, the figure of merit $N_{\rm sig}/\sqrt{N_{\rm bkg} + N_{\rm sig}}$, where $N_{\rm sig}$ is the expected number of signal events, requires an assumed or measured signal branching fraction to determine the size of $N_{\rm sig}$ relative to $N_{\rm bkg}$. Details regarding the optimization of each analysis are discussed in Sections 5.4 and 6.4.

To avoid experimenter bias when optimizing the selection criteria, MC simulations are relied upon rather than the data. The data that is in or around the signal region is "blinded" until the full analysis process, background estimations, and systematic uncertainties are finalized and reviewed within the *BABAR* Collaboration. *Blinding* is achieved by vetoing out all data events, within well-defined signal regions, when the background yield is larger than the expected signal yield by less than about two orders of magnitude. The unblinded data outside these signal regions, called *sidebands*, are useful to validate agreement between the data and the MC, and to extrapolate data yields and characteristics into the signal region. In the $B^+ \to \ell^+\nu_\ell\gamma$ analysis, the blinded signal region is defined using the reconstructed B-meson mass and the reconstructed neutrino mass-squared. In the $B \to K^{(*)}\nu\overline{\nu}$ analysis, the blinded signal region is also defined using the reconstructed B-meson mass, as well as the amount of extraneous EMC energy within the event. After a full review within the collaboration, the data events are unblinded to obtain the actual data measurements and distributions that were collected by BABAR.

3.5.4 Remarks About Plots

In the following chapters, unless otherwise explicitly stated, all one-dimensional histogram plots are shown using the generic background MC samples, which are stacked and scaled to the dataset luminosity of each run using the weights calculated from Equation (3.1). The data are overlayed as dots with error bars, except in blinded regions. For comparison purposes, the signal decay distributions are overlayed as red-dashed lines. Unless otherwise stated, all of the signal channels of an analysis are summed together within a given plot. The red axis on the right of the plots refers to the expected number of SM signal events, which is determined by normalizing the signal MC to the SM-predicted branching fractions of $\mathcal{B}(B^+ \to \ell^+\nu_\ell\gamma) = 1.0 \times 10^{-6}$, $\mathcal{B}(B \to K\nu\overline{\nu}) = 4.0 \times 10^{-6}$, and $\mathcal{B}(B \to K^*\nu\overline{\nu}) = 13.0 \times 10^{-6}$. The plots within the $B^+ \to \ell^+\nu_\ell\gamma$ analysis use the default $f_A = f_V$ signal MC, unless otherwise stated.

CHAPTER 4
Hadronic-Tag B-Meson Selection

4.1 Hadronic-Tag Reconstruction

Because *BABAR* produces B mesons through an $e^+e^- \to \Upsilon(4S) \to B\overline{B}$ process, a useful technique for rare decay searches, such as for $B^+ \to \ell^+\nu_\ell\gamma$ and $B \to K^{(*)}\nu\overline{\nu}$ decays, is to first fully reconstruct one of the two B mesons before looking for evidence of the signal decay within the decay products of the second B meson. Since B mesons primarily decay hadronically via charmed mesons, first a D or D^* meson "seed" is reconstructed and then a combination of charged and neutral particles is added to it so that it fulfills B-meson kinematic criteria. The D meson is reconstructed from the following decays:

- $D^{*0} \to D^0\pi^0,\ D^0\gamma$
- $D^{*+} \to D^0\pi^+$
- $D^0 \to K^-\pi^+,\ K^-\pi^+\pi^0,\ K^-\pi^+\pi^-\pi^+,\ K^0_S\pi^+\pi^-$
- $D^+ \to K^0_S\pi^+,\ K^0_S\pi^+\pi^0,\ K^0_S\pi^+\pi^+\pi^-,\ K^-\pi^+\pi^+,\ K^-\pi^+\pi^+\pi^0$

with $K^0_S \to \pi^+\pi^-$ and $\pi^0 \to \gamma\gamma$. After reconstructing the $D^{(*)}$ seeds, remaining pions and kaons in the event are then combined with the $D^{(*)}$ seed to form a B meson candidate, referred to as the $B_{\rm tag}$. Specifically, the semi-exclusive reconstructed decays, $B^-_{\rm tag} \to D^{(*)0}X^-_{\rm had}$ and $\overline{B}^0_{\rm tag} \to D^{(*)+}X^-_{\rm had}$, require that $X_{\rm had}$ has a total charge of ±1 and is composed of any combination of kaons and/or pions such that $X_{\rm had} = n_1\pi + n_2K + n_3K^0_S + n_4\pi^0$, with $n_1+n_2 \leq 5$, $n_3 \leq 2$, $n_4 \leq 2$, and $n_1+n_2+n_3+n_4 \leq 5$. These $B_{\rm tag}$ candidates are stored in a *BABAR*-wide skim of the full dataset and MC samples, called the `BSemiExcl` skim, which is used in the $B^+ \to \ell^+\nu_\ell\gamma$ analysis. The $B \to K^{(*)}\nu\overline{\nu}$ analysis uses an updated and improved extension of the `BSemiExcl` skim, called the `BSemiExclAdd` skim. One of the main differences of this latter skim is the inclusion of additional seed decays, including $B \to D_s^{(*)+} X^-_{\rm had}$ and $B \to J/\psi\, X^-_{\rm had}$ modes, where $J/\psi \to \ell^+\ell^-$ ($\ell = e$ or μ), as well as the following:

- $D^0 \to\ K^0_S\pi^+\pi^-\pi^0,\ K^+K^-, \pi^+\pi^-\pi^0,\ \pi^+\pi^-,\ K^0_S\pi^0$
- $D^+ \to\ K^+K^-\pi^+,\ K^+K^-\pi^+\pi^0$
- $D^+_s \to \phi\pi^+,\ K^0_S K^+$
- $D^{*+}_s \to D^+_s\gamma$

with $\phi \to K^+K^-$. In total, the `BSemiExcl` skim reconstructs over 1000 different B-decay modes, and the `BSemiExclAdd` skim reconstructs 2968 modes.

To ensure proper $B_{\rm tag}$ reconstruction and reduce combinatoric background from mis-reconstructed $B_{\rm tag}$ candidates, two powerful kinematic variables are employed. Firstly, the reconstructed $B_{\rm tag}$ should have a CM-frame energy ($E_{B_{\rm tag}}$) equal to half the colliding e^+e^- energy in the CM frame ($E_{\rm CM}$), such that the difference:

$$\Delta E = \frac{E_{\rm CM}}{2} - E_{B_{\rm tag}} \tag{4.1}$$

peaks at zero for correctly reconstructed $B_{\rm tag}$ candidates. Secondly, the invariant mass of the $B_{\rm tag}$ candidate should be consistent with the nominal mass of a B meson. However, because the CM energy is precisely known at PEP-II, a higher resolution can be achieved by using the beam energies in place of the reconstructed event energy. The *energy-substituted mass* ($m_{\rm ES}$) is defined as:

$$m_{\rm ES} = \sqrt{\left(\frac{E_{\rm CM}}{2}\right)^2 - p^2_{B_{\rm tag}}} \tag{4.2}$$

where $p^2_{B_{\rm tag}}$ is the three-momentum of the reconstructed $B_{\rm tag}$ candidate in the CM frame. An event is not added to the skims unless $5.20 < m_{\rm ES} < 5.30\,{\rm GeV}/c^2$ and either $|\Delta E| < 0.12\,{\rm GeV}$ or ΔE is within two standard deviations from zero for a given decay mode (which can be as low as $\pm 0.045\,{\rm GeV}$), whichever of the two is the tighter constraint. The step-like shape shown in the ΔE distributions in Figure 4–1 is due to these mode-specific ΔE requirements.

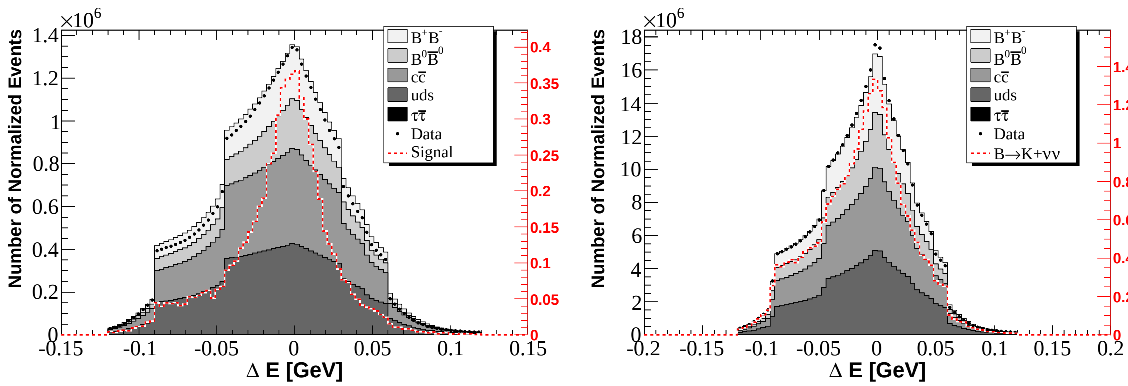

Figure 4–1: The distribution of ΔE of the $B_{\rm tag}$ candidates, as defined in Equation (4.1), in the (left) $B^+ \to \ell^+ \nu_\ell \gamma$ and (right) $B \to K^{(*)} \nu \overline{\nu}$ analyses after the $B_{\rm tag}$ reconstruction skim. The plots compare the data (points) with the generic background MC, and show the signal MC distribution (red dashed). A well-reconstructed $B_{\rm tag}$ should peak at zero.

If several $B_{\rm tag}$ candidates are selected within the accepted modes, the one with the highest "high-multiplicity" purity is chosen. *Purity* is defined as the fraction of correctly reconstructed $B_{\rm tag}$ candidates within the $m_{\rm ES}$ signal region of $\gtrsim 5.27\,{\rm GeV}/c^2$, and is discussed in more detail in Section 4.4. If more than one $B_{\rm tag}$ can be formed with equal purity values, the one with the smallest $|\Delta E|$ value is selected. To save disk space, the `BSemiExcl` skim also requires the high-multiplicity purity to be greater than 12%. The `BSemiExclAdd` skim has no such constraint. Finally, `ROOT` files [74] are produced from the *BABAR* skims which contain relevant variables for each event with an accepted $B_{\rm tag}$ reconstruction.

By fully reconstructing one B meson, the four-momentum of the second B meson, called the $B_{\rm sig}$, can then be determined using the kinematics of the $B_{\rm tag}$ and the known CM energy. The $B_{\rm sig}$ energy is assigned as equal to the $E_{\rm CM}/2$, and its three-momentum as equal and opposite to the three-momentum of the $B_{\rm tag}$ in the CM frame. Any tracks and/or clusters that are not used in reconstructing the $B_{\rm tag}$ are assigned as $B_{\rm sig}$ decay products, as well as all missing energy and momentum within the event.

The missing-energy four-vector is defined as the $B_{\rm sig}$ four-momentum minus the four-momenta of all the remaining "signal-side" tracks and clusters in the event. Evidence of the signal decays $B^+ \to \ell^+\nu_\ell\gamma$ and $B \to K^{(*)}\nu\overline{\nu}$ is then searched for within the signal-side tracks, clusters, and missing four-momentum, as depicted in Figure 4–2.

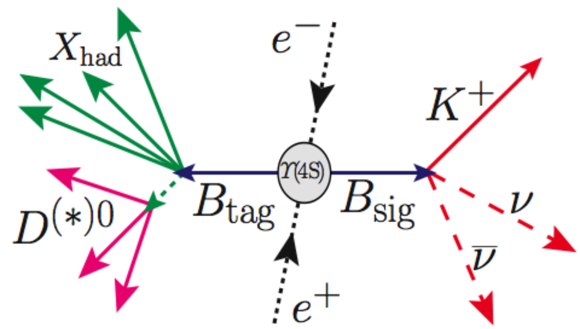

Figure 4–2: Cartoon of a reconstructed $B_{\rm tag}$ candidate and $B^+ \to K^+\nu\overline{\nu}$ signal event.

4.1.1 Comparison with Other Analyses

The upper limits on $\mathcal{B}(B^+ \to \ell^+\nu_\ell\gamma)$ had been reported three times previously, as outlined in Table 2–4, all of which were based on untagged "inclusive" search methods. Unlike exclusive-tag analyses, such as those described in this thesis, inclusive analyses first select evidence of the signal event, such as selecting the highest energy track and cluster within the full event, while the other "recoiling" B meson is formed by simply summing the four-momenta of all the remaining tracks and clusters in the event. In order to reduce the large continuum background, the recoiling B candidate must pass ΔE and $m_{\rm ES}$ requirements. The CM-frame kinematics of the recoiling B candidate are used to obtain the $B_{\rm sig}$ four-momentum which, when combined with the kinematics of the signal track and cluster, determine the neutrino candidate's four-momentum. Although inclusive searches tend to have higher efficiencies than exclusive searches, they are limited by low resolution on the $m_{\rm ES}$, ΔE, and missing energy. In addition, the strong presence of continuum background results in heavy reliance on the modeling of the continuum within the MC. In order to overcome the backgrounds, these searches apply tight kinematic constraints on the signal decay.

However, since there exists some theoretical uncertainty in the expected kinematics of $B^+ \to \ell^+\nu_\ell\gamma$, these analyses tend to be dependent on the assumed theoretical signal model. Conversely, by using the hadronic-tag reconstruction method, which significantly reduces continuum background, the $B^+ \to \ell^+\nu_\ell\gamma$ signal selection can avoid tight kinematic constraints on the signal track and cluster, thus enabling the analysis described in this thesis to be the first model-independent search for $B^+ \to \ell^+\nu_\ell\gamma$.

All of the previous $B \to K^{(*)}\nu\overline{\nu}$ analyses (listed in Table 2–5) have been performed using exclusive-tag analyses, although several used semileptonic-tag reconstruction instead of hadronic-tag reconstruction. Semileptonic-tag analyses also reconstruct the B_{tag} before looking for evidence of the signal decay, but instead reconstruct the B_{tag} candidate via a three-body $B \to D^{(*)}\ell\nu_\ell$ decay. The lepton is required to have a momentum greater than $800\,\mathrm{MeV}/c$. However, because the B_{tag} candidate contains an undetectable neutrino, its momentum cannot be exactly known, and thus the B_{sig} daughter kinematics can only be evaluated in the CM frame. In addition, the m_{ES} and ΔE of the B_{tag} candidate cannot be as tightly constrained, which leads to higher combinatoric backgrounds than in the hadronic-tag reconstruction.

An advantage of the hadronic-tag analyses over the semileptonic-tag and inclusive analyses is the fact that the B_{tag} candidates are reconstructed using fully-detectable decay modes, making them ideal for signal decays containing final-state neutrinos. The full reconstruction of the B_{tag} enables the complete determination of the B_{sig} four-momentum, allowing one to boost the event into the B_{sig} rest frame. The B_{sig} frame provides hadronic-tag analyses with higher resolution on signal kinematic handles, such as the kaon momentum in $B \to K^{(*)}\nu\overline{\nu}$ and the neutrino mass in $B^+ \to \ell^+\nu_\ell\gamma$. A disadvantage of the hadronic-tag reconstruction is that it results in lower signal efficiencies than in the inclusive and semileptonic-tag methods. However, the hadronic-tag reconstruction compensates for the more statistically-limited measurements by providing a higher purity B_{tag} sample, as well as high-resolution knowledge of the signal kinematics for additional background rejection. The low background rates improve the sensitivity for branching-fraction limits. Plus, should signal decay candidates be observed, one would be able to conclude with higher significance that the events are in fact signal decays.

4.2 Energy-Substituted Mass

If a B_{tag} is perfectly reconstructed, its m_{ES} distribution would exactly equal the nominal mass of a B meson, at 5.279 GeV/c^2. As shown in Figure 4–3, the m_{ES} distribution in the signal MC has a narrow peak around the B-meson mass, with the peak's resolution dominated by the spread in E_{beam} of 5–10 MeV [63]. The signal region is defined, using the kinematics of the reconstructed B_{tag}, as $5.270 < m_{\text{ES}} < 5.290\,\text{GeV}/c^2$ in the $B^+ \to \ell^+\nu_\ell\gamma$ analysis and $5.273 < m_{\text{ES}} < 5.290\,\text{GeV}/c^2$ in the $B \to K^{(*)}\nu\overline{\nu}$ analysis. Unlike well-reconstructed B_{tag} candidates, which peak within the signal region, combinatoric background (originating from B_{tag} candidates that are incorrectly reconstructed from either continuum events or both B mesons) produces a distribution that is fairly flat below the signal region and decreases within it. The region below the signal window, the m_{ES} sideband (SB), is valuable for comparing data and MC agreement of combinatoric events and is defined as $5.200 < m_{\text{ES}} < 5.260\,\text{GeV}/c^2$ in the $B^+ \to \ell^+\nu_\ell\gamma$ analysis and $5.200 < m_{\text{ES}} < 5.265\,\text{GeV}/c^2$ in the $B \to K^{(*)}\nu\overline{\nu}$ analysis.

Within both analyses, the dependency on MC modeling is reduced by estimating the expected number of combinatoric background events, within the m_{ES} signal region, directly from the data within the m_{ES} sideband. To do this, the MC is used to extrapolate the shape of the combinatoric distribution into the m_{ES} signal region. Then, data events from the m_{ES} sideband are scaled appropriately in order to model the combinatoric background in the signal region. Furthermore, to improve the MC estimate of the B_{tag} reconstruction efficiency, the generic MC is normalized to the number of data events that peak within the $m_{\rm ES}$ signal region. These procedures are discussed in detail in Sections 5.5 and 6.5.

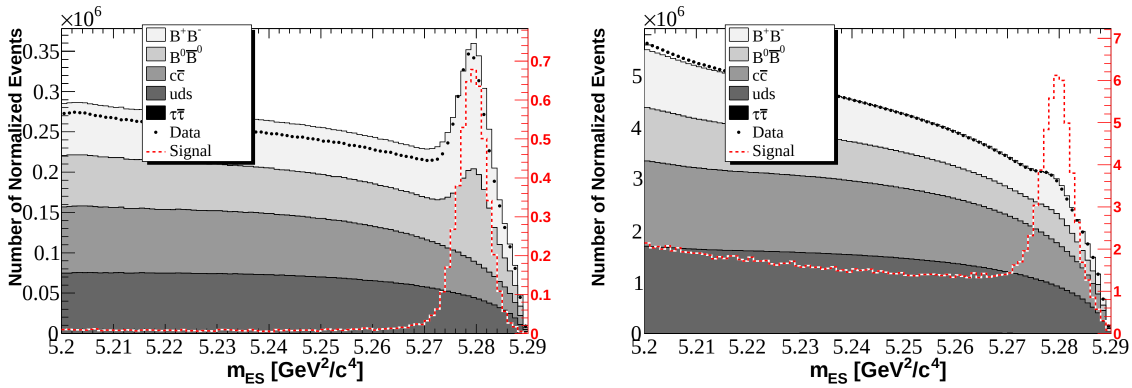

Figure 4–3: The distribution of the $m_{\rm ES}$ of $B_{\rm tag}$ candidates, as defined in Equation (4.2) in the (left) $B^+ \to \ell^+\nu_\ell\gamma$ and (right) $B \to K^{(*)}\nu\overline{\nu}$ analyses after the $B_{\rm tag}$ reconstruction skim. The plots compare the data (points) with the generic background MC, and show the signal MC distribution (red dashed). A well-reconstructed $B_{\rm tag}$ candidate should peak at the B-meson mass of $5.279\,{\rm GeV}/c^2$.

Although the `BSemiExclAdd` skim increases the signal efficiency, the $m_{\rm ES}$ peak in the generic background MC sample shown in Figure 4–3 is much less prominent than in the `BSemiExcl` skim. This is due to the reconstruction of more $B_{\rm tag}$ modes and the removal of the high-multiplicity purity requirement in the skim. Therefore, in the $B \to K^{(*)}\nu\overline{\nu}$ analysis, the higher amount of combinatoric background initially present in the `BSemiExclAdd` skim must be combated with more stringent $B_{\rm tag}$ selection requirements that specifically target continuum and poorly-reconstructed $B\overline{B}$ events.

4.3 Continuum Likelihood and Missing Momentum

When a $B\overline{B}$ pair is produced from the $\Upsilon(4S)$ resonance, the large masses of the two mesons restrict them to low momenta in the CM frame, of about $350\,{\rm MeV}/c$. Therefore, they tend to decay with a spherically-symmetric topology. Conversely, continuum events, due to e^+e^- annihilation into lighter $q\overline{q}$ and $\tau^+\tau^-$ particles, are produced with high momentum and therefore tend to have more jet-like decays with a strongly-preferred direction characterizing the event. Therefore, a multivariate likelihood selector, defined with event-shape variables, is used to further suppress continuum events in order to achieve a higher purity of B mesons. These five variables include: R2All, thrust magnitude, $|\cos\theta_{\text{Thrust}}|$, Thrust$_z$, and $\cos\theta_B$, which are each discussed below. A sixth variable, the direction of the missing momentum (θ_{pmiss}), is employed differently in the $B^+ \to \ell^+\nu_\ell\gamma$ and $B \to K^{(*)}\nu\overline{\nu}$ analyses.

R2All, which is the ratio of the second to zeroth Fox-Wolfram moment [75] using all charged and neutral particles in the event, essentially quantifies the collimation, or "jettiness", of an event topology. Ranging between zero and one, an R2All value closer to zero indicates a more spherically-isotropic event. Therefore, $B\overline{B}$ events tend to have lower values of R2All than continuum events, as shown in Figure 4–4.

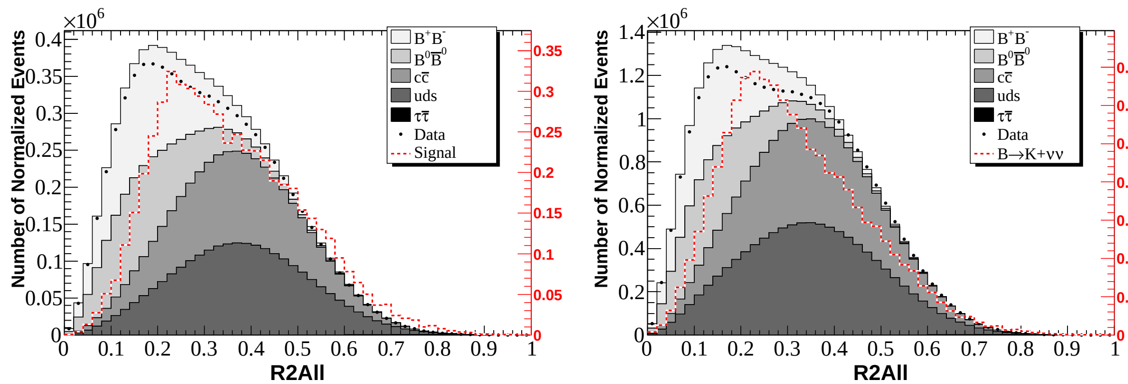

Figure 4–4: The distribution of the R2All variable, which quantifies the "jettiness" of an event, in the (left) $B^+ \to \ell^+\nu_\ell\gamma$ and (right) $B \to K^{(*)}\nu\overline{\nu}$ analyses, after the B_{tag} reconstruction skim and a B_{tag} m_{ES} constraint. This variable is used within the Continuum Likelihood selector. The plots compare the data (points) with the generic background MC, and show the signal MC distribution (red dashed). Higher values indicate more collimated events.

After B_{tag} reconstruction, two thrust axes are determined, one for the B_{tag} and one for all the remaining particles assigned to the B_{sig}. A *thrust axis* is defined as the axis which maximizes the sum of the longitudinal momenta for a set of particles, with the *thrust magnitude* being the total magnitude of their momenta along that axis. Since the two B mesons decay independently of one another, there should be very little correlation between the directions of their decay products. Therefore, the angle between the B_{tag} and B_{sig} thrust axes in the CM frame (θ_{Thrust}) should have a flat distribution for $B\overline{B}$ events. Conversely, when a collimated continuum event is incorrectly reconstructed into a B_{tag}, it is done so using particles from both jets. Thus, continuum events tend to have larger thrust magnitudes, as well as thrust axes that are more parallel to each other such that $|\cos\theta_{\text{Thrust}}|$ peaks at one. The thrust magnitude and $|\cos\theta_{\text{Thrust}}|$ distributions are provided in Figure 4–5.

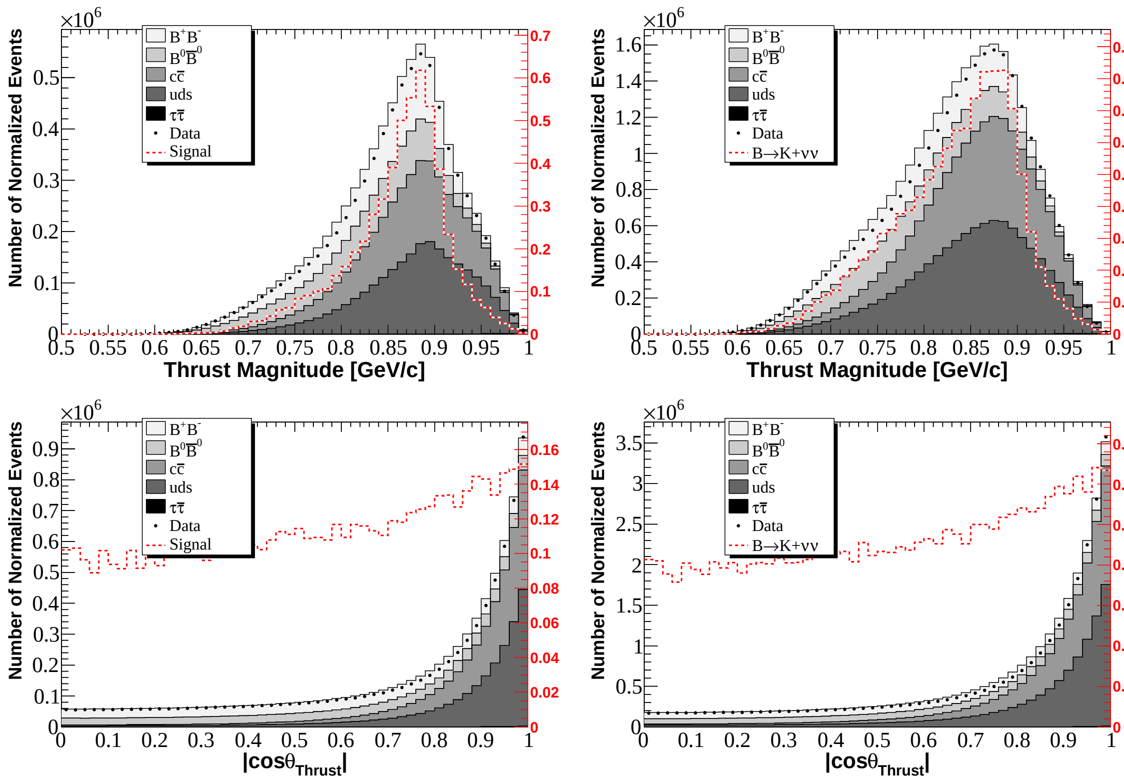

Figure 4–5: The distribution of the (top) thrust magnitude and (bottom) $|\cos\theta_{\text{Thrust}}|$ in the (left) $B^+ \to \ell^+\nu_\ell\gamma$ and (right) $B \to K^{(*)}\nu\overline{\nu}$ analyses, after the B_{tag} reconstruction skim and a B_{tag} m_{ES} constraint. These variables are used within the Continuum Likelihood selector and are described in the text. The plots compare the data (points) with the generic background MC, and show the signal MC distribution (red dashed).

In addition, the high-momentum jets in continuum events tend to be produced at relatively small angles to the beam axis, while $B\overline{B}$ events are more likely to have their momenta directed toward the central region of the detector due to their more isotropic topology. Therefore, continuum events are expected to have larger z-components of the thrust vector magnitude (Thrust_z) than $B\overline{B}$ events. In addition, the distribution of $\cos\theta_B$, where θ_B is the angle between the B_{tag} three-momentum and the z-axis in the CM frame, tends to have a flat distribution for continuum events and to peak at zero for $B\overline{B}$ events due to the larger solid angle at 90° than at 0°. The distributions of Thrust_z and $\cos\theta_B$ are shown in Figure 4–6.

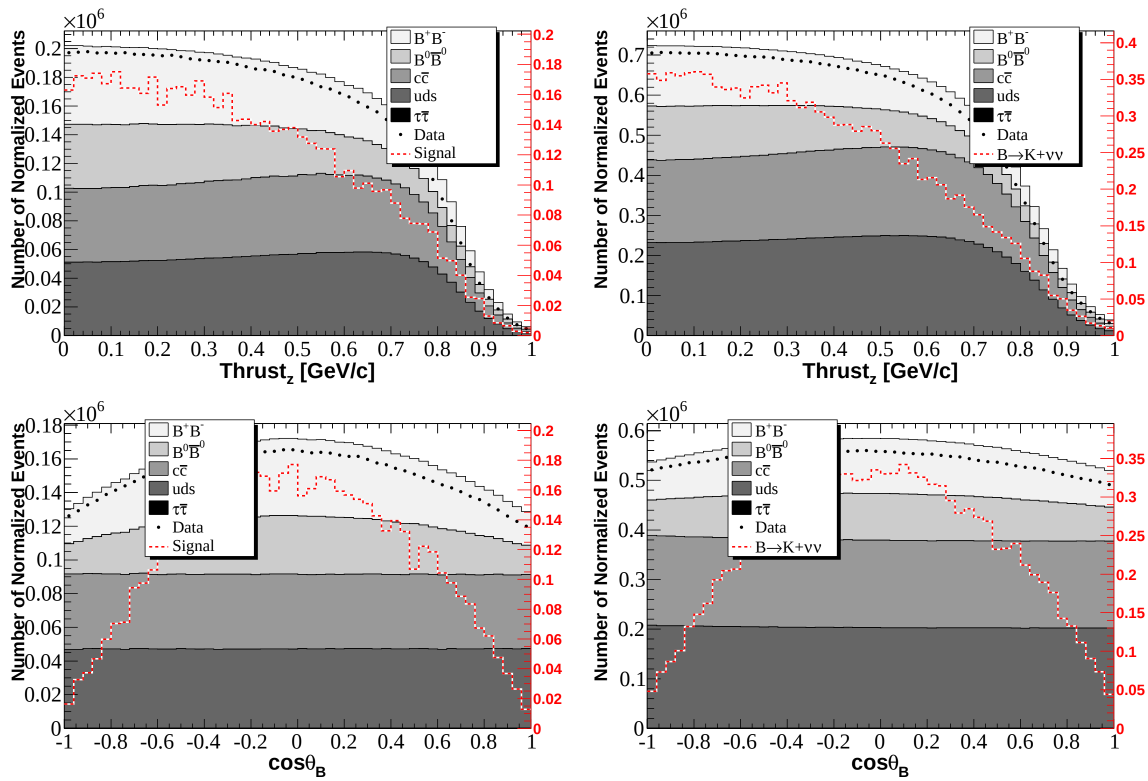

Figure 4–6: The distribution of (top) Thrust_z and (bottom) $\cos\theta_B$ in the (left) $B^+ \to \ell^+\nu_\ell\gamma$ and (right) $B \to K^{(*)}\nu\overline{\nu}$ analyses, after the B_{tag} reconstruction skim and a B_{tag} m_{ES} constraint. These variables are used within the Continuum Likelihood selector and are described in the text. The plots compare the data (points) with the generic background MC, and show the signal MC distribution (red dashed).

Finally, missing momentum within an event can be due to either an undetectable particle like a neutrino, or an otherwise detectable particle that travels outside of the fiducial acceptance of the detector. For continuum events that are produced at small angles to the beam axis, it is common that the source of much of this missing momentum is from particles passing outside the angular acceptance of the detector (*i.e.* "lost down the beam-pipe"). Therefore, $\cos\theta_{\rm pmiss}$ peaks at ± 1, where $\theta_{\rm pmiss}$ is the angle of the missing momentum, with respect to the z-axis, in the CM frame. Background $B\overline{B}$ events may also tend more toward $\cos\theta_{\rm pmiss} = \pm 1$, while the signal MC has a flat distribution due to real particles (neutrinos) that pass within the detector acceptance but which are not detected, as shown in Figure 4–7.

The fiducial acceptance of the EMC is within $-0.916 < \cos\theta < 0.895$ in the CM frame [64], but particles that are incident near the boundary of the calorimeter will often register only part of their total energy, while the rest of their energy contributes to the missing four-momentum within the event. In analyses with one neutrino, such as $B^+ \to \ell^+\nu_\ell\gamma$, it is common to require that the neutrino travels within the acceptance region of the detector. Therefore, a simple requirement is applied in the $B^+ \to \ell^+\nu_\ell\gamma$ analysis that all events must satisfy $-0.912 < \cos\theta_{\rm pmiss} < 0.87$ in the CM frame. Conversely, because the $B \to K^{(*)}\nu\overline{\nu}$ decay contains two final-state neutrinos, it is possible that the vector sum of the momenta of both neutrinos points near the beam axis, even if both neutrinos actually travel through within the detector acceptance. Therefore, in the $B \to K^{(*)}\nu\overline{\nu}$ analysis, $\cos\theta_{\rm pmiss}$ is added into the multivariate likelihood selector as a sixth variable. Ultimately, the effect of the likelihood selector is similar to a direct removal of events with $\cos\theta_{\rm pmiss}$ near ± 1.

Using these five and six event-shape variables for the $B^+ \to \ell^+\nu_\ell\gamma$ and $B \to K^{(*)}\nu\overline{\nu}$ analyses respectively, a multivariate likelihood, referred to as the *Continuum Likelihood*, is calculated using the equation:

$$\mathcal{L}_{\rm CL} \equiv \frac{\prod_i \mathcal{P}_B(x_i)}{\prod_i \mathcal{P}_B(x_i) + \prod_i \mathcal{P}_q(x_i)} \tag{4.3}$$

where $\mathcal{P}_B(x_i)$ and $\mathcal{P}_q(x_i)$ are Probability Density Functions (PDFs) that describe $B\overline{B}$ and continuum events, respectively, for the variables x_i. The generic continuum MC samples are used to determine the continuum PDF and the $B^+ \to K^+\nu\overline{\nu}$ signal MC

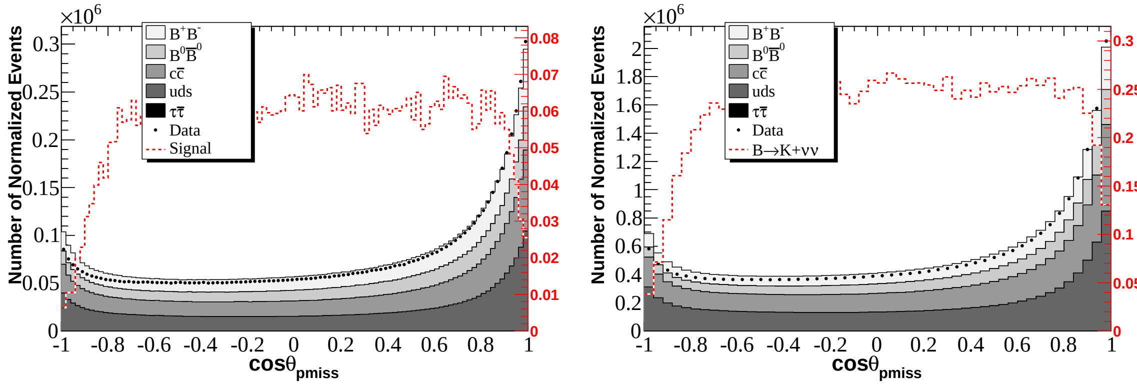

Figure 4–7: The distribution of $\cos\theta_{\mathrm{pmiss}}$, which defines the direction of the missing momentum, in the (left) $B^+ \to \ell^+\nu_\ell\gamma$ and (right) $B \to K^{(*)}\nu\overline{\nu}$ analyses, after the B_{tag} reconstruction skim and a B_{tag} m_{ES} constraint. In the $B^+ \to \ell^+\nu_\ell\gamma$ analysis, this variable is required to be within the fiducial acceptance of the EMC, while in the $B \to K^{(*)}\nu\overline{\nu}$ analysis, it is employed within the Continuum Likelihood selector. The plots compare the data (points) with the generic background MC, and show the signal MC distribution (red dashed).

is used for the $B\overline{B}$ PDF,[1] all with a requirement on the B_{tag} m_{ES} to ensure good $B\overline{B}$ reconstruction. Figure 4–8 illustrates the separation between $B\overline{B}$ and continuum events from this likelihood, such that $B\overline{B}$ events peak at one and continuum events peak near zero. In addition, discrepancies between MC and data are visible around zero, which are likely due to un-modeled continuum-like backgrounds, such as $e^+e^- \to e^+e^-\ell^+\ell^-$ events via two photons. The Continuum Likelihood is required to be greater than 0.3 (0.53) in the $B^+ \to \ell^+\nu_\ell\gamma$ ($B \to K^{(*)}\nu\overline{\nu}$) analysis. This requirement not only suppresses much of the continuum background, but also improves the agreement between data and MC.

4.4 Purity

The B_{tag} mode purity is useful for removing B_{tag} candidates reconstructed in what are considered "dirty" modes with high combinatoric rates. A requirement on

[1]For historical reasons, the $B^+ \to K^+\nu\overline{\nu}$ signal MC with a `BSemiExcl` skim is used to define the $B\overline{B}$ PDF in the $B^+ \to \ell^+\nu_\ell\gamma$ analysis.

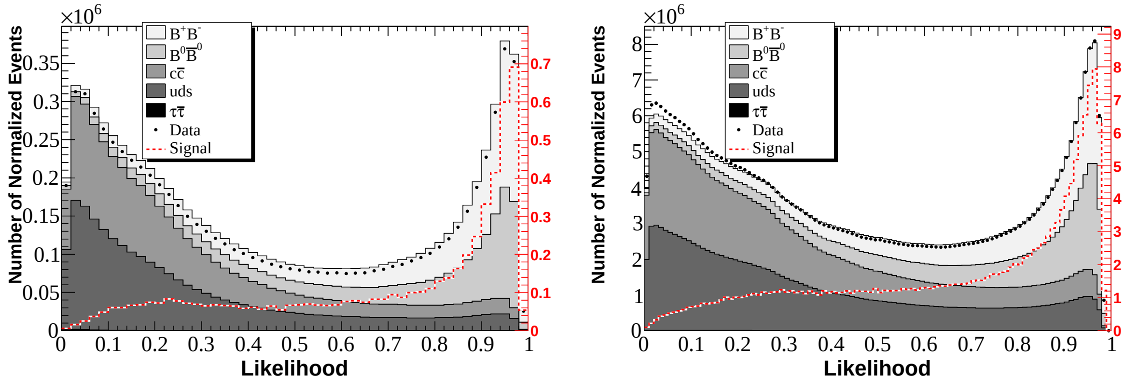

Figure 4–8: The distribution of the Continuum Likelihood selector, used to separate $B\overline{B}$ and continuum events, in the (left) $B^+ \to \ell^+\nu_\ell\gamma$ and (right) $B \to K^{(*)}\nu\overline{\nu}$ analyses after the $B_{\rm tag}$ reconstruction skim. This selector uses five (six) event-shape variables in the $B^+ \to \ell^+\nu_\ell\gamma$ ($B \to K^{(*)}\nu\overline{\nu}$) analyses, respectively. The plots compare the data (points) with the generic background MC, and show the signal MC distribution (red dashed).

the purity level is effectively the same as removing specific $B_{\rm tag}$ decay modes from the hadronic-tag reconstruction process. There are two types of purity values that are referred to in this thesis, described as either high-multiplicity or low-multiplicity. The *high-multiplicity purity* values, set by the designers of the hadronic-tag skims, were determined using all reconstructed events before applying any signal selection. However, the chance of daughter cross-over in the reconstruction of the two B mesons is larger in $B_{\rm sig}$ candidates that decay to a high number of tracks and/or clusters. If one were to only require $B_{\rm sig}$ candidates with low signal-side multiplicity, one would expect that the fraction of well-reconstructed events, for each $B_{\rm tag}$ mode, would mostly be larger. Thus, the $B \to K^{(*)}\nu\overline{\nu}$ analysis defines a *low-multiplicity purity* after requiring that the $B_{\rm sig}$ candidate has one to three signal-side tracks, less than 13 signal-side clusters, greater-than-zero missing energy, and a $B_{\rm tag}$ charge that is opposite the total charge of the $B_{\rm sig}$ tracks. Figure 4–9 shows that both background and signal tend to peak in the low region for high-multiplicity purity, while the low-multiplicity purity is more effective at separating the signal events from the combinatoric backgrounds.

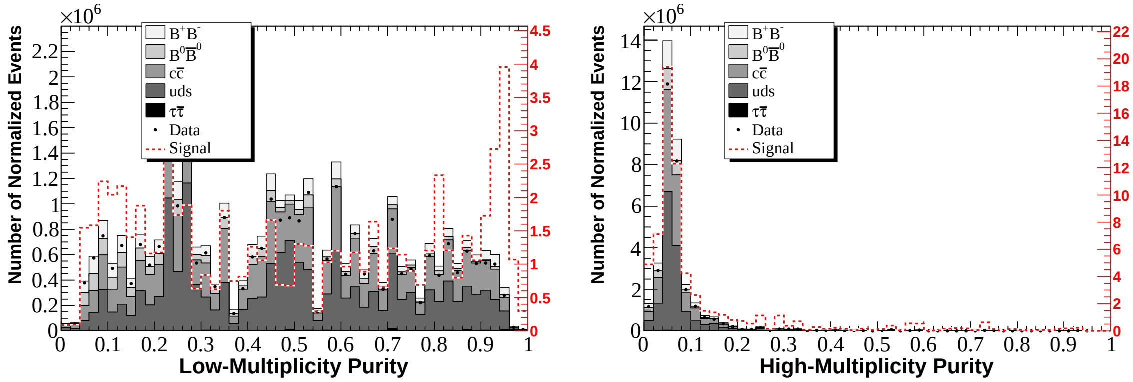

Figure 4–9: The distribution of the (left) low-multiplicity purity values and (right) high-multiplicity purity values. Both plots are produced after the B_{tag} reconstruction skim that is used in the $B \to K^{(*)}\nu\overline{\nu}$ analysis, as well as a requirement of one to three signal-side tracks. The plots compare the data (points) with the generic background MC, and show the signal MC distribution (red dashed).

Both the high- and low-multiplicity purity algorithms use the MC to determine the fraction of correctly-reconstructed B_{tag} candidates within the m_{ES} signal region for a given B_{tag} decay mode. The high-multiplicity purity values were determined by fitting the m_{ES} distribution of each B_{tag} mode, in order to model the peaking (well-reconstructed) and combinatoric components. These fits were performed using the full generic MC sample, including continuum. Conversely, the low-multiplicity purity algorithm uses generator-truth information,[2] within the B^+B^- and $B^0\overline{B}^0$ MC only, to determine the number of $\pi^{\pm}$, $K^{\pm}$, and K^0_S particles that were actually generated by the B_{tag} decay. The low-multiplicity purity thus defines a well-reconstructed B_{tag} as one that is reconstructed with the correct number of $\pi^{\pm}$, $K^{\pm}$, and K^0_S candidates.

The high-multiplicity purity is used in both skims to determine the chosen B_{tag} candidate when an event has more than one, as already discussed in Section 4.1. In

[2] *Generator-truth* information provides the kinematics actually used to generate the MC simulation event, while *particle-truth* information only provides the detected kinematics on the signal-side tracks and clusters as they are reconstructed in `Geant4`. Both also provide reference on the actual particle types and decay chains.

addition, in the $B^+ \to \ell^+\nu_\ell\gamma$ analysis, a high-multiplicity purity requirement is automatically applied at 12% within the `BSemiExcl` skim. In the $B \to K^{(*)}\nu\overline{\nu}$ analysis, no high-multiplicity purity requirement is applied in the `BSemiExclAdd` skim, so the more-appropriate low-multiplicity purity is employed such that all events must have a value greater than 68%. This primarily removes B_{tag} candidates that are reconstructed in X_{had} modes containing either five tracks, or two π^0's and more than one track. Figure 4–10 provides a comparison of the high- and low-multiplicity purity values and illustrates that there are numerous B_{tag} modes with high-multiplicity purity values less than 12%, which have low-multiplicity purity values greater than the 68% threshold.

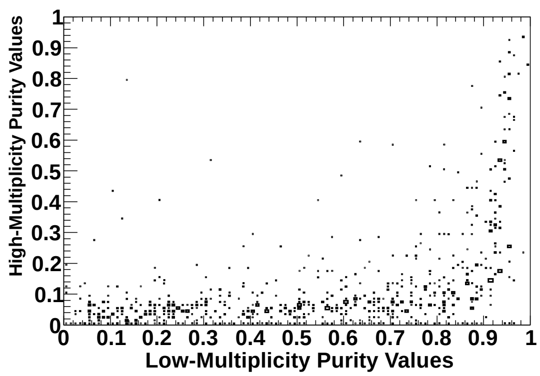

Figure 4–10: The two-dimensional distribution of the low-multiplicity purity versus high-multiplicity purity values for each B_{tag} reconstruction mode, in the $B \to K^{(*)}\nu\overline{\nu}$ analysis. The low-multiplicity purity is used within the $B \to K^{(*)}\nu\overline{\nu}$ analysis, and the high-multiplicity purity is used within the $B^+ \to \ell^+\nu_\ell\gamma$ analysis. The size of the boxes are scaled to the number of reconstructed B_{tag} candidates, after various signal selection requirements.

The remaining signal selection for the two analyses, $B^+ \to \ell^+\nu_\ell\gamma$ and $B \to K^{(*)}\nu\overline{\nu}$, diverges from here and will be discussed separately in the following chapters.

CHAPTER 5
$B^+ \to \ell^+\nu_\ell\gamma$ Analysis Procedure

5.1 Signal Selection

5.1.1 Signal Lepton and Photon Selection

The $B^+ \to \ell^+\nu_\ell\gamma$ analysis requires that there is exactly one signal-side track in the event, with a charge opposite that of the B_{tag}. This track must also satisfy the PID criteria of either an electron or muon, and fail the PID criteria of a kaon hypothesis. No kinematic requirements are applied to the lepton momentum other than those deriving from PID thresholds of about 400 (800) MeV/c for electrons (muons). Requiring exactly one track reduces the signal efficiency by 25%, but removes over 99% of background events, as evident from Figure 5–1.

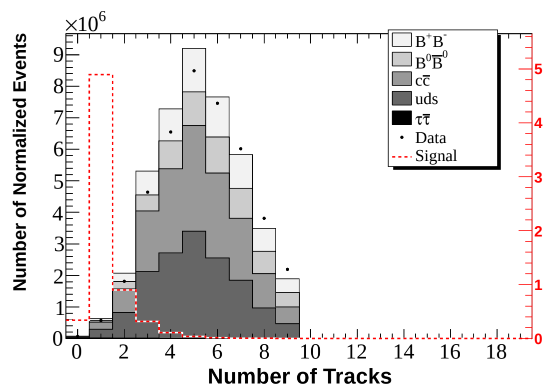

Figure 5–1: The signal-side track multiplicity, in the $B^+ \to \ell^+\nu_\ell\gamma$ analysis, after the B_{tag} reconstruction skim. The plot compares the data (points) with the generic background MC, and shows the signal MC distribution (red dashed).

High energy electrons, such as those typically produced in $B^+ \to e^+\nu_e\gamma$ decays, will often radiate bremsstrahlung photons. Therefore, the four-momentum of an electron-identified signal track is redefined to include any clusters that are identified as bremsstrahlung photon candidates. These candidates are selected by finding signal-side clusters whose lab-frame momentum vectors are almost parallel, in both θ and ϕ, to that of the signal electron, where θ is the polar angle with respect to the z-axis and ϕ is the azimuthal angle around the z-axis. Because of the solenoidal magnetic field in the detector, charged particles are bent in the ϕ direction. Therefore, the electron and its bremsstrahlung photon should have a small difference in ϕ, but remain unchanged in θ. Since a positron will bend in the direction opposite of an electron, $\Delta\phi$ is multiplied by the track charge.

Figure 5–2 shows the angular difference between electrons and true bremsstrahlung photons, where true candidates are determined using the particle-truth information in the MC. Clusters with an angular separation from the electron momentum direction of $-3^\circ < \Delta\theta < 3^\circ$ and $-3^\circ < \Delta\phi \times Q_e < 13^\circ$, where $Q_e = \pm 1$ is the charge of the lepton, are assigned as bremsstrahlung photon candidates. In addition to bremsstrahlung photons, this acceptance region also recovers neutral EMC clusters that are fragments from the electron shower. The angular acceptance region is optimized by maximizing the number of bremsstrahlung candidates and electron-shower fragments, using particle-truth information within the signal MC, while minimizing the number of mis-identified clusters originating from the B_{tag} decay. About 58% of the chosen candidates in the signal MC are true bremsstrahlung photons, 20% are from signal-electron fragments, 19% are from initial-state radiation from the B_{sig}, and only 2.5% are from the true $B^+ \to \ell^+\nu_\ell\gamma$ signal photon.

As shown in Figure 5–3, the energy spectrum of the signal photon peaks around 1.5 GeV and drops off at the low photon energy around 350 MeV.[1] Because these photons are expected to have relatively high energy, the signal-side cluster with the highest CM energy, excepting bremsstrahlung photon candidates, is assigned as the

[1]This is due to the theoretically-driven 350 MeV threshold that is used in generating the signal MC.

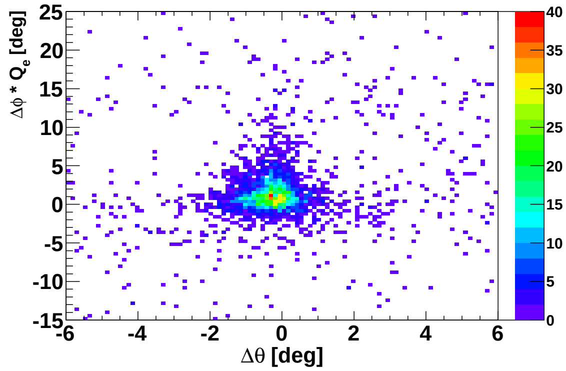

Figure 5–2: The two-dimensional distribution of $\Delta\phi$ versus $\Delta\theta$, the angles between the electron and bremsstrahlung photon three-momenta, after applying all B_{tag} and track criteria. Only true bremsstrahlung photons within the $B^+ \to \ell^+\nu_\ell\gamma$ signal MC are plotted. The value of $\Delta\phi$ is multiplied by the lepton charge (Q_e).

signal-photon candidate. Due to the poor theoretical understanding of the photon energy below Λ_{QCD} and the possibility of soft-photon background contributions to $B^+ \to \ell^+\nu_\ell$, no lower threshold is applied to the signal-photon energy. Therefore, this analysis is sensitive to low-energy photons, limited only by the calorimeter threshold of about 20 MeV. Although the selection of the photon candidate is biased toward higher energy photons, the signal MC indicates that the signal-photon candidate is correctly assigned in about 88% of events, and only 2.5% of the candidates are B_{tag} clusters that are higher in energy than the true signal photon. In less than 10% of events, the true signal photon is not present in the signal-side clusters.

5.1.2 Event Topological Selection

The background can be significantly reduced by requiring that the kinematics of the signal track and the signal-photon candidate are consistent with the presence of a third massless particle originating from the B_{sig}. The neutrino-mass-squared is defined as:

$$m_\nu^2 \equiv (p_{B_{\mathrm{sig}}} - p_\gamma - p_\ell)^2 \tag{5.1}$$

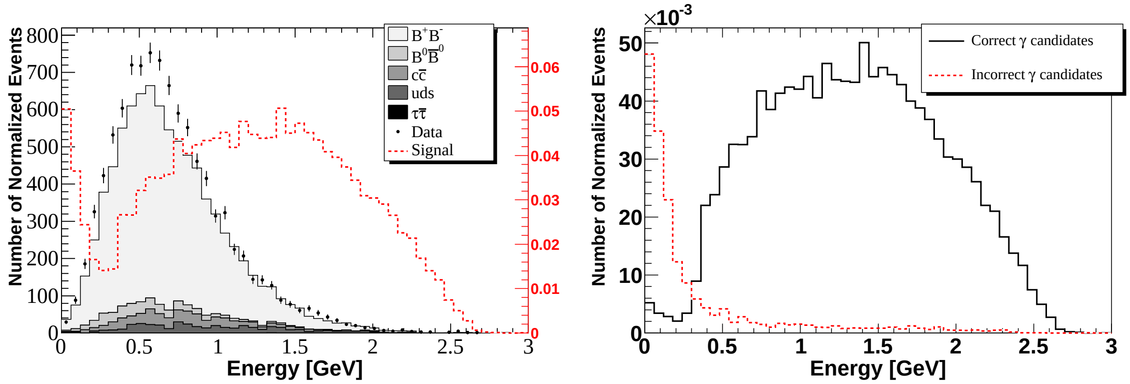

Figure 5–3: The energy distribution of the $B^+ \to \ell^+\nu_\ell\gamma$ signal-photon candidate in the B_{sig} rest frame, after applying all B_{tag} and track criteria. (left) This plot compares the data (points) with the generic background MC, and shows the signal MC distribution (red dashed). (right) This plot shows the signal MC only, separating correctly-identified (black solid) and incorrectly-identified (red dashed) signal-photon candidates, according to particle-truth information within the MC.

where $p_{B_{\text{sig}},\gamma,\ell}$ are the four-momenta of the B_{sig}, signal-photon candidate, and signal track, respectively. This is the most discriminating variable in the $B^+ \to \ell^+\nu_\ell\gamma$ analysis. As shown in Figure 5–4, the background increases with m_ν^2, while $B^+ \to \ell^+\nu_\ell\gamma$ events peak at zero, corresponding to the expected mass of the neutrino. The unphysical negative values and the positive tail in the signal distribution are mainly due to detector resolution, with a tail enhancement in the electron mode due to unrecovered bremsstrahlung photons. The bremsstrahlung recovery algorithm improves the signal efficiency in the electron channel by 12%. The m_ν^2 values are required to be within the signal window of -1 to 0.46 $(0.41)\,\text{GeV}^2/c^4$ for the electron (muon) channels. The data events with values less than $1\,\text{GeV}^2/c^4$ were kept blinded until the end of the analysis.

Since the lepton and neutrino are emitted back-to-back by the virtual $W^\pm$ boson, the lepton and neutrino momenta should reflect this, assuming the missing momentum in the event accurately represents that of the neutrino. To quantify this, the $\cos\theta_{\ell\nu}$ variable is used, which is the cosine of the angle between the lepton and the missing momenta in the rest frame that recoils from the photon emission. This rest frame

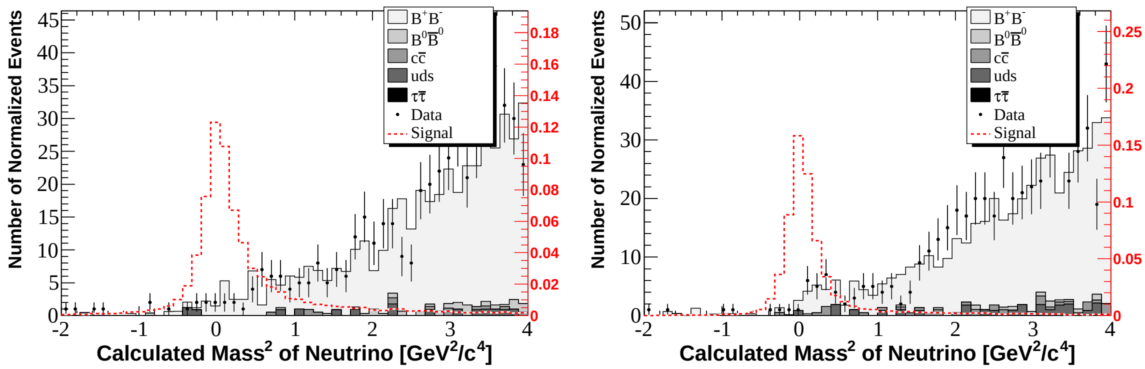

Figure 5–4: The distribution of the m_ν^2 variable for the (left) $B^+ \to e^+\nu_e\gamma$ and (right) $B^+ \to \mu^+\nu_\mu\gamma$ channels. These plots compare the data (points) with the generic background MC, and show the signal MC distribution (red dashed), after applying all B_{tag} and track criteria.

is defined as the B_{sig} four-momentum minus the photon four-momentum. Since the missing energy is assumed to come from a massless particle, the magnitude of the missing three-momentum is used in place of the missing energy, as the latter tends to have lower resolution. As shown in Figure 5–5, if the B_{sig} undergoes a three-body decay, $\cos\theta_{\ell\nu}$ peaks at -1. Therefore, the signal selection requires that $\cos\theta_{\ell\nu} < -0.93$. After all other selection criteria are applied, the MC indicates that the m_ν^2 and $\cos\theta_{\ell\nu}$ criteria together remove 99% of background events with only a 30 (20)% reduction in the signal efficiency for the electron (muon) channel.

5.1.3 Peaking $B^+ \to X_u^0\ell^+\nu_\ell$ Background Suppression

The dominant background for $B^+ \to \ell^+\nu_\ell\gamma$ is from $B^+ \to \pi^0\ell^+\nu_\ell$ events in which one (or both) of the photons in a $\pi^0 \to \gamma\gamma$ decay fakes the $B^+ \to \ell^+\nu_\ell\gamma$ signal photon. Other $B^+ \to X_u^0\ell^+\nu_\ell$ decays, where X_u^0 are neutral mesons containing a u-quark, are also problematic, particularly $B^+ \to \eta\ell^+\nu_\ell$ with $\eta \to \gamma\gamma$. A π^0 (η) decays to two photons 98.8% (39.4%) of the time [2]. Such decays can be suppressed by vetoing events which contain a π^0 or η candidate, reconstructed using the signal-photon candidate and a second cluster of CM energy $E_{\gamma 2}$. An event is rejected if a π^0 candidate can be formed with an invariant mass between 120 and 145 MeV/c^2, and

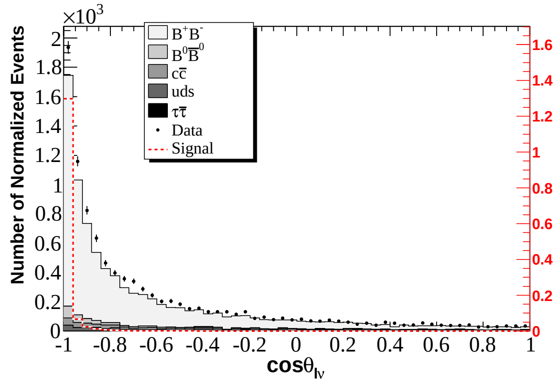

Figure 5–5: The distribution of the $\cos\theta_{\ell\nu}$ variable, where $\theta_{\ell\nu}$ is the angle between the track and the missing momentum in a boosted frame. This plot compares the data (points) with the generic background MC, and shows the signal MC distribution (red dashed), after applying all B_{tag} and track criteria.

with $E_{\gamma 2} > 30\,\text{MeV}$. As shown in Figure 5–6, the combinatoric effects in signal MC are strongest at low $E_{\gamma 2}$, so a second veto is also used, which rejects any event with a π^0 candidate that has an invariant mass between 100 and 160 MeV, and $E_{\gamma 2} > 80\,\text{MeV}$. Since η particles are much more massive, and thus tend to decay into high energy photons even when boosted into the CM frame, $B^+ \to \eta\ell^+\nu_\ell$ events are vetoed if the second photon has an energy of $E_{\gamma 2} > 100$ MeV and an invariant mass between 515 and 570 MeV/c^2 when combined with the signal-photon candidate. These veto values are optimized by maximizing both the signal efficiency and the removal of background MC events in which the π^0 and η are correctly reconstructed.

In addition, the exclusive $B^+ \to X_u^0\ell^+\nu_\ell$ MC samples indicate a non-negligible contribution from $B^+ \to \omega(782)\ell^+\nu_\ell \to [\pi^0\gamma]\ell^+\nu_\ell$ events. The ω decays via $\pi^0\gamma$ 8.92% of the time [2] and, according to the MC, the single γ is usually the highest energy cluster in the decay. Therefore, this background is suppressed by rejecting any event in which the signal-photon candidate and a π^0 candidate produce an invariant mass between 730 and 830 MeV/c^2. This π^0 candidate is reconstructed using any two (non-signal-photon candidate) clusters with a CM energy greater than 70 MeV and which

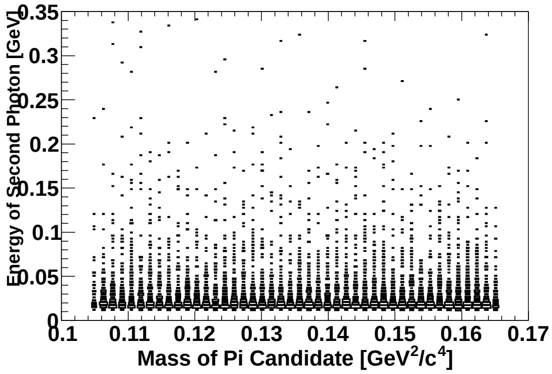

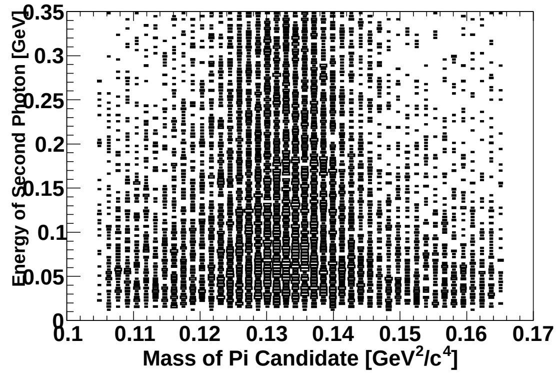

Figure 5–6: The two-dimensional distributions of the invariant mass of each π^0 candidate versus the energy of the second photon, within (left) the signal MC and (right) the generic B^+B^- background MC. The background MC only plots events in which the candidate is a true π^0 meson, according to particle-truth information within the MC. The size of the boxes corresponds to the number of events within a given bin.

produce a $\gamma\gamma$ invariant mass between 115 and 145 MeV/c^2. Because this veto has two kinematic handles, it has minimal effect on the signal efficiency.

After applying all other selection criteria, these vetoes reduce the $B^+ \to \pi^0\ell^+\nu_\ell$ background by 65% and the remaining (non-π^0) $B^+ \to X_u^0\ell^+\nu_\ell$ background by 50%. The surviving events are mainly those in which the π^0 or η is not reconstructible, such as because the energy of the second photon is incorrectly measured ($\sim$ 15% of $B^+ \to \pi^0\ell^+\nu_\ell$ events), the second photon is "lost down the beam-pipe" by traveling outside the fiducial acceptance region of the detector ($\sim$ 35% of $B^+ \to \pi^0\ell^+\nu_\ell$ events), or the second photon is mis-reconstructed into the B_{tag} ($\sim$ 40% of $B^+ \to \pi^0\ell^+\nu_\ell$ events). However, such events tend to have kinematic distributions that are distinguishable from the signal, so their contribution within the signal region can be studied and validated using the E_{extra} and/or m_{ES} sidebands.

One problematic category of $B^+ \to \pi^0\ell^+\nu_\ell$ events ($\sim$ 5% of $B^+ \to \pi^0\ell^+\nu_\ell$ events) occurs when both photon daughters land so close to one another in the EMC that they are reconstructed as a single merged cluster. Since the merged clusters have the full four-momentum of the π^0, the detected final state particles form a three-body decay with a massless neutrino, and therefore mimic the signal kinematics exactly. However, they are suppressible using a cluster-shape variable. The *lateral moment* [64] of a photon EMC energy deposit, which essentially quantifies the cluster width and ranges between zero and one, peaks around 0.25 for signal events, as shown in Figure 5–7. Clusters of two merged π^0 photons tend to be wider than single photon clusters, resulting in larger lateral moment values. Therefore, a lateral moment requirement of < 0.55 is applied to the signal photon candidate to suppress $B^+ \to \pi^0 \ell^+ \nu_\ell$ candidates with merged photons. A lower bound of > 0 is also imposed in order to reduce discrepancies between the data and the MC. About 90% of the signal MC events in which the signal-photon candidate has a lateral moment of zero, signifying a one- or two-crystal cluster, are from "junk" clusters such as detector noise, hadronic fragments, and various non-B physics backgrounds, all of which are difficult to correctly model in the MC. The other $B^+ \to X_u^0 \ell^+ \nu_\ell$ decay modes are not expected to contribute merged cluster backgrounds, due to their higher X_u masses, and the MC particle-truth information confirms this expectation.

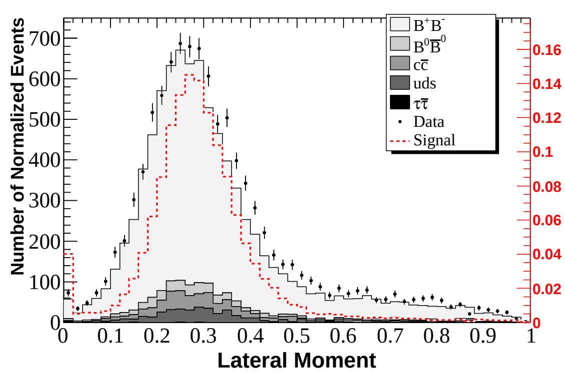

Figure 5–7: The distribution of the lateral moment for $B^+ \to \ell^+ \nu_\ell \gamma$ signal-photon candidates, which quantifies the EMC cluster width and ranges between 0 and 1. The plot compares the data (points) with the generic background MC, and shows the signal MC distribution (red dashed), after applying all $B_{\rm tag}$ and track criteria.

Unfortunately, there is an irreducible category of $B^+ \to \pi^0 \ell^+ \nu_\ell$ events in which the energy of the second photon is $\lesssim 20\,\mathrm{MeV}$ in the lab frame, making its energy too low to be detectable in the EMC.[2] Such low energy clusters are produced when one photon tends to retain most of the π^0 momentum in the lab frame, such that the event kinematics also mimic that of a three-body decay. Although the two π^0 photon daughters are produced back-to-back with equal energies in the π^0 rest frame, these values are boosted when viewed in the lab frame. The decay axis of the two π^0 daughters should be isotropic in the detector, as shown by the flat distribution in Figure 5–8, which plots the cosine of the angle between the flight directions of the higher-energy photon in the π^0 rest frame and of the π^0 in the lab frame. However, in rare situations, the π^0 decay axis happens to lie along the flight direction of the π^0 in the lab frame, or in other words, along the boost axis between the lab and π^0 frames. Thus, one photon will have a four-momentum close to that of the mother π^0 in the lab frame, while the lab-frame energy of the recoiling photon may be so low that it is below the EMC cluster-reconstruction threshold. Such events are irreducible and their distributions completely indistinguishable from signal. Fortunately, however, they are rare, making up only about 2% of the $B^+ \to \pi^0\ell^+\nu_\ell$ background, after the full signal selection criteria is applied.

5.1.4 Additional Cluster Energy

After identifying the B_{tag}, signal-photon, signal-lepton, and bremsstrahlung candidates, $B^+ \to \ell^+\nu_\ell\gamma$ events are expected to contain little or no additional energy within the calorimeter. However, additional energy deposits can result from:

- Hadrons, from the B_{tag} decay, producing showers in the calorimeter that are assigned as independent clusters due to poor cluster or track reconstruction.

[2] This category also contains events in which the second photon energy is detected to be $\lesssim 30\,\text{MeV}$, and thus is not reconstructed in the π^0 veto due to the high combinatorics with clusters at such low energies.

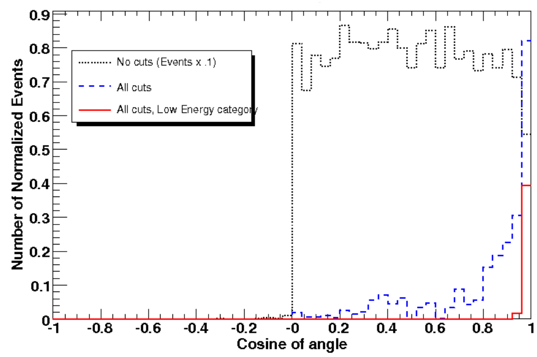

Figure 5–8: The distribution of the cosine of the angle between the flight directions of the higher-energy photon in the π^0 rest frame and of the π^0 in the lab frame. Because only the higher-energy photon of the two daughters is plotted, the cosine is greater than zero by definition. These distributions use the true π^0 mesons within the $B^+ \to \pi^0 \ell^+ \nu_\ell$ exclusive MC, either after applying the $B_{\rm tag}$ and track criteria (black dotted), or after applying the full signal selection (blue dashed). Events in which one photon has an energy $< 20\,\mathrm{MeV}$ (red solid) (after applying the full signal selection) fall almost exclusively into the last bin. For comparison purposes, the black-dotted histogram is scaled by 1/10.

- Beam-related photons, detector noise, or other non-B physics, which typically produce low energy ($\lesssim 30\,\mathrm{MeV}$) clusters, but can be as high as about 100 MeV.
- Photons originating from the $B_{\rm tag}$, such as from unreconstructed $D^* \to D\gamma, D\pi$ transitions. These mis-assigned clusters tend to be low in energy such that the reconstructed $B_{\rm tag}$ can pass the skim selection and $m_{\rm ES}$ requirements.

Conversely, most background events tend to have one or more additional high-energy clusters due to the extra particles in their $B_{\rm sig}$ decays. The total energy of additional clusters, or $E_{\rm extra}$, is calculated by summing the CM energies of all unassigned signal-side clusters with lab-frame energy greater than 50 MeV. As shown in the left plot of Figure 5–9, the signal peaks at zero for $E_{\rm extra}$, while the background is at a minimum around zero and peaks significantly higher in energy. The discrepancy between the data and the MC is reduced after the "$m_{\rm ES}$ sideband-data substitution" procedure, which will be discussed in Section 5.5. Although the $E_{\rm extra}$ variable is uncorrelated with the signal kinematics, the kinematic restrictions from m_ν^2 and $\cos\theta_{\ell\nu}$ remove most background processes, leaving only the irreducible $B^+ \to X_u^0 \ell^+ \nu_\ell$ events which mimic the $B^+ \to \ell^+ \nu_\ell \gamma$ decays in the E_{extra} distribution as well. Therefore, a loose requirement of $E_{\text{extra}} < 0.8\,\text{GeV}$ is applied. In addition, events are required to have less than 13 signal-side clusters. The signal-side cluster multiplicity is shown in the right plot of Figure 5–9.

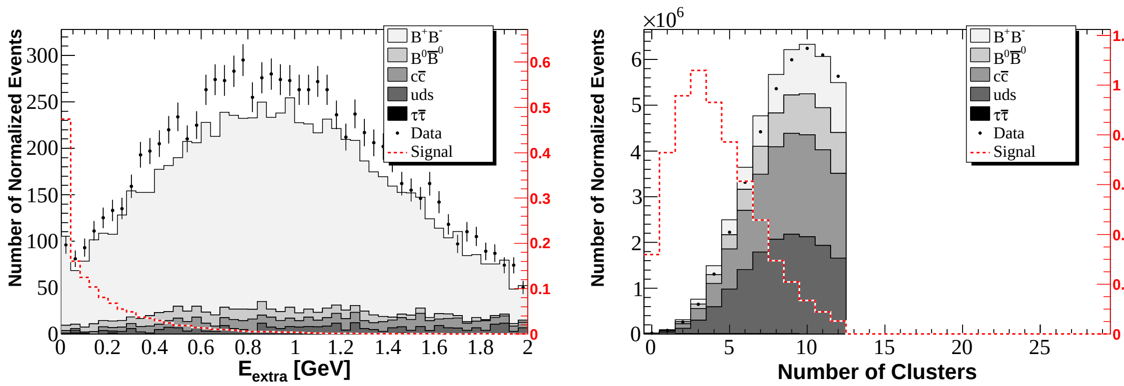

Figure 5–9: (left) The distribution of E_{extra} within the $B^+ \to \ell^+ \nu_\ell \gamma$ analysis, after applying all B_{tag} and track criteria, and (right) the distribution of the signal-side cluster multiplicity, after the B_{tag} reconstruction skim. These plots compare the data (points) with the generic background MC, and show the signal MC distribution (red dashed).

5.2 Signal Kinematics

5.2.1 Model-Dependent Kinematic Selection

This search for $B^+ \to \ell^+ \nu_\ell \gamma$ avoids kinematic restrictions on the energy of the signal-lepton and signal-photon candidates, and the only angular restriction, $\cos\theta_{\ell\nu}$, has excellent resolution due to the hadronic-tag reconstruction technique. Therefore, the resulting branching fraction measurement is essentially independent of the $B \to \gamma$ form-factor model over the full kinematic spectrum. However, one can also determine separate branching-fraction upper limits on the two $B^+ \to \ell^+ \nu_\ell \gamma$ theoretical models by exploiting the differences between the $f_A = f_V$ and $f_A = 0$ models. As shown in Figure 5–10, the energy distribution of the final-state particles, as well as the angles between them, are noticeably model-dependent. In the $f_A = 0$ model, the lepton energy spectrum is less peaked at high energies, and the photon and neutrino are much more likely to be back-to-back than in the $f_A = f_V$ model. Two of the three previous inclusive $B^+ \to \ell^+\nu_\ell\gamma$ analyses (see Section 4.1.1) had applied restrictions on $\cos\theta_{\gamma\ell}$, the cosine of the angle between the signal lepton and signal photon momenta, but Figure 5–11 indicates that such a requirement is directly correlated with applying a kinematic constraint on the lepton momentum.

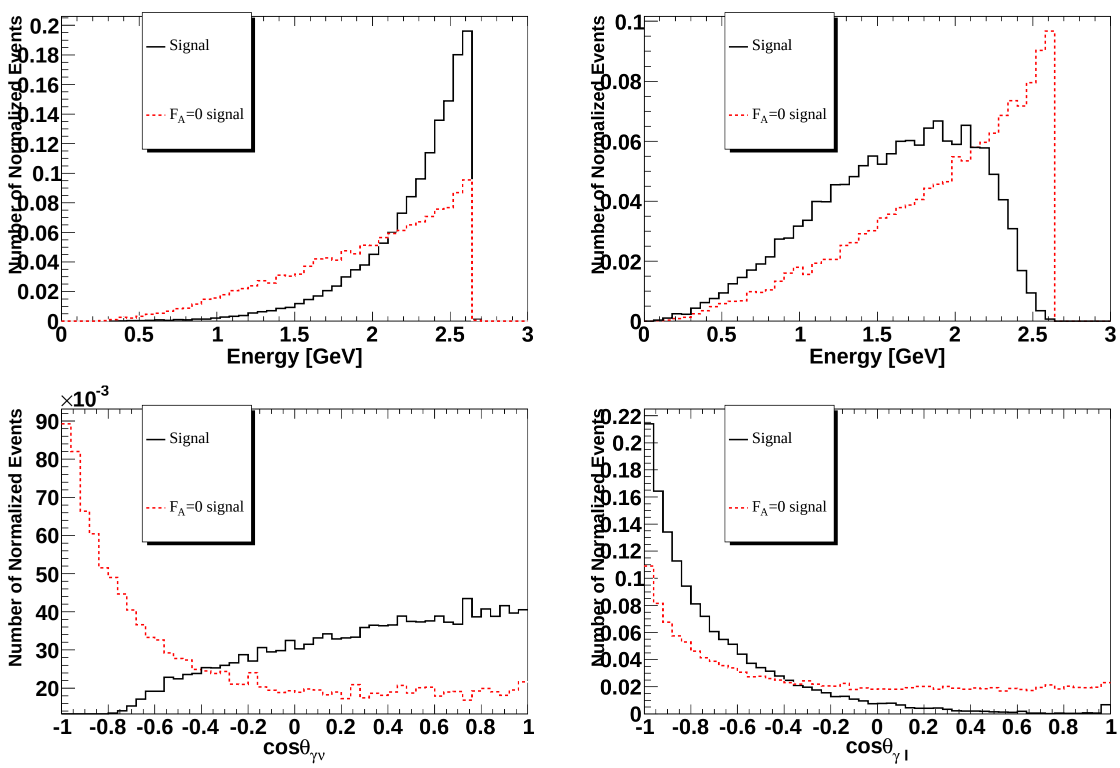

Figure 5–10: A comparison of true kinematic distribution within the two $B^+ \to \ell^+\nu_\ell\gamma$ signal MC samples, between the default $f_A = f_V$ model (solid) and the $f_A = 0$ model (dashed). (top) The energy distribution of the (left) lepton and (right) neutrino, and (bottom) the cosine of the angles between (left) the photon and neutrino and (right) the photon and lepton. These distributions are in the B_{sig} rest frame, after applying B_{tag} and track criteria, and determined using the MC particle-truth information. The energy distribution of the photon is consistent between the two models.

The relationship between the variables $\cos\theta_{\gamma\nu}$ and $\cos\theta_{\gamma\ell}$ are shown in Figure 5–12, where the former is the cosine of the angle between the signal photon and the missing momenta, and the latter is between the photon and lepton momenta. The

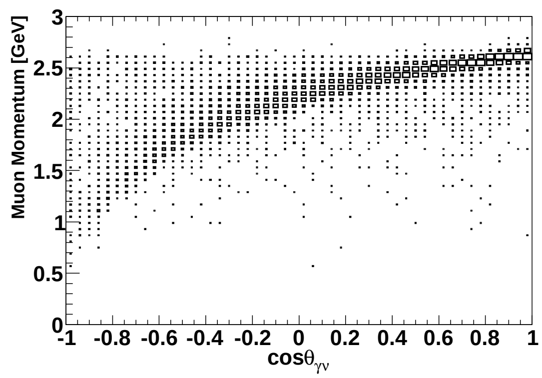

Figure 5–11: The two-dimensional distribution and correlation between the $\cos\theta_{\gamma\ell}$ variable and the signal-lepton candidate momentum. This plot only uses the default $f_A = f_V$ signal $B^+ \to \ell^+\nu_\ell\gamma$ MC after applying $B_{\rm tag}$ and track criteria. The size of the boxes represent the number of events within a given bin.

$f_A = f_V$ model tends to favor $B^+ \to \ell^+\nu_\ell\gamma$ decays in which the lepton decays back-to-back with the photon and neutrino ($\cos\theta_{\gamma\nu} \approx +1$, $\cos\theta_{\gamma\ell} \approx -1$). Conversely, the $f_A = 0$ model favors a photon that is emitted back-to-back with either the lepton or neutrino ($\cos\theta_{\gamma\nu} \approx \pm1$, $\cos\theta_{\gamma\ell} \approx \mp1$). The background events tend to populate the diagonal axis of the two-dimensional distribution, such that $\theta_{\gamma\nu} + \theta_{\gamma\ell} \approx 180°$ due to the $\cos\theta_{\ell\nu}$ requirement, which preferentially selects three-body events in which the lepton and neutrino are back-to-back.

Model-dependent regions are selected for model-specific branching fraction measurements, using equations based on the radius of an ellipse:

$$R_1 < (\cos\theta_{\gamma\ell} - 1)^2 + \frac{(\cos\theta_{\gamma\nu} + 1)^2}{3} \tag{5.2}$$

$$R_2 < (\cos\theta_{\gamma\nu} - 1)^2 + \frac{(\cos\theta_{\gamma\ell} + 1)^2}{3} \tag{5.3}$$

where the origin of each ellipse is at $\cos\theta_{\gamma\ell} = \pm1$ and $\cos\theta_{\gamma\nu} = \mp1$ and the major axis is three times as large as the minor axis. Events satisfying the $f_A = f_V$ model prediction are chosen such that Equation (5.2) is less than 0.4, which essentially only selects events in which $\cos\theta_{\gamma\ell} \approx -1$ and $\cos\theta_{\gamma\nu} \approx +1$. Events of the $f_A = 0$ model

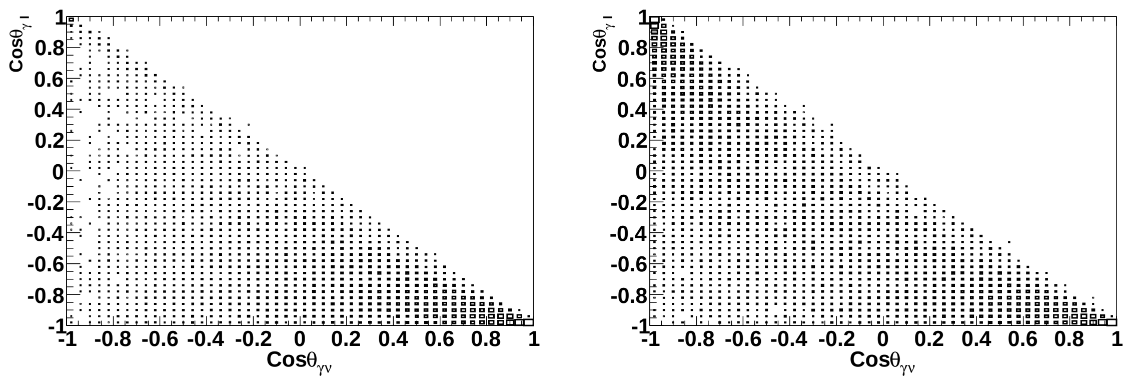

Figure 5–12: The two-dimensional distributions of $\cos\theta_{\gamma\nu}$ versus $\cos\theta_{\gamma\ell}$, which quantify the angles between the $B^+ \to \ell^+\nu_\ell\gamma$ final-state particles, for the (left) default $f_A = f_V$ signal MC and (right) $f_A = 0$ signal MC. These plots provide a comparison between the two signal MC samples, which tend to populate the corners. The size of the boxes represent the number of events within a given bin, after applying $B_{\rm tag}$ and track criteria.

are chosen such that either Equation (5.2) or Equation (5.3) are less than 0.4, which selects events in two signal regions.

5.3 Peaking Background Estimation

The only background that survives the full signal selection, according to the generic MC, are from B^+B^- decays. Of the B^+B^- background events that remain, almost all are due to $B^+ \to X_u^0\ell^+\nu_\ell$ events. This is due to the m_ν^2 and $\cos\theta_{\ell\nu}$ restrictions, which ensure kinematic and topological consistency with a three-body decay involving a massless and undetected particle: the neutrino. By further requiring that exactly one track recoils from a fully-reconstructed $B_{\rm tag}$, PID ensured that the track is a lepton. One possible decay that could mimic the signal is a mis-reconstructed $B^+ \to \pi^+\pi^0$, where the π^+ is mis-identified as a muon and one π^0 daughter photon travels within the detector's fiducial region but is undetected. However, these decays have a SM branching fraction of about 5.5×10^{-6} [2], which is of the same order as the $B^+ \to \ell^+\nu_\ell\gamma$ branching fraction predictions, and thus the probability of seeing such a poorly reconstructed event is negligible. Other decays with larger branching fractions can also pass the signal selection if they have a poorly-reconstructed $B_{\rm tag}$ candidate.

However, such combinatoric events can be estimated directly from the data in the m_{ES} sideband and are not considered m_{ES} "peaking" events. Therefore, only $B^+ \to \ell^+\nu_\ell\gamma$ decays peak within the m_{ES} signal region, unless the signal photon candidate actually arises from one or more particles that mimic the kinematics of $B^+ \to \ell^+\nu_\ell\gamma$, which occurs in specific pathological $B^+ \to X_u^0\ell^+\nu_\ell$ decays (as discussed in Section 5.1.3). The number of events that peak within the m_{ES} signal region (N_i^{peak} for each signal channel $i = e, \mu$) is estimated using several samples of exclusive $B^+ \to X_u^0\ell^+\nu_\ell$ MC, as described below. These exclusive MC samples add to the statistics of the generic background MC and thus reduce the uncertainty on the final peaking background estimate.

5.3.1 Peaking Background Monte Carlo

As listed in Table 3–4, this analysis uses a combination of exclusive $B^+ \to \pi^0\ell^+\nu_\ell$, $B^+ \to \eta\ell^+\nu_\ell$, and $B^+ \to \eta'\ell^+\nu_\ell$ MC samples in which the second B meson decays generically, as well as a $B \to X_u\ell\nu_\ell$ "cocktail" MC sample which is used to estimate $B^+ \to \omega\ell^+\nu_\ell$ events and other semileptonic X_u decays. In the *cocktail MC*, one charged or neutral B meson is generated to decay via $B \to X_u\ell\nu_\ell$, where here $\ell = e, \mu, \tau$, for a total of 19 $B^+ \to X_u^0\ell^+\nu_\ell$ resonance states per lepton mode. The second B meson decays via $D^{(*)0}X$ and $D^{(*)\pm}X$, where X is a combination of less than three pions or other light u-quark mesons. By having the second B meson decay to exclusive D-meson modes rather than generically, the B_{tag} reconstruction efficiency is increased, providing additional MC statistics for N_i^{peak} without having to generate as large a MC sample.

In order to normalize the cocktail MC to data luminosity for a background estimate of N_i^{peak}, one must account for the facts that neither B-meson decay is generic, and that the B_{tag} reconstruction efficiency will be, by design, significantly higher than that of a generic B-meson decay. Therefore, the cocktail MC is actually normalized to the generic B^+B^- MC, since the generic MC is already normalized to the data luminosity. This is achieved by using generator-truth information in the MC to remove all events from the generic MC except those generated with the same $B^\pm \to X_u^0 \ell^\pm \nu_\ell$ modes as in the cocktail sample (accounting for additional photons from initial and final state radiation). The B_{tag}, in both the generic and cocktail MC, must be charged and within the m_{ES} signal region to provide comparable samples of well-reconstructed events. Then, by assuming that both samples should have the same B_{tag} reconstruction efficiencies, the effective number of generated events in the cocktail sample (as if it had been produced with a generic B_{tag}) is determined. The cocktail MC is reweighted using this effective number of generated MC events, which is about 30 times larger than the actual number. This algorithm provides excellent agreement between the cocktail and generic MC samples when the statistics of $B^+ \to X_u^0 \ell^+ \nu_\ell$ events are high. When the statistics become lower, after more selection requirements are applied, the cocktail sample results are still consistent but significantly more precise than the generic MC results. There is also excellent agreement within the statistical uncertainties between the exclusive and cocktail MC samples in the $B^+ \to \pi^0 \ell^+ \nu_\ell$ and $B^+ \to \eta \ell^+ \nu_\ell$ modes, even at the end of the signal selection.

To improve the N_i^{peak} estimate, the branching fractions of the dominant $B^+ \to X_u^0 \ell^+ \nu_\ell$ modes are corrected in the exclusive, cocktail, and generic background MC samples to reflect up-to-date averages of recent experimental results. The generated and measured branching fractions for various modes are outlined in Table 5–1. Due to large discrepancies between the two published $B^+ \to \eta' \ell^+ \nu_\ell$ branching fraction measurements at the time of the analysis [76, 77], the branching fraction is set equal to $\mathcal{B}(B^+ \to \eta \ell^+ \nu_\ell)$ with an assumed relative uncertainty of 100%. In addition, due to the lack of measurements of the $B^+ \to X_u^0 \ell^+ \nu_\ell$ resonances with masses higher than η', the relative uncertainty on the other $B^+ \to X_u^0 \ell^+ \nu_\ell$ branching fractions is set to

50%. Within the $B^+ \to \ell^+\nu_\ell\gamma$ analysis, the largest systematic uncertainty on N_i^{peak} stems from branching fraction uncertainties of $B^+ \to X_u^0\ell^+\nu_\ell$ events .

Table 5–1: The branching fractions for the various $B^+ \to X_u^0\ell^+\nu_\ell$ modes, including the values used in generating the generic MC ($\mathcal{B}_{\text{genMC}}$) and the correct up-to-date measurement values used to weight the background MC samples ($\mathcal{B}_{\text{meas}}$). All branching fractions are given as ($\times 10^{-4}$).

Decay	$\mathcal{B}_{\text{genMC}}$	$\mathcal{B}_{\text{meas}}$
$B^+ \to \pi^0\ell^+\nu_\ell$	0.72	0.77 ± 0.12 [2]
$B^+ \to \eta\ell^+\nu_\ell$	0.84	0.64 ± 0.20 [76]
$B^+ \to \rho^0\ell^+\nu_\ell$	1.45	1.28 ± 0.18 [2]
$B^+ \to \omega\ell^+\nu_\ell$	1.45	1.3 ± 0.54 [78]
$B^+ \to \eta'\ell^+\nu_\ell$	0.84	0.64 ± 0.64
Other $B^+ \to X_u^0\ell^+\nu_\ell$ resonances	2.90	2.90 ± 1.45

In addition to the $B^+ \to X_u^0\ell^+\nu_\ell$ events which decay via resonances, there are also possible contributions from inclusive $b \to u\ell^+\nu_\ell$ non-resonant states. Although the generic background MC already models an inclusive spectrum, additional statistics are gained by consulting an inclusive $B \to X_u\ell\nu_\ell$ MC sample. This MC models a continuous invariant mass spectrum without any resonance production, based on Reference [79]. The inclusive branching fraction is taken from a BABAR measurement of $(22.7^{+4.5}_{-4.2}) \times 10^{-4}$ [79], and the branching fractions of the modeled resonances in Table 5–1 are subtracted from this value to obtain the inclusive $B \to X_u\ell\nu_\ell$ MC branching fraction weighting. This MC is considered relevant above the mass of about $1.5\,\text{GeV}/c^2$, since the spectrum below this is essentially modeled by the resonance structure in the exclusive and cocktail $B^+ \to X_u^0\ell^+\nu_\ell$ MC. The total number of expected N_i^{peak} events at the end of the signal selection is provided in Table 5–2. Ultimately, it is found that only four resonance decays significantly contribute to the peaking background in this analysis, while the other exclusive and inclusive $B \to X_u\ell\nu_\ell$ contributions are relatively negligible.

Table 5–2: The expected number of $B^+ \to X_u^0 \ell^+ \nu_\ell$ events in each signal mode after the full signal selection, the branching fraction corrections, and the form-factor reweighting discussed in Section 5.3.2. The uncertainties are only statistical.

Mode	Expected Events
$B^+ \to \pi^0 e^+ \nu_e$	1.96 $\pm$ 0.28
$B^+ \to \eta e^+ \nu_e$	0.52 $\pm$ 0.13
$B^+ \to \omega e^+ \nu_e$	0.17 $\pm$ 0.03
$B^+ \to \eta' e^+ \nu_e$	0.08 $\pm$ 0.05
Other $B^+ \to X_u^0 e^+ \nu_e$	0.01 $\pm$ 0.01
Total (e^+ mode)	2.74 $\pm$ 0.31
$B^+ \to \pi^0 \mu^+ \nu_\mu$	1.62 $\pm$ 0.27
$B^+ \to \eta \mu^+ \nu_\mu$	0.51 $\pm$ 0.13
$B^+ \to \omega \mu^+ \nu_\mu$	0.19 $\pm$ 0.03
$B^+ \to \eta' \mu^+ \nu_\mu$	0.05 $\pm$ 0.04
Other $B^+ \to X_u^0 \mu^+ \nu_\mu$	0.02 $\pm$ 0.01
Total (μ^+ mode)	2.39 $\pm$ 0.31

5.3.2 Peaking Background Form-Factors

In addition to branching fraction uncertainties, there are also theoretical uncertainties involved with the $B \to X_u$ form-factor in the matrix element of semileptonic X_u decays. The partial branching fraction of $B^+ \to \pi^0 \ell^+ \nu_\ell$, assuming massless leptons, can be written as [80]:

$$\frac{d\mathcal{B}(B \to \pi \ell \nu)}{dq^2} = \frac{G_F^2 |V_{ub}|^2 \tau_B}{24\pi^3} p_\pi^3 |f_+(q^2)|^2 \tag{5.4}$$

where p_π is the magnitude of the pion's three-momentum in the B-meson rest frame. The $B \to \pi$ form-factor ($f_+(q^2)$) depends on q^2, which is the four-momentum carried by the virtual $W^\pm$ boson. The background events that pass the signal selection are dominated by $B^+ \to \pi^0 \ell^+ \nu_\ell$ events with high q^2, corresponding to high-energy leptons and low-energy pions. However, $f_+(q^2)$ is a theoretically uncertain function, so its dependence on q^2 results in uncertain kinematic distributions, which leads to an uncertain number of $B^+ \to \pi^0 \ell^+ \nu_\ell$ events which ultimately contribute to N_i^{peak}.

Therefore, in order to adequately estimate N_i^{peak}, this analysis uses up-to-date theoretical models for the $B \to X_u$ form-factors, which is particularly important in the high-q^2 region.

The $B^+ \to \pi^0\ell^+\nu_\ell$, $B^+ \to \eta\ell^+\nu_\ell$, and $B^+ \to \eta'\ell^+\nu_\ell$ exclusive MC samples are generated with a flat distribution in q^2 and reweighted to produce the distributions predicted by various form-factor models. The cocktail and generic background MC are also reweighted. The generated q^2 of each event is calculated by subtracting the true four-momentum of the X_u from that of the B_{sig}, using the generator-truth information in the MC. The q^2 is then inputted into a BABAR software package [81], which includes the parameters of various form-factor models. The $B^+ \to \pi^0\ell^+\nu_\ell$ contribution is reweighted using a distribution based on the results from a 2006 BABAR measurement of $B^0 \to \pi^-\ell^+\nu_\ell$ [82]. Since isospin symmetry suggests that the interchange of u- and d-quarks will leave the quark distributions invariant, the form factor is expected to remain unchanged between $B^0 \to \pi^-\ell^+\nu_\ell$ and $B^+ \to \pi^0\ell^+\nu_\ell$ decays.[3] The 2006 analysis measured the fit parameter $\alpha_{\text{BK}} = 0.53 \pm 0.05(\text{stat}) \pm 0.04(\text{syst})$ to a theoretically-predicted q^2 distribution [83] that describes the data well. Figure 5–13 shows $d\mathcal{B}(B \to \pi\ell\nu_\ell)/dq^2$ as a function of q^2 for various theoretical form-factor models. The curve fitted to the data points in the plot is the assumed $B^+ \to \pi^0\ell^+\nu_\ell$ q^2 distribution in this $B^+ \to \ell^+\nu_\ell\gamma$ analysis.

In addition, all $B^+ \to \eta\ell^+\nu_\ell$ and $B^+ \to \eta'\ell^+\nu_\ell$ events in the exclusive, generic, and cocktail MC samples are reweighted to match the form-factor distribution predicted by a Light-Cone Sum Rule (LCSR) model from 2004 [53], shown in Figure 5–14

[3] According to isospin symmetry, the branching fraction ratio of $B^0 \to \pi^-\ell^+\nu_\ell$ to $B^+ \to \pi^0\ell^+\nu_\ell$ decays should be equal to $2\tau_{B^+}/\tau_{B^0}$, where $\tau_{B+,B0}$ are the lifetimes of the B^+ and B^0 meson, respectively.

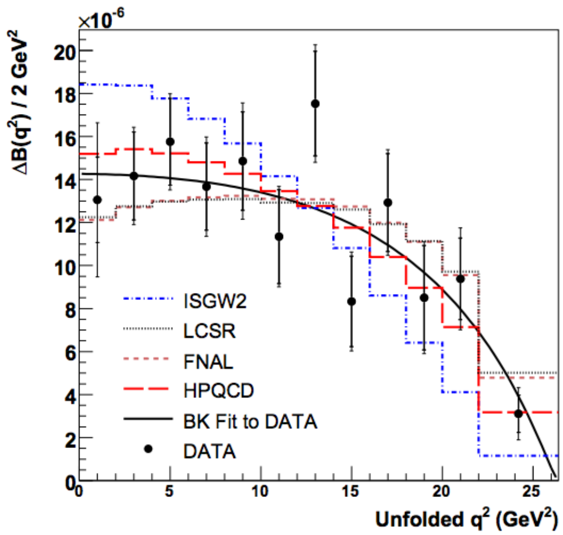

Figure 5–13: The measured data q^2 distribution of the form-factor shape for $B \to \pi\ell\nu_\ell$ (points), and a fit to the data (solid black) [82] which is used to reweight the $B^+ \to \pi^0\ell^+\nu_\ell$ MC events in this $B^+ \to \ell^+\nu_\ell\gamma$ analysis. In addition, the distribution of various other theoretical models is also provided for comparison, with citations provided in Ref. [82]. The two lattice QCD models (FNAL and HPQCD) are only considered reliable in the region $q^2 > 16\,\mathrm{GeV}^2$, and the LCSR model is valid for $q^2 < 16\,\mathrm{GeV}^2$.

as "Ball04". The reweighting parameters were not available at the time of this analysis to use the updated 2007 model "Ball07" [84]. However, the systematic uncertainty applied to the form-factor distribution accounts for this by using the Isgur-Wise model (ISGW2) [85] to bound the q^2 distribution, since the "Ball07" distribution lies almost halfway between the "Ball04" and ISGW2 models. Although the ISGW2 model has been disfavored as a description of the quark-level processes [86], it is still the model used to generate the generic and cocktail MC samples, and thus convenient to use. Since the other $B^+ \to X_u^0\ell^+\nu_\ell$ decays have relatively small contributions to the background, the uncertainties arising from using the ISGW2 model, without reweighting to the latest theoretical distributions, are considered negligible compared to those arising from the branching fraction uncertainties.

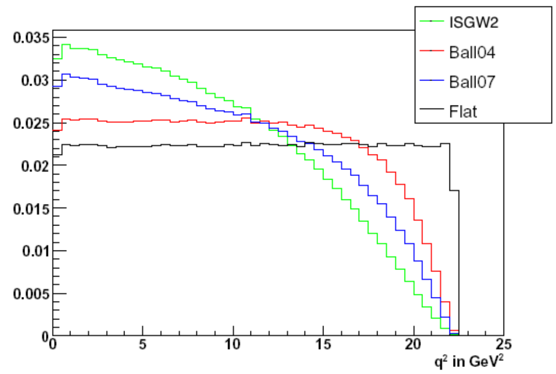

Figure 5–14: A comparison of the q^2 distributions of various $B^+ \to \eta^{(\prime)} \ell \nu_\ell$ form-factor models, as well as the flat-q^2 distribution (black) [87]. The "Ball04" LCSR model (red) is the assumed distribution within the $B^+ \to \ell^+ \nu_\ell \gamma$ analysis.

5.4 $B^+ \to \ell^+ \nu_\ell \gamma$ Selection Optimization

As discussed in Section 3.5.3, the signal selection values are optimized using the Punzi figure of merit. An iterative algorithm is employed to maximize this figure of merit, and to avoid localized maxima which may occur due to statistical fluctuations. The optimization is performed several times using various half-sized selections of the full MC samples, in order to further avoid optimization biases from low-statistics fluctuations. The $B^+ \to \ell^+ \nu_\ell \gamma$ analysis primarily determines $N^{\mathrm{MC}}_{\mathrm{bkg}}$ (of Equation (3.2)) from $B^+ \to X_u^0 \ell^+ \nu_\ell$ MC samples. Both signal channels are optimized together for the continuum likelihood, $\cos_{\ell\nu}$, lateral moment, and the model-dependent angular requirements, as well as the reconstruction values involved in the π^0, η, and ω vetoes. The m_ν^2 values and lepton PID selectors are optimized separately for each of the two signal channels. Both of the $B^+ \to \ell^+ \nu_\ell \gamma$ form-factor models result in the same optimized values.

5.5 Combinatoric Background Estimation

The background (N_i^{bkg} for each signal channel i) is divided into two categories: the number of events that peak in the m_{ES} signal region (N_i^{peak}, discussed in Section 5.3) and the number of combinatoric events from B_{tag} candidates that are incorrectly reconstructed from either continuum events or both B mesons (N_i^{comb}). Although one could estimate N_i^{comb} from MC (as is done for N_i^{peak}), this analysis reduces the systematic uncertainties from MC modeling of the continuum and combinatoric background distributions by directly using the data in the m_{ES} sidebands (SB) rather than relying on the MC estimates. This method also reduces the statistical uncertainty in the $B^+ \to \ell^+\nu_\ell\gamma$ analysis; since there are less than two generated continuum MC events for every expected continuum event in the data, the larger m_{ES} SB region can provide several times the statistics of the signal region. The m_{ES} signal region is defined in the $B^+ \to \ell^+\nu_\ell\gamma$ analysis as $5.27 < m_{\text{ES}} < 5.29\,\text{GeV}/c^2$, and the m_{ES} SB is defined as $5.20 < m_{\text{ES}} < 5.26\,\text{GeV}/c^2$. The data events within the region $5.26 < m_{\text{ES}} < 5.29$ GeV/c^2 and $m_\nu^2 < 1\,\text{GeV}^2/c^4$ were kept blinded until the analysis was complete.

The value of N_i^{comb} is estimated in the m_{ES} signal region using:

$$N_i^{\text{comb}} \equiv N_{\text{data}}^{SB} \cdot R_{\text{comb}} \tag{5.5}$$

where N_{data}^{SB} is the number of the data events within the SB, and the *Combinatoric Ratio* (R_{comb}) is the ratio of the number of non-peaking events in the m_{ES} signal region to the number of events in the m_{ES} SB. After the B_{tag} charge requirement, the entire continuum and $B^0\overline{B}^0$ MC samples are considered non-peaking and, therefore, their contribution to the Combinatoric Ratio is easily determined from the MC. On the other hand, correctly-charged B^+B^- events peak within the m_{ES} signal region, but they will still have a combinatoric contribution under the peak, which must be extrapolated. To do this, the B^+B^- MC (including the $B^+ \to X_u^0\ell^+\nu_\ell$ MC) is assumed to have the same combinatoric distribution shape as that from the mis-charged $B^0\overline{B}^0$ MC events (in other words, charged B_{tag} candidates reconstructed within the $B^0\overline{B}^0$ MC). Thus, the Combinatoric Ratio is found using:

$$R_{\text{comb}} \equiv \frac{N_{f\bar{f}}^{SR} + N_{B^0\overline{B}^0}^{SR} + (N_{B^+B^-}^{SB} \cdot R_{B^0\overline{B}^0})}{N_{f\bar{f}}^{SB} + N_{B^0\overline{B}^0}^{SB} + N_{B^+B^-}^{SB}} \tag{5.6}$$

$$R_{B^0\overline{B}^0} \equiv \frac{N^{SR}_{B^0\overline{B}^0}}{N^{SB}_{B^0\overline{B}^0}} \tag{5.7}$$

where N^{SR} (N^{SB}) is the number of events within the m_{ES} signal region (sideband), with the subscript referring to the MC sample used. The subscript $f\overline{f}$ refers to all continuum MC, specifically $e^+e^- \to u\overline{u}, d\overline{d}, s\overline{s}, c\overline{c}$, and $\tau^+\tau^-$. The ratio $R_{B^0\overline{B}^0}$ essentially quantifies the shape of the mis-charged B_{tag} candidates. Therefore, the term ($N^{SB}_{B^+B^-} \cdot R_{B^0\overline{B}^0}$) (in Equation (5.6)) determines the size of the B^+B^- combinatoric contribution within the signal region, by normalizing the mis-charged $B^0\overline{B}^0$ MC to the B^+B^- MC, both within the m_{ES} SB, which is depicted in the top left plot of Figure 5–15.

The exclusive and cocktail $B^+ \to X_u^0\ell^+\nu_\ell$ MC samples, which are used to determine N_i^{peak}, also include both a peaking and combinatoric component. Since the combinatoric component of the B^+B^- MC already accounts for the combinatoric contributions from $B^+ \to X_u^0\ell^+\nu_\ell$ decays, double-counting is avoided in the total background estimate ($N_i^{\text{peak}} + N_i^{\text{comb}}$) by subtracting out the combinatoric contribution within the exclusive and cocktail $B^+ \to X_u^0\ell^+\nu_\ell$ MC samples. Again, the assumed shape of this contribution is described by $R_{B^0\overline{B}^0}$ from Equation (5.7). Thus, the number of peaking background events is determined using:

$$N_i^{\text{peak}} \equiv (N^{SR}_{X_u^0\ell^+\nu_\ell} - N^{SB}_{X_u^0\ell^+\nu_\ell} \cdot R_{B^0\overline{B}^0}) \cdot C_{\text{yield}} \tag{5.8}$$

where $N_{X_u^0\ell^+\nu_\ell}$ is the number of events within the exclusive and cocktail $B^+ \to X_u^0\ell^+\nu_\ell$ MC samples. The B_{tag} *Yield Correction* (C_{yield}) corrects the MC normalization to more accurately match the data. This is done by using the ratio of the peaking-data yield to the peaking-MC yield:

$$C_{\text{yield}} \equiv \frac{N^{SR}_{\text{data}} - \left[N^{SR}_{f\overline{f}} - N^{SR}_{B^0\overline{B}^0} - (N^{SB}_{\text{data}} - N^{SB}_{f\overline{f}} - N^{SB}_{B^0\overline{B}^0}) \cdot R_{B^0\overline{B}^0}\right]}{N^{SR}_{B^+B^-} - (N^{SB}_{B^+B^-} \cdot R_{B^0\overline{B}^0})}. \tag{5.9}$$

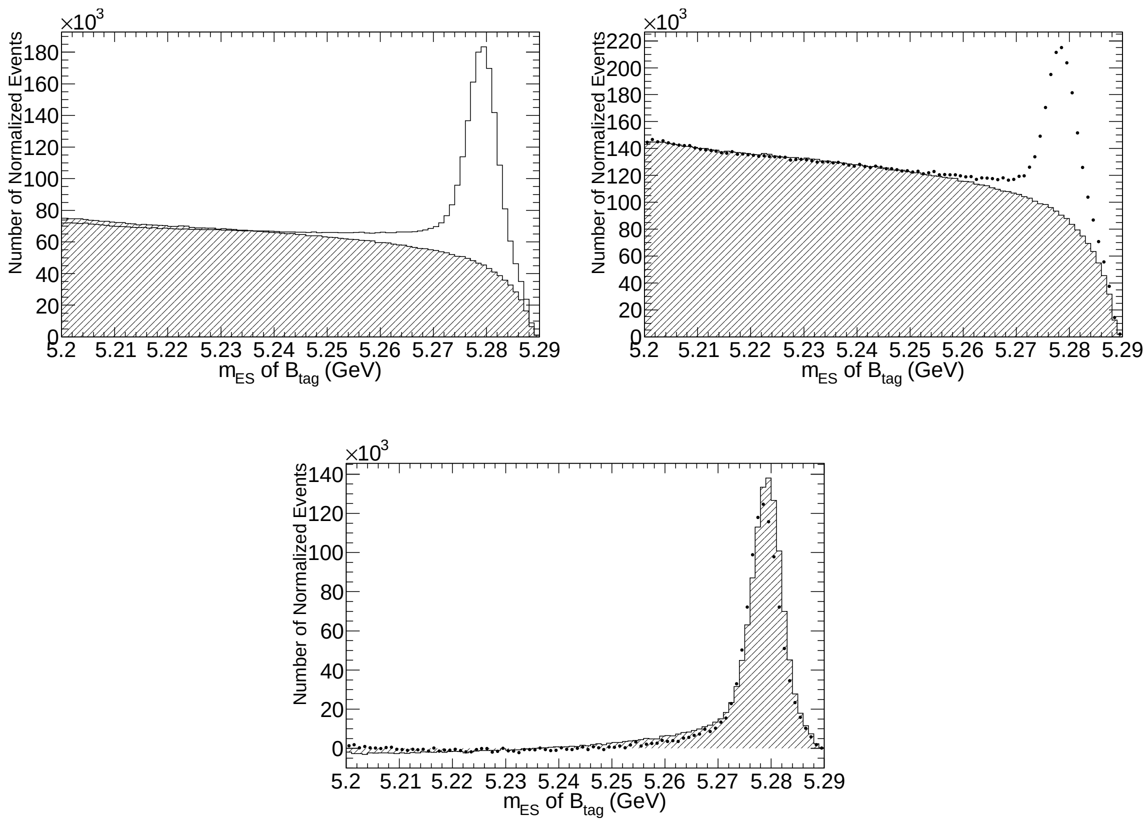

Figure 5–15: The distribution of $m_{\rm ES}$ demonstrating various steps in the determination of the combinatoric background estimation and $B_{\rm tag}$ Yield Correction: (left) the mis-charged $B^0\overline{B}^0$ combinatoric shape normalized to B^+B^- MC using $N^{SB}_{B^+B^-} \cdot R_{B^0\overline{B}^0}$ (shaded) and the $B^0\overline{B}^0$ MC (points); (right) the mis-charged $B^0\overline{B}^0$ combinatoric shape (shaded) and the extrapolated B^+B^- component ($N_{\rm data} - N_{f\bar{f}} - N_{B^0\overline{B}^0}$) within the data (points); (bottom) the peaking yield distributions of the data (points) and the B^+B^- MC (shaded).

where $(N^{SB}_{\text{data}} - N^{SB}_{f\bar{f}} - N^{SB}_{B^0\bar{B}^0})$ is the extrapolated B^+B^- size in the data, shown as the points in the right plot of Figure 5–15, and $R_{B^0\bar{B}^0}$ is used to estimate the combinatoric B^+B^- component of the data within the signal region, shown as the shaded region of the same plot. Thus, C_{yield} corrects the disagreement in the peaking-MC and peaking-data yields shown in the bottom plot of Figure 5–15.

The two $B^+ \to \ell^+\nu_\ell\gamma$ channels are combined to find a common set of R_{comb}, $R_{\text{B}^0\bar{\text{B}}^0}$, and C_{yield} ratios. Since the ratios suffer from low statistics and/or data-blinding near the end of the signal selection, the statistics are increased by determining the R_{comb} and $R_{\text{B}^0\bar{\text{B}}^0}$ ratios without the m^2_ν restriction (although all other signal selection criteria are applied). The C_{yield} ratio is determined after reconstructing a charged B_{tag} with less than ten signal-side tracks, and that passes the Continuum Likelihood requirement, but before applying any signal-side selection. The $B^+ \to \ell^+\nu_\ell\gamma$ analysis uses an $R_{\text{B}^0\bar{\text{B}}^0}$ value of 35.5%, a R_{comb} value of 30.8%, and a C_{yield} value of 90.7%.

5.6 Systematic Uncertainties

5.6.1 Branching Fraction and Form-Factor Uncertainties

The largest systematic uncertainty in the $B^+ \to \ell^+\nu_\ell\gamma$ analysis comes from the uncertainty of the form-factors and branching fractions of the $B^+ \to X^0_u\ell^+\nu_\ell$ events which form the N^{peak}_i estimate. The systematic due to the various $B^+ \to X^0_u\ell^+\nu_\ell$ branching fractions are determined by increasing the branching fraction values by one standard deviation, using the experimentally-measured values and uncertainties listed in Table 5–1. The difference in the estimated number of events is taken as the branching fraction systematic uncertainty for each $B^+ \to X^0_u\ell^+\nu_\ell$ channel.

The branching fraction uncertainties are large for most of the $B^+ \to X^0_u\ell^+\nu_\ell$ modes and, therefore, their form-factor uncertainties are comparatively negligible. However, this is not the case for $B^+ \to \pi^0\ell^+\nu_\ell$, the dominant contributor to N^{peak}_i. The decay modes $B^+ \to \pi^0\ell^+\nu_\ell$, $B^+ \to \eta\ell^+\nu_\ell$, and $B^+ \to \eta'\ell^+\nu_\ell$ are estimated using exclusive MC, with high statistics, that are generated using a flat-q^2. This distribution is ideal to reduce systematic effects associated with the form-factor reweighting, especially since the shape, resulting from various form-factor models, can differ by almost an order of magnitude in the high-q^2 region. The form-factor distribution of $B^+ \to \pi^0 \ell^+ \nu_\ell$ is taken from experimental data, which is parameterized as a value of α_{BK}, as discussed in Section 5.3.2. Therefore, the uncertainty on this form-factor distribution is found by varying the α_{BK} parameter by one standard deviation from the measured value, and taking the difference in the estimated number of $B^+ \to \pi^0 \ell^+ \nu_\ell$ events as the form-factor systematic uncertainty.

The "Ball07" form-factor model of $B^+ \to \eta \ell^+ \nu_\ell$ and $B^+ \to \eta' \ell^+ \nu_\ell$ decays lies approximately halfway between the ISGW2 and the "Ball04" models (see Figure 5–14), the latter of which is the assumed form-factor model in this analysis. Therefore, the form-factor is varied to that of the ISGW2 shape, and the systematic uncertainty is taken as half the relative difference in the expected background. Overall, the systematic uncertainties on the peaking background due to the branching fraction and form-factor models totals 13.7 (13.5)% within the electron (muon) channel.

5.6.2 m_ν^2 Uncertainties

The resolution of the m_ν^2 variable depends on the detector resolution of the signal-photon energy, signal-lepton momentum, and the four-momenta of the reconstructed B_{tag} daughters. Since the signal lepton is well-tracked within the detector, while the four-momentum of the photon candidate is determined only from the calorimeter and an approximate vector direction from the interaction region, the photon kinematics are assumed to have the limiting resolution. Therefore, to determine the systematic uncertainty from detector resolution modeling, the energy of all signal-photon candidates (E_γ) is smeared with a Gaussian of a width $1.9\% \times E_\gamma$, corresponding to the resolution uncertainty of the EMC at high E_γ, as given in Section 3.3.4. The *relative* *difference* on the efficiency is defined as:

$$\frac{\delta_\epsilon}{\epsilon} = \frac{|\epsilon_{MC} - \epsilon'_{MC}|}{\epsilon_{MC}} \tag{5.10}$$

where ϵ_{MC} is the efficiency in the MC, and ϵ'_{MC} is the varied efficiency for the systematic study which, for m_ν^2, is after the E_γ-smearing. The average δ_ϵ/ϵ over 1000 *Toy MC experiments*, in which fake data is simulated directly from a specific fit model, is taken as the m_ν^2 systematic uncertainty. Since the differing kinematics in the signal and $B^+ \to X_u^0 \ell^+ \nu_\ell$ decays result in differing m_ν^2 distributions, separate systematic uncertainties are determined for the signal efficiency and N_i^{peak}. In addition, because the $B^+ \to e^+\nu_e\gamma$ channel has a looser m_ν^2 window as compared to $B^+ \to \mu^+\nu_\mu\gamma$, each channel has a separate systematic associated with it. The m_ν^2 systematic is estimated at 0.43 (0.63)% for the $B^+ \to e^+\nu_e\gamma$ ($B^+ \to \mu^+\nu_\mu\gamma$) signal efficiencies, and 1.4% for the $B^+ \to X_u^0 \ell^+ \nu_\ell$ peaking background.

5.6.3 Combinatoric Ratio Uncertainty

The value of the Combinatoric Ratio, R_{comb}, relies on the shape of the combinatoric background, which is extrapolated from MC. The uncertainty of this shape assumption is estimated by recalculating the R_{comb} ratio using the assumption that the combinatoric component in the B^+B^- MC has the same shape as the continuum distribution, rather than the mis-charged $B^0\overline{B}^0$ distribution. This is simply done by replacing all instances of $R_{B^0\overline{B}^0}$ in Equations (5.6)–(5.9) with:

$$R_{f\bar{f}} \equiv \frac{N_{f\bar{f}}^{SR}}{N_{f\bar{f}}^{SB}}. \tag{5.11}$$

The relative difference between the resulting R_{comb} values is taken as the systematic uncertainty. Even though this results in a generously large systematic uncertainty of 14.6%, it is still smaller than the statistical uncertainty of $\sqrt{N_{\text{data}}^{SB}}$ =100 (50)% from the 1 (4) SB data events in the $B^+ \to e^+\nu_e\gamma$ ($B^+ \to \mu^+\nu_\mu\gamma$) channels.

5.6.4 Additional Uncertainties

The uncertainty of the B_{tag} Yield Normalization, C_{yield}, is determined by adding in quadrature the change in C_{yield} due to: varying the lower bound of the m_{ES} signal region, varying the sideband size and bounds, determining C_{yield} at various stages of the signal selection, and using either the continuum or mis-charged $B^0\overline{B}^0$ combinatoric shapes. The C_{yield} uncertainty is estimated to be 3.1%.

Because the Continuum Likelihood requirement is applied before normalizing the MC to the data with C_{yield}, any systematic uncertainties resulting from the modeling of the Continuum Likelihood distribution are implicitly included. However, because the $B\overline{B}$ PDFs were determined using the $B^+ \to K^+\nu\overline{\nu}$ MC and not the $B^+ \to \ell^+\nu_\ell\gamma$ MC, the signal PDF shapes inputted into Equation (4.3) are redefined using the $B^+ \to \ell^+\nu_\ell\gamma$ MC, as depicted in Figure 5–16. The systematic uncertainty associated with the $B\overline{B}$ shape is then taken as half the difference between the two likelihood results, giving a relative difference of 1.4%.

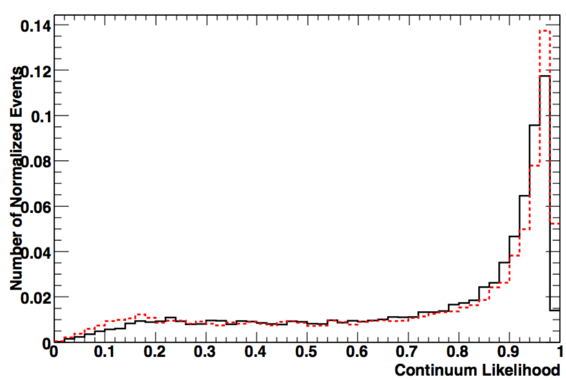

Figure 5–16: The comparison of two Continuum Likelihood distributions, after all other signal selection criteria are applied, within the signal $B^+ \to \ell^+\nu_\ell\gamma$ MC. The default likelihood used in the analysis is defined using $B^+ \to K^+\nu\overline{\nu}$ signal MC (solid) and the likelihood used to determine the systematic uncertainty is defined using the $B^+ \to \ell^+\nu_\ell\gamma$ MC (dashed).

Because the $B^+ \to \ell^+\nu_\ell\gamma$ signal selection requires exactly one track, an additional systematic uncertainty arises due to the tracking efficiency within the detector. Using a collaboration-wide recipe for high p_T tracks ($> 0.2\,\text{GeV}$) and low multiplicity events, this is estimated at 0.36% per track. Although a signal event can have a high multiplicity if one includes the B_{tag} tracks, any systematic effects from the tracking efficiency on the B_{tag} side is already incorporated into the C_{yield} normalization correction. Therefore, the requirement of one signal-side track contributes to a tracking uncertainty of 0.36%.

Likewise, there is a systematic contribution on the efficiency of identifying a cluster that is not a daughter of a π^0. Using a collaboration-wide recipe, which is valid for selecting photons with energies between 0.030 and 2.5 GeV, this uncertainty is estimated to be 1.8%.

In order to improve the agreement between data and MC, a "PID Tweaking" algorithm is employed within the *BABAR* MC simulation. This algorithm modifies the MC output to improve its agreement with the data, specifically the agreement of the modeled PID-selector efficiencies and fake rates. This is done either by randomly rejecting accepted tracks in the MC or by randomly selecting rejected ones. Therefore, the systematic uncertainty from the PID is determined by comparing the final efficiencies in the signal MC samples with and without this PID Tweaking, resulting in a relative difference of 0.93 (1.3)% for the electron (muon) channel.

5.6.5 Control Sample

To verify the modeling of the signal efficiency, a control sample is used. *Control samples* select data events from specific decays with relatively large branching fractions in order to provide a high-statistics comparison with the MC. These events are selected using similar requirements as for signal decays but, in some way, are also orthogonal such that the signal data can remain blinded. These samples can also validate the normalization of the background estimates, as the data yield of the control sample, corrected for background contamination, should coincide with the number of expected events given the well-measured branching fractions of the control sample decay.

A control sample of $B^+ \to \pi^0 \ell^+ \nu_\ell$ is used, since these decays have similar kinematics and topology to the signal decay, as evidenced by the fact that they are the dominant background in this analysis. The control sample is completely orthogonal to the $B^+ \to \ell^+ \nu_\ell \gamma$ final selection; using the same requirements as in the $B^+ \to \pi^0 \ell^+ \nu_\ell$ veto, the control sample requires that a π^0 candidate can be formed using the signal photon candidate, and rejects all other events. The m_ν^2 and $\cos\theta_{\ell\nu}$ variables are constructed using the π^0 four-momentum in place of the signal-photon candidate four-momentum, and both π^0 photon energies are subtracted from the E_{extra} variable. Other than the $B^+ \to \eta \ell^+ \nu_\ell$ and $B^+ \to \omega \ell^+ \nu_\ell$ vetoes, all other signal selection criteria are applied, including the C_{yield} correction. The m_ν^2 peak of the control sample, shown in Figure 5–17, resembles that of $B^+ \to \ell^+ \nu_\ell \gamma$ such that the data peaks at zero within the m_ν^2 signal region. A $B^+ \to \pi^0 \ell^+ \nu_\ell$ yield of 44 data events is observed within the m_ν^2 signal regions. The MC agrees with the data within the 15% statistical uncertainty of the data. As a cross-check, the $B^+ \to \pi^0 \ell^+ \nu_\ell$ branching fraction is determined (using Equation (5.12), which will be discussed in Section 5.7). The peak in the control sample corresponds to $\mathcal{B}(B^+ \to \pi^0 \ell^+ \nu_\ell)$=($0.78^{+1.7}_{-1.1} \times 10^{-4}$), where the uncertainties are only statistical. This is consistent with the current world-average value of $(0.77 \pm 0.12) \times 10^{-4}$ [2], which is also the assumed $B^+ \to \pi^0 \ell^+ \nu_\ell$ branching fraction in this analysis.

5.7 Branching Fraction Extraction

This analysis uses the *cut-and-count* technique of branching fraction extraction, which involves merely counting the number of expected background events ($N_i^{\mathrm{bkg}} = N_i^{\mathrm{peak}} + N_i^{\mathrm{comb}}$) and observed data events within the signal region (N_i^{obs}) to determine the number of signal events (N_i^{sig}) present in the data. A branching fraction is measured for both of the individual $B^+ \to \ell^+ \nu_\ell \gamma$ channels, as well as a combined branching fraction for $B^+ \to \ell^+ \nu_\ell \gamma$. The signal branching-fraction central

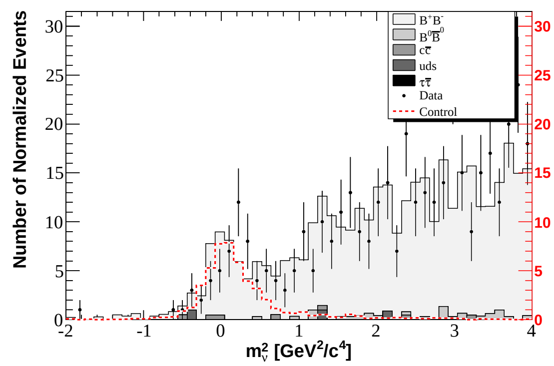

Figure 5–17: The distribution of m_ν^2 within the $B^+ \to \pi^0\ell^+\nu_\ell$ control-sample selection. This plot compares the data (points) with the generic background MC, and shows the expected distribution from the exclusive $B^+ \to \pi^0\ell^+\nu_\ell$ MC (red dashed), normalized to $\mathcal{B} = 0.77 \times 10^{-4}$.

value is calculated for each signal channel i using:

$$\mathcal{B}_i = \frac{N_i^{\mathrm{obs}} - N_i^{\mathrm{bkg}}}{\epsilon_i^{\mathrm{sig}} N_{B\bar{B}}} \tag{5.12}$$

where $\epsilon_i^{\mathrm{sig}}$ is the total signal efficiency and $N_{B\bar{B}} = (465.04 \pm 5.12) \times 10^6$ is the number of $B\overline{B}$ events produced in the data sample. The input values for Equation (5.12) will be provided in Table 5–3.

For an observed signal, one can find the statistical significance from the null hypothesis (zero signal events) by finding the one-sided probability (α) that N_i^{bkg} events would fluctuate to N_i^{obs}. The probability is then inputted into the equation [2]:

$$1 - 2\alpha = \mathrm{erf}\left(\frac{\delta}{\sqrt{2}}\right) \tag{5.13}$$

where δ is the number of standard deviations, measured in σ. The probability is calculated by taking the integral of a Poisson distribution, of mean N_i^{bkg}, from N_i^{obs} to infinity. The value of N_i^{bkg} is smeared using a Gaussian distribution with a width taken as the uncertainty on N_i^{bkg}. The two signal channels are combined by summing their N_i^{bkg} and N_i^{obs} values, and adding in quadrature the uncertainties on N_i^{bkg}. If an analysis sees an insignificant number of signal events with respect to the background levels, one cannot actually claim the measurement of a branching fraction with the necessary statistical significance (typically required to be at least 3σ). Instead, one can place one-sided upper limits on the branching fractions of these processes.

The upper limits of the branching fractions are initially computed using two different frequentist[4] methods. The straight-forward "Barlow" method [89] determines the upper limits by assuming Poisson-like statistical fluctuations. In other words, one can draw a Poisson distribution with a mean of μ to describe the probability that μ expected data events can fluctuate to the observed number $N_i^{\rm obs}$. The value of the expected number of events μ can be written as:

$$\mu = \mathcal{B}_i \epsilon_i^{\rm sig} N_{B\bar{B}} + N_i^{\rm bkg} \tag{5.14}$$

The values of $\epsilon_i^{\rm sig}$ and $N_i^{\rm bkg}$ are smeared using a Gaussian distribution with a width equal to their respective uncertainties, and the smeared values are required to be positive. The upper limit of $\mathcal{B}_i$ is found using a series of Toy MC experiments with various trial values of $\mathcal{B}_i$. A value n is generated from a Poisson distribution with mean μ ($P(n,\mu)$). The upper limit at 90% confidence level (CL) is then found to be the trial value of $\mathcal{B}_i$ such that [89]:

$$\alpha = \sum_{n=0}^{N_i^{\rm obs}} P(n,\mu) \tag{5.15}$$

where $1-\alpha = 90\%$ or, in other words, 10% of all Toy MC experiments gives $n \leq N_i^{\rm obs}$. Since $B^+ \to e^+\nu_e\gamma$ and $B^+ \to \mu^+\nu_\mu\gamma$ are expected to have equal branching fractions (aside from small phase-space effects), one can combine the results of the two channels

[4]Frequentist statistics treat probabilities as an objective summary of the relative frequency of an event within a large number of trials. Conversely, Bayesian statistics factor in subjectively-assumed or prior-measurement values [88].

by using a maximum likelihood defined as a product of the Poisson distributions (P):

$$\mathcal{L} = \prod_i P(n_i|\mu_i) = \prod_i \frac{\mu_i^{n_i} e^{-\mu_i}}{n_i!} \tag{5.16}$$

The values of $\mathcal{B}_i$ are then scanned to find the one that maximizes $\mathcal{L}$, and then Toy MC experiments are again employed to find the upper limit of $\mathcal{B}_i$.

Unfortunately, if the number of observed events is less than that of expected background events, the resulting upper limits using the above technique can be negative and thus unphysical. Therefore, the $B^+ \to \ell^+\nu_\ell\gamma$ analysis actually determines the upper limits using the "Feldman-Cousins" method [90], which is specifically designed to provide only positive upper limits by using the likelihood ratio:

$$R = \frac{P(n|\mu)}{P(n|\mu_{best})} \tag{5.17}$$

where P is the Poisson probability for observing $n = N_i^{\text{obs}}$ events, given a mean of μ. The variable μ_{best} is the value of μ which maximizes $P(n|\mu)$. Thus, R is the ratio of the likelihood of obtaining n, given the actual mean, and the likelihood of obtaining n, given the best-fit physically-allowed mean. This likelihood ratio is used to "rank" the possible $\mathcal{B}_i$ values to determine the 90% CL acceptance region. Again, this procedure is performed using Toy MC experiments, and the uncertainties are accounted for by smearing the N_i^{bkg} and ϵ_i^{sig} values using a Gaussian distribution. Finally, the uncertainties on the branching-fraction central values are determined using similar algorithms, but with the confidence interval set to one standard deviation (68%).

5.8 $B^+ \to \ell^+\nu_\ell\gamma$ Results

The SM-predicted branching fraction for $B^+ \to \ell^+\nu_\ell\gamma$ ranges between 0.32×10^{-6} and 5×10^{-6}. Based on the signal efficiency, this analysis expects to observe at least one signal event in either channel if the branching fraction is above 1.35×10^{-6}. Upon unblinding the data, a total of four events are present in the $B^+ \to e^+\nu_e\gamma$ channel and seven events in the $B^+ \to \mu^+\nu_\mu\gamma$ channel, both in slight excess of the expected number of background events. Although it is reasonable to suppose these events might be due to the presence of signal events, the statistical significance in both channels combined is 2.1σ from the hypothesis of zero signal events, which is not considered large enough to claim evidence of the signal decay. Therefore, upper limits at 90% CL are determined using the Feldman-Cousins method. The resulting branching-fraction central values and upper limits are provided in Table 5–3.

Table 5–3: The expected $B^+ \to \ell^+\nu_\ell\gamma$ background yields ($N_i^{\rm bkg} = N_i^{\rm comb} + N_i^{\rm peak}$), signal efficiencies ($\epsilon_i^{\rm sig}$), number of observed data events ($N_i^{\rm obs}$) and their corresponding significance, and the resulting branching-fraction limits at 90% CL. The average central value ($\mathcal{B}_{combined}$) and combined limits are also provided. Uncertainties are given as statistical ± systematic.

	$B^+ \to e^+\nu_e\gamma$	$B^+ \to \mu^+\nu_\mu\gamma$
$N_i^{\rm comb}$	$0.3 \pm 0.3 \pm 0.1$	$1.2 \pm 0.6 \pm 0.6$
$N_i^{\rm peak}$	$2.4 \pm 0.3 \pm 0.4$	$2.1 \pm 0.3 \pm 0.3$
$N_i^{\rm bkg}$	$2.7 \pm 0.4 \pm 0.4$	$3.4 \pm 0.7 \pm 0.7$
$\epsilon_i^{\rm sig}$	$(7.8 \pm 0.1 \pm 0.3)\times 10^{-4}$	$(8.1 \pm 0.1 \pm 0.3)\times 10^{-4}$
$N_i^{\rm obs}$	4	7
Significance	1.17σ	1.83σ
Limits	$< 17 \times 10^{-6}$	$< 26 \times 10^{-6}$
Combined Limits	$< 15.6 \times 10^{-6}$	
$\mathcal{B}_{\rm combined}$	$\left(6.5^{+7.6+2.8}_{-4.7-0.8}\right) \times 10^{-6}$	

These branching fraction results also put a lower limit on the value of λ_B, the first inverse moment of the B-meson distribution amplitude. As discussed in Section 2.3, this value ranges in the theoretical literature from 150–700 MeV [41, 40, 42, 43]. From Equation (5.12), and assuming $m_B = 5.279\,\mathrm{GeV}/c^2$, $m_b = 4.20\,\mathrm{GeV}/c^2$, $\tau_B = 1.638\,\mathrm{ps} \approx 2.489 \times 10^{12}\,\mathrm{GeV}^{-1}$, $|V_{ub}| = (3.93 \pm 0.36) \times 10^{-3}$ [2], and $f_B = 0.216 \pm 0.022\,\mathrm{GeV}$ [27], the value of λ_B can be calculated as:

$$\lambda_B = \frac{2}{3}\left(\sqrt{\frac{288\pi^2 \cdot \mathcal{B}(B^+ \to \ell^+\nu_\ell\gamma)}{\alpha G_F^2 |V_{ub}|^2 f_B^2 m_B^5 \tau_B}} - \frac{1}{3m_b}\right)^{-1} \tag{5.18}$$

The probability density function of $\mathcal{B}(B^+ \to \ell^+\nu_\ell\gamma)$, which peaks at the branching-fraction central value, is found using Toy MC experiments. These experiments combine the PDFs of the two signal channels, each obtained using Equation (5.12) with N_i^{obs} modeled as a Poisson distribution and ϵ_i^{sig} and N_i^{bkg} as Gaussian distributions. The $\mathcal{B}(B^+ \to \ell^+\nu_\ell\gamma)$ PDF is then inputted into Equation (5.18), and the uncertainty on $f_B^2|V_{ub}|^2$ is included by assuming Gaussian uncertainties. This results in the PDF of λ_B, which is shown in Figure 5–18. The lower limit on λ_B, taken as the value such that 90% of the PDF's integral lies above it, is determined to be 300 MeV.

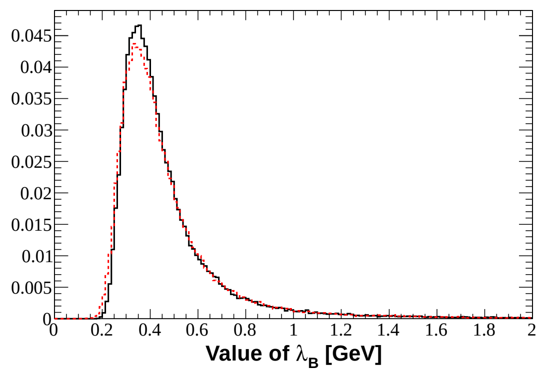

Figure 5–18: The Probability Density Function of the first inverse moment of the B-meson distribution amplitude, as defined in Equation (5.18), with (solid) and without (dashed) uncertainties on f_B and V_{ub}. This PDF is used to determine the λ_B lower limit.

A validation study on the unblinded data events has been performed in order to justify that the observed data adequately agrees with the expected results within various variable distributions, and that no obvious systematic uncertainty has been overlooked. Such results would typically manifest as an excess of continuum-like events or events hugging the edges of a signal region. Therefore, the combinatoric background, peaking background MC, and signal MC are studied using a variety of variables to find any excesses that are likely due to poor background estimates. The m_ν^2 distribution of the data events is shown in Figure 5–19, with signal events expected to peak around zero. In addition, the phase-space distribution, of the lepton- versus photon-candidate energies, is shown in Figure 5–20, which is generally consistent with the background expectations, although there are a few events which could be actual signal $B^+ \to \ell^+\nu_\ell\gamma$ decays.

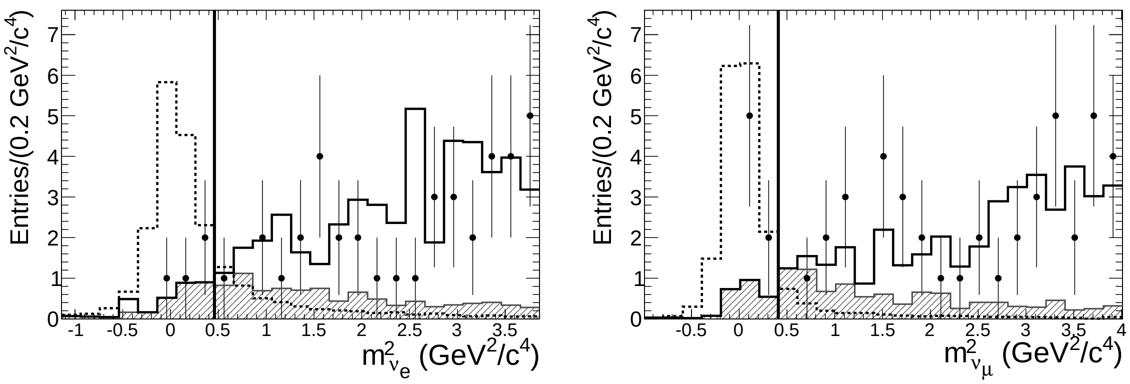

Figure 5–19: The distribution of m^2_ν after the full signal selection in the (left) $B^+ \to e^+\nu_e\gamma$ and (right) $B^+ \to \mu^+\nu_\mu\gamma$ channels. The non-peaking background contribution (solid) is added atop the m_{ES}-peaking background component (shaded) and overlayed with the data (points). The signal MC (dashed) is normalized to $\mathcal{B} = 40 \times 10^{-6}$. Events to the left of the vertical lines are selected.

5.8.1 Model-Dependent Results

The two model-specific requirements on the angular distribution of $\cos\theta_{\gamma\nu}$ and $\cos\theta_{\gamma\ell}$ (discussed in Section 5.2.1), provide a secondary set of branching-fraction upper limits for theoretical studies. There are zero observed data events within the default $f_A = f_V$ model, which results in more stringent upper limits on the branching fraction, and there are a total of five data events in the alternative $f_A = 0$ model, as outlined in Table 5–4.

Thus, the $f_A = 0$ model may appear to be more favored by the data, which is contrary to most of the theoretical literature, but the statistical uncertainty on the data sample is too large to permit a robust statement regarding a favored model. The angular distribution of the observed data and expected background and signal events are shown in Figure 5–21.

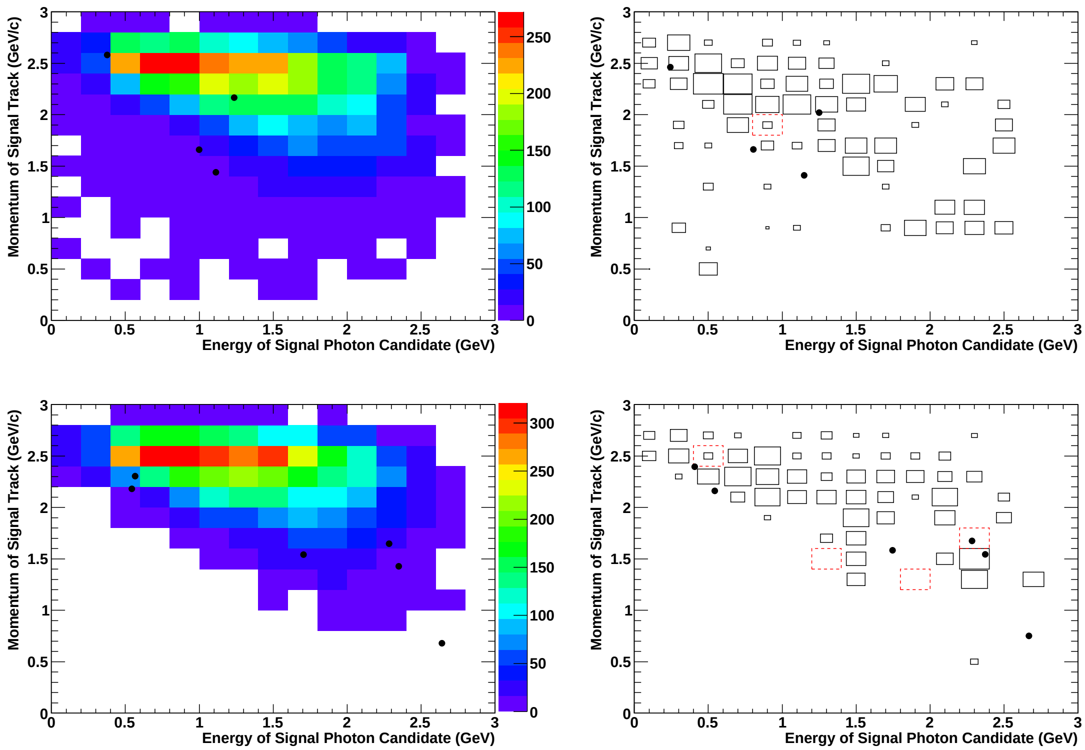

Figure 5–20: The phase-space distribution in (top) $B^+ \to e^+\nu_e\gamma$ and (bottom) $B^+ \to \mu^+\nu_\mu\gamma$ channels after the final signal selection. The plots provide comparisons of the distributions in the signal MC (colored distribution in left plot), peaking background MC (black boxes in right plot), combinatoric background from data SB (red boxes, not to scale with the black boxes), and observed data (points).

Due to the observation of less events in the $f_A = f_V$ model than the expected background, the central value of the resulting branching fraction is negative. This is a result of using a frequentist method of measurement, with no Bayesian priors assumed. Although a negative branching fraction is unphysical, the upper limits are required to be positive through the use of the Feldman-Cousins method.

Table 5–4: The results for the two $B^+ \to \ell^+\nu_\ell\gamma$ model-specific angular regions, including the expected background yields (N_i^{bkg}), signal efficiencies ($\epsilon_i^{\mathrm{sig}}$), number of observed data events (N_i^{obs}), and the resulting branching-fraction upper limits at 90% CL. Uncertainties are given as statistical ± systematic.

	$B^+ \to e^+\nu_e\gamma$	$B^+ \to \mu^+\nu_\mu\gamma$
	$f_A = f_V$ model	
$\epsilon_i^{\mathrm{sig}}$	$(4.9 \pm 0.2) \times 10^{-4}$	$(5.2 \pm 0.2) \times 10^{-4}$
N_i^{bkg}	0.6 ± 0.1	1.0 ± 0.4
N_i^{obs}	0	0
Limits	$< 8.4 \times 10^{-6}$	$< 6.7 \times 10^{-6}$
Combined Limits	$< 3.0 \times 10^{-6}$	
$\mathcal{B}_{\mathrm{combined}}$	-8.6×10^{-6}	
	$f_A = 0$ model	
$\epsilon_i^{\mathrm{sig}}$	$(4.6 \pm 0.2) \times 10^{-4}$	$(4.5 \pm 0.2) \times 10^{-4}$
N_i^{bkg}	1.3 ± 0.4	1.5 ± 0.6
N_i^{obs}	3	2
Limits	$< 29 \times 10^{-6}$	$< 22 \times 10^{-6}$
Combined Limits	$< 18 \times 10^{-6}$	
$\mathcal{B}_{\mathrm{combined}}$	$(5.6^{+7.4+1.7}_{-3.7-1.4}) \times 10^{-6}$	

5.8.2 High E_γ Branching Fraction

Since the photon energy distribution is theoretically uncertain, particularly at low energies, it is important to ensure that the signal efficiency is relatively flat over the full photon energy spectrum in order to claim that the results of this analysis are truly model independent. Figure 5–22 shows the total signal-side efficiency ($\epsilon_i^{\mathrm{sig}}$ divided by the B_{tag} reconstruction efficiency) as a function of a lower-bound restriction on the energy of the signal photon (E_γ) in the B_{sig} rest frame. Since signal events are more likely to be well-reconstructed when E_γ is high, the signal efficiency tends to increase with higher photon energies, but otherwise, the signal efficiency is relatively

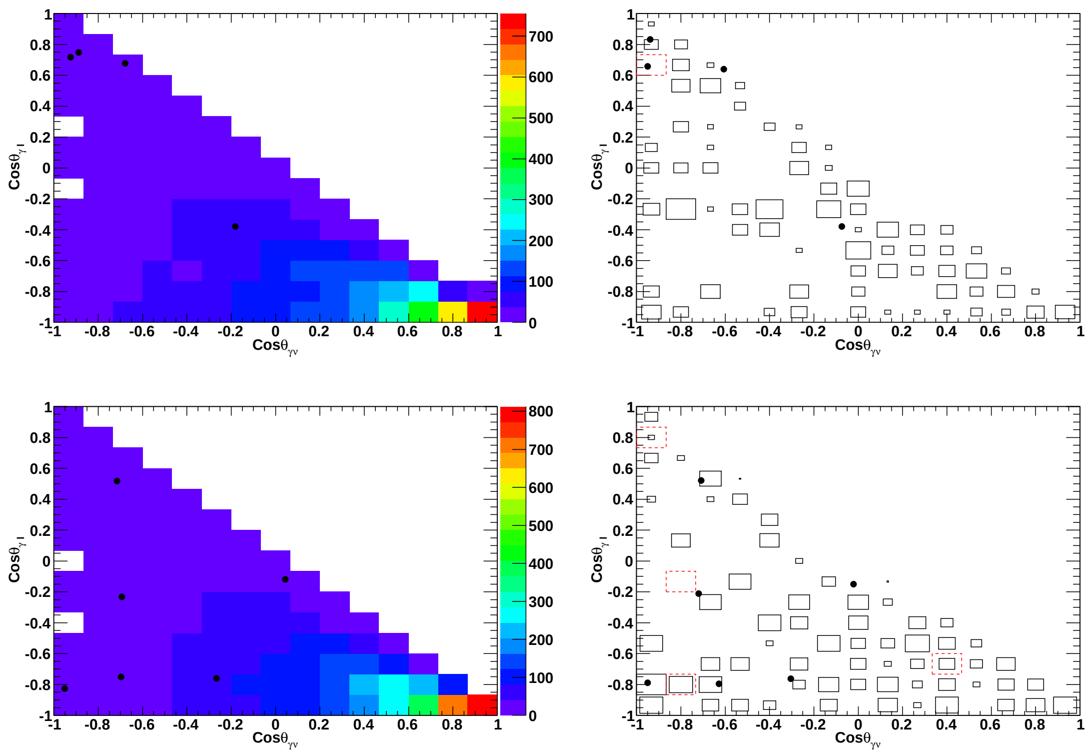

Figure 5–21: The angular distribution of $\cos\theta_{\gamma\nu}$ and $\cos\theta_{\gamma\ell}$ in (top) $B^+ \to e^+\nu_e\gamma$ and (bottom) $B^+ \to \mu^+\nu_\mu\gamma$ channels after the final model-independent signal selection. The plots provide comparisons of the distributions in the signal MC (colored distribution in left plot), peaking background MC (black boxes in right plot), combinatoric background from data SB (red boxes, not to scale with the black boxes), and observed data (points). Only the default $f_A = f_V$ signal MC is shown here.

independent of the photon energy. In addition, since the signal MC only generates events with photon energies greater than 350 MeV in the $B_{\rm sig}$ rest frame, an exclusive MC sample of $B^+ \to e^+\nu_e$, where the electron emits a low-energy bremsstrahlung photon, is used to check the signal efficiency below 350 GeV. Using the same signal selection as in the $B^+ \to \ell^+\nu_\ell\gamma$ analysis (except for the bremsstrahlung recovery algorithm), the resulting efficiency increases from (0.20 ± 0.005) to (0.25 ± 0.02) as E_γ increases from 0 to 350 MeV, which is consistent with the lowest photon-energy bin in Figure 5–22.

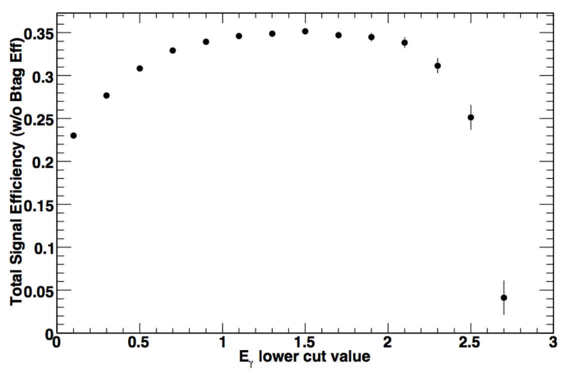

Figure 5–22: The total $B^+ \to \ell^+\nu_\ell\gamma$ signal efficiency, divided by the $B_{\rm tag}$ reconstruction efficiency, as a function of the lower bound of a photon-candidate energy requirement, in GeV. This plot is produced using the signal MC and demonstrates that the signal selection efficiency is relatively independent of the photon energy.

To remove the theoretical uncertainty associated with $E_\gamma < \Lambda_{QCD}$, some theorists suggest to measure $B^+ \to \ell^+\nu_\ell\gamma$ using only events with $E_\gamma \gtrsim 1$ GeV [45, 37]. Therefore, a second model-independent branching fraction is determined for this $B^+ \to \ell^+\nu_\ell\gamma$ analysis by requiring the photon-candidate energy to be above 1 GeV in the $B_{\rm sig}$ rest frame. Otherwise, the signal selection remains the same. The results are given in Table 5–5.

Table 5–5: The results in the photon-energy region above 1 GeV, including the expected background yields (N_i^{bkg}), signal efficiencies (ϵ_i^{sig}), number of observed data events (N_i^{obs}), and the resulting branching-fraction upper limits at 90% CL. Uncertainties are given as statistical ± systematic.

	$B^+ \to e^+\nu_e\gamma$	$B^+ \to \mu^+\nu_\mu\gamma$
ϵ_i^{sig}	$(5.5 \pm 0.2) \times 10^{-4}$	$(5.7 \pm 0.3) \times 10^{-4}$
N_i^{bkg}	1.4 ± 0.3	2.5 ± 1.0
N_i^{obs}	2	4
Limits	$< 17 \times 10^{-6}$	$< 23 \times 10^{-6}$
Combined Limits	$< 14 \times 10^{-6}$	
$\mathcal{B}_{\text{combined}}$	$(3.8^{+6.0+1.7}_{-3.5-1.6}) \times 10^{-6}$	

CHAPTER 6
$B \to K^{(*)}\nu\overline{\nu}$ Analysis Procedure

6.1 Signal Selection

6.1.1 Signal $K^{(*)}$ Reconstruction

The $B \to K^{(*)}\nu\overline{\nu}$ signal decays are reconstructed in one of the following six decay channels:

- $B^+ \to K^+\nu\overline{\nu}$
- $B^+ \to [K^+\pi^0]\nu\overline{\nu}$
- $B^+ \to [K^0_S\pi^+]\nu\overline{\nu}$
- $B^0 \to K^0_S\nu\overline{\nu}$
- $B^0 \to [K^+\pi^-]\nu\overline{\nu}$
- $B^0 \to [K^0_S\pi^0]\nu\overline{\nu}$

where the particles in brackets represent particles decaying from an on-shell K^* resonance. The K^0_S mesons are reconstructed via two charged pions, and π^0 candidates are reconstructed from two photons.

Since all six signal channels possess low track-multiplicity, as illustrated by Figure 6–1, this analysis requires that all events have either 1, 2, or 3 signal-side tracks, depending on the signal channel. This requirement alone reduces the well-reconstructed B_{tag} background by 2/3. In addition, the summed charge of all the signal-side tracks must be opposite the B_{tag} charge. The surviving events are sorted into the different signal channels, based on track multiplicity and the reconstruction of K^*, K^0_S, and π^0 candidates.

The π^0 candidates are reconstructed by combining two signal-side clusters with CM energies greater than 30 MeV, cluster lateral moments greater than 0 and less

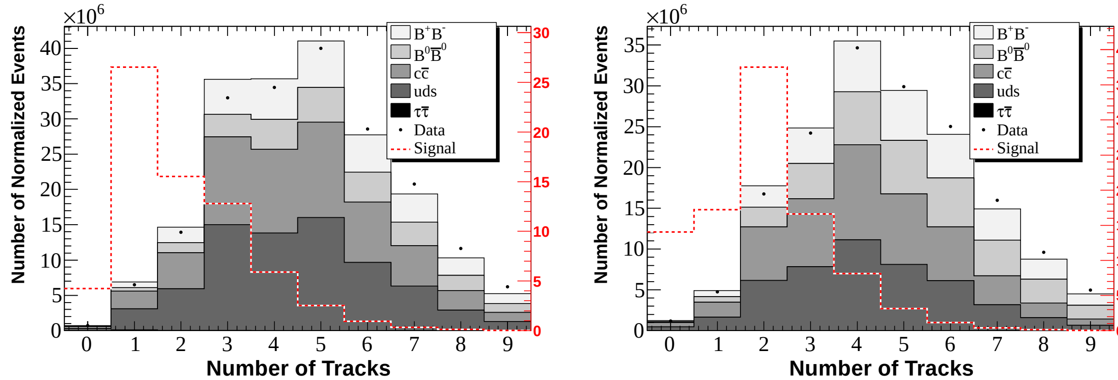

Figure 6–1: The signal-side track multiplicity, after the B_{tag} reconstruction skim, separated into (left) charged B_{sig} and (right) neutral B_{sig} candidates. These plots compare the data (points) with the generic background MC, and show the signal MC distributions (red dashed).

than 80%, and a summed CM energy greater than 200 MeV. The invariant mass of the π^0 candidates should be between 100 and 160 MeV/c^2.

The K_S^0 candidates are reconstructed by combining two signal-side tracks of opposite charge. Because K_S^0 candidates have a non-negligible lifetime and thus tend to decay outside the interaction region, a multivariate Kalman filter algorithm is used to ensure that the two tracks originate from a common vertex. This is done by determining the point-of-closest-approach (POCA) of each track to a common vertex. This algorithm corrects the four-momentum of each track to account for the hypothesis that it originates from this vertex and has the mass of a charged pion. The corrected invariant mass is required to be within 25 MeV/c^2 from the nominal K_S^0 mass for the reconstruction, although a tighter mass window of ± 7 MeV/c^2 from the nominal K_S^0 mass is used in the final selection. Furthermore, both tracks must be inconsistent with electron, muon, and kaon PID selectors. The reconstructed K_S^0 invariant mass distributions are shown in the left plot of Figure 6–2. Breit-Wigner fits to the mass peaks indicate a mean mass of 0.4976 (0.4973) GeV/c^2 for signal MC (data) and a width of 4.2 (5.5) MeV/c^2.

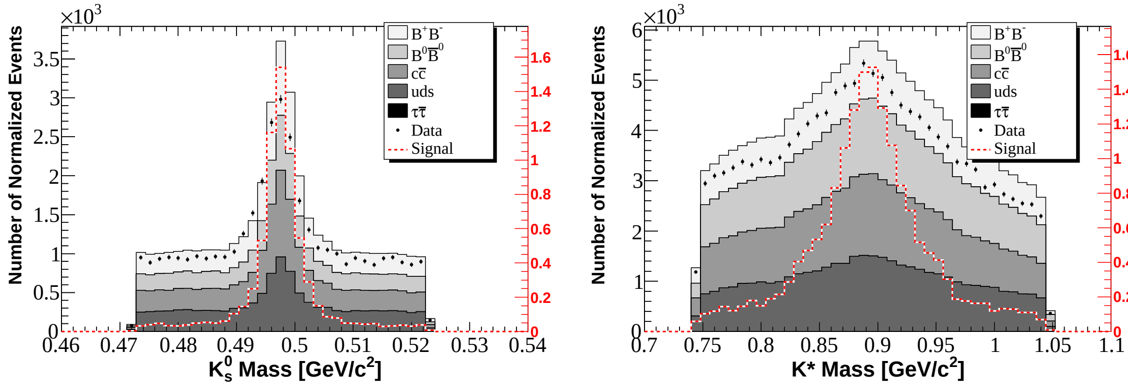

Figure 6–2: The distribution of the invariant mass of the (left) K_S^0 candidates and (right) K^* candidates, after applying loose requirements on the $B_{\rm tag}$ and on K_S^0 and K^* reconstructions. These plots compare the data (points) with the generic background MC, and show the signal MC distributions (red dashed).

A $K^* \to K^+\pi^0$ candidate is reconstructed by combining a π^0 candidate with a signal-side track that satisfies the kaon PID selector, and requires exactly one signal-side track within the event. A $K^* \to K_S^0\pi^+$ candidate is reconstructed by combining a K_S^0 candidate with a signal-side track that satisfies the pion PID selector, and requires exactly three signal-side tracks within the event. A $K^* \to K^+\pi^-$ candidate requires exactly two signal-side tracks in the event and is reconstructed by combining both tracks. Furthermore, one of the tracks is required to satisfy the kaon PID selector, while the other must be inconsistent with electron, muon, and kaon PID selectors. Finally, a $K^* \to K_S^0\pi^0$ candidate is reconstructed by combining a K_S^0 and π^0 candidate and requires exactly two tracks within the event. The pion PID selector uses an Error Correcting Output Code classifier [91] that is trained to distinguish kaons, pions, protons, and electrons, with muons explicitly vetoed within the selector. The kaon PID selector uses a Bootstrap-Aggregated ("Bagged") Decision Tree classifier, which specializes in kaon/pion discrimination. The energies of the K^+, π^+, and K_S^0 candidates are corrected to be consistent with the nominal mass of their respective particle types (listed in Table 2–3), since the momenta of tracks are measured with high resolution by the SVT and DCH. Conversely, the momentum of each π^0 candidate is corrected to be consistent with its nominal mass, since only the energy of the daughter photons is detectable, while their momenta must be inferred based on cluster position within the EMC. After these energy or momentum corrections, the invariant mass of the involved tracks, π^0, and/or K^0_S daughters is required to be within 150 MeV/c^2 from the nominal K^* mass for the reconstruction, although a tighter mass window of $\pm 70\,\mathrm{MeV}/c^2$ from the nominal K^* mass is used in the final selection. The reconstructed K^* invariant mass distributions are shown in the right plot of Figure 6–2. Breit-Wigner fits to the mass peaks indicate a mean mass of 0.892 (0.890) GeV/c^2 for signal MC (data) and a width of 0.065 (0.13) GeV/c^2.

After reconstructing the B_{tag}, π^0, K^0_S, and K^* candidates, all events are separated into one of the six signal channels such that every event is uniquely categorized. All events with three tracks are considered a $B^+ \to [K^0_S\pi^+]\nu\overline{\nu}$ event. There can be two possible K^{*+} candidates formed from three tracks, so if both combinations produce a good candidate, the K^{*+} candidate whose mass is closest to the nominal K^{*+} mass is chosen. Events with one track are required to satisfy the kaon PID selector and can be either $B^+ \to K^+\nu\overline{\nu}$ or $B^+ \to [K^+\pi^0]\nu\overline{\nu}$ events. It is considered the latter if a $K^{*+} \to K^+\pi^0$ can be reconstructed within the event, otherwise it is considered the former. Finally, a two-track event with a track that satisfies the kaon PID selector is assigned as a $B^0 \to [K^+\pi^-]\nu\overline{\nu}$ event. Otherwise, if the two-track event contains a $K^{*0} \to K^0_S\pi^0$ candidate, it is considered a $B^0 \to [K^0_S\pi^0]\nu\overline{\nu}$ event, and if not, it is identified as a $B^0 \to K^0_S\nu\overline{\nu}$ event. For $B^+ \to [K^+\pi^0]\nu\overline{\nu}$ and $B^0 \to [K^0_S\pi^0]\nu\overline{\nu}$ events, there can be several K^* candidates since there can be many π^0 candidates within an event. Studies using the particle-truth information in the signal MC indicate that the π^0 energy is the optimal variable for maximizing the number of correctly reconstructed π^0 candidates. Therefore, the chosen K^* candidate is the one reconstructed with the highest-energy π^0 candidate.

6.1.2 Additional Cluster Energy

As in the $B^+ \to \ell^+\nu_\ell\gamma$ analysis, the amount of unassigned CM energy in the event (E_{extra}) is a useful variable that is completely uncorrelated with the signal kinematics. Since, the $B \to K^{(*)}\nu\overline{\nu}$ analysis has no kinematic handles equivalent to the m_ν^2 variable of $B^+ \to \ell^+\nu_\ell\gamma$ which can be exploited for background rejection, E_{extra} is the most powerful discriminant for separating background from the signal $B \to K^{(*)}\nu\overline{\nu}$ decays. After reconstructing the $K^{(*)}$ candidates, the E_{extra} is calculated using all signal-side clusters with energy greater than 50 MeV, excluding those that are used in the reconstruction of the π^0 candidate within the relevant signal channels.

In addition, according to the particle-truth information in the $B^+ \to K^+\nu\overline{\nu}$ signal MC, about 1/4 of events have a cluster that is either a fragment cluster from the signal-kaon shower in the EMC or an immediate daughter of the signal kaon. Such clusters have a lab-frame momentum vector that is almost parallel to that of the signal kaon candidate, in both the ϕ (azimuthal) and θ (polar) angles. The variable r_{clus}, which has units in degrees, is calculated using the equation of an ellipse:

$$r_{\mathrm{clus}} = \sqrt{\Delta\theta^2 + \frac{(Q_K \cdot \Delta\phi - 8^\circ)^2}{1.5}} \tag{6.1}$$

where 8° is the approximate offset in $+\Delta\phi$ from the magnetic field, and 1.5 is the approximate ratio between the ellipse radii. Due to the magnetic field, the charge of the kaon determines the direction, in ϕ, that the kaon trajectory will bend compared to any neutral shower fragments. Therefore, $\Delta\phi$ is multiplied by the kaon-track charge ($Q_K = \pm 1$). The distribution of the r_{clus} values are shown in Figure 6–3. Any cluster in the $B^+ \to K^+\nu\overline{\nu}$ channel with $r_{\mathrm{clus}} < 15^\circ$ is recovered as a "kaon cluster" and removed from the E_{extra} calculation, which improves the $B^+ \to K^+\nu\overline{\nu}$ signal efficiency by about 13%. This requirement effectively corresponds to $|\Delta\theta| < 15^\circ$ and $-14.5^\circ < \Delta\phi < 30.5^\circ$. This algorithm is only applied in the $B^+ \to K^+\nu\overline{\nu}$ signal channel; the other five channels do not benefit significantly from such an algorithm.

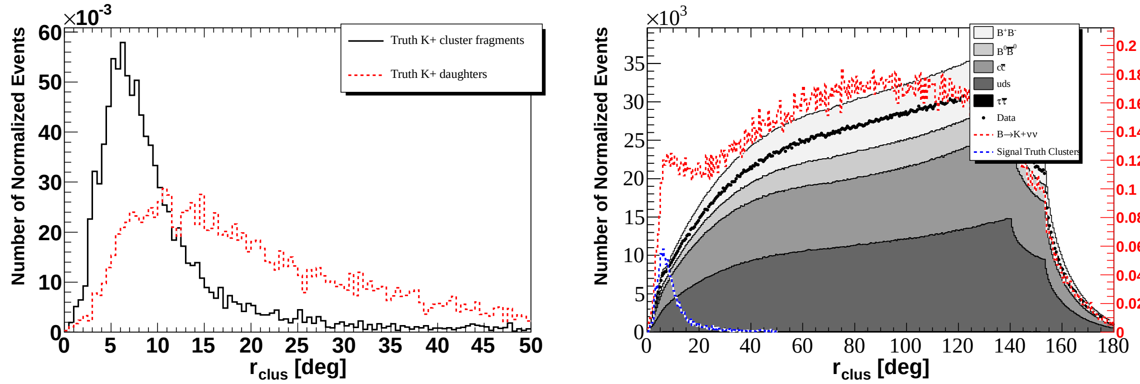

Figure 6–3: (left) The distribution of r_{clus} for $> 50\,\text{MeV}$ clusters which, according to MC particle-truth information, are from signal-kaon shower fragments (black solid) or daughters of the signal kaons (red dashed). This plot shows only events from the signal $B^+ \to K^+\nu\overline{\nu}$ MC. (right) The r_{clus} distribution for all clusters, comparing the data (points) with the generic background MC, and showing the signal $B^+ \to K^+\nu\overline{\nu}$ MC distribution (red dashed). The bumps at 140 and 153 correspond to $\phi = \pm 180$. Both of these plots are produced after applying loose requirements on the B_{tag} and on K^0_S and K^* reconstructions.

As shown in the left plot of Figure 6–4, the signal peaks at zero for E_{extra}, while the number of background events tends to rise with the energy. The discrepancy between the data and the MC is reduced when the data in the m_{ES} sidebands are used in place of the combinatoric MC, as discussed in Section 6.5. Requirements on E_{extra} are optimized separately for each signal channel, ranging from 110 to 330 MeV, as outlined in Table 6–1. In addition, a loose requirement of less than 13 signal-side clusters is applied in order to improve agreement between data and MC. The number of signal-side clusters is shown in the right plot of Figure 6–4. The data events with $E_{\text{extra}} < 400\,\text{MeV}$ were kept blinded until the end of the analysis.

Table 6–1: The upper-value of the allowed E_{extra} signal region in each $B \to K^{(*)}\nu\overline{\nu}$ signal channel.

Channel	E_{extra} (GeV)
$K^{+}\nu\overline{\nu}$	0.11
$[K^{+}\pi^{0}]\nu\overline{\nu}$	0.18
$[K^{0}_{S}\pi^{+}]\nu\overline{\nu}$	0.29
$K^{0}_{S}\nu\overline{\nu}$	0.33
$[K^{+}\pi^{-}]\nu\overline{\nu}$	0.31
$[K^{0}_{S}\pi^{0}]\nu\overline{\nu}$	0.28

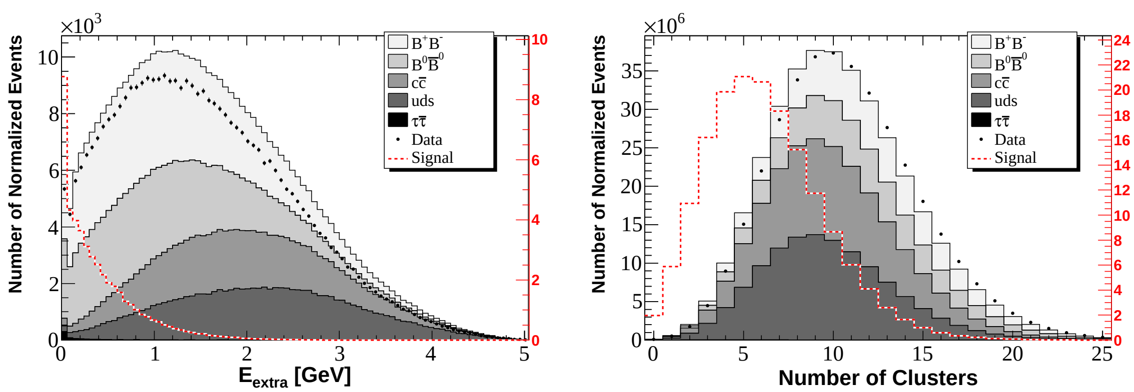

Figure 6–4: (left) The distribution of E_{extra} after applying loose requirements on the B_{tag} and on K^{0}_{S} and K^{*} reconstructions. (right) The signal-side cluster multiplicity after the B_{tag} skim reconstruction. These plots compare the data (points) with the generic background MC, and show the signal MC distributions (red dashed).

6.1.3 Missing Energy

The missing four-momentum within the event is calculated by subtracting the four-momenta of all signal-side tracks and clusters from the reconstructed B_{sig} four-momenta (where $E_{B_{\text{sig}}} = E_{\text{CM}}/2$ and $\vec{p}_{B_{\text{sig}}} = -\vec{p}_{B_{\text{tag}}}$). Because the B_{tag} is reconstructed using fully hadronic modes, any missing energy or momentum can be assumed to originate from the B_{sig}. Therefore, since signal events have two neutrinos, the amount of missing energy in the event is required to be greater than zero. However, no additional restrictions on the amount of missing energy are applied, since this value is highly correlated with the kaon momentum.

In addition, the angle of the missing momentum might be considered useful, since it should be back-to-back with the kaon momentum in the B_{sig} rest frame for signal events. However, because all the signal-side clusters are used in calculating the missing momentum, it is highly correlated with the E_{extra} variable and thus avoided. Events where the direction of the missing momentum is outside of the detector's angular acceptance, however, are suppressed using the six-variable Continuum Likelihood, as discussed in Section 4.3.

6.2 $B \to K^{(*)}\nu\overline{\nu}$ Signal Kinematics

6.2.1 Kinematic Modeling

Since the signal MC is generated using a simple phase-space model of the kinematics, it is reweighted to match the kinematic distribution predicted by a SM-based theoretical model in order to obtain more realistic efficiencies for SM $B \to K^{(*)}\nu\overline{\nu}$ decays. The kinematics of an event can be described by the unitless $s_B \equiv q^2/(m_B c)^2$ variable, where q^2 is an invariant quantity describing the four-momentum transfer from the B meson to the neutrinos. The value of s_B ranges between zero and the kinematic endpoint $(1-m_{K^{(*)}}/m_B)^2$ (≈ 0.82 and ≈ 0.69 for $B \to K\nu\overline{\nu}$ and $B \to K^*\nu\overline{\nu}$ respectively), and its predicted SM distribution is shown in the top plots of Figure 6–5. Since $K^{(*)}$ can decay into several daughters while the neutrinos do not, the "true-s_B"

value of each event is calculated as the invariant mass of the two neutrinos, determined using the generator-truth information in the MC. To obtain the correct signal efficiency, including the B_{tag} reconstruction efficiency, unskimmed signal MC samples are produced without the B_{tag} reconstruction or the `BSemiExclAdd` skim. In order to reproduce the theoretical distribution of s_B, "s_B-reweight" values are determined from the unskimmed signal phase-space distribution. Each event in the skimmed signal MC is then multiplied by the s_B-reweight value that corresponds to its true-s_B value. The s_B-reweight values are determined separately for each of the six signal MC samples. The s_B distribution for $B^+ \to K^+\nu\overline{\nu}$, before and after s_B-reweighting, is shown in the bottom plot of Figure 6–5.

In addition to the s_B distribution, the helicity model used in the $B \to K^*\nu\overline{\nu}$ signal MC also needs correcting. The variable $\cos\theta_K$ employs the helicity angle θ_K, defined as the angle between the B_{sig} flight direction and the K^+ or K^0_S flight direction, both in the K^* rest frame. The $\cos\theta_K$ value is calculated for each event using the generator-truth information. The resulting $\cos\theta_K$ distribution is fit to the equation:

$$\frac{3}{2}F_L \cos^2\theta_K + \frac{3}{4}(1 - F_L)(1 - \cos^2\theta_K) \tag{6.2}$$

to extract the K^* longitudinal polarization fraction F_L [92]. This is done bin-by-bin in s_B to get a F_L distribution versus s_B. The signal MC samples are generated using a flat F_L distribution at 1/3, as shown in the bottom left plot of Figure 6–6, which corresponds to no preferential decay direction. However, according to the SM theory predictions, shown in the top plot of Figure 6–6, F_L should be closer to one at low s_B values and should taper to 1/3 as s_B increases. The value of $F_L = 1$, which occurs when the neutrinos are at the limit of zero energy, is due to helicity conservation, which forces the B meson to decay into a longitudinal K^* [47]. "Helicity-reweight" values are determined in each of the unskimmed $B \to K^*\nu\overline{\nu}$ signal MC samples, using both the true-s_B and true $\cos\theta_K$ values in the event. The effect on $\cos\theta_K$ from this

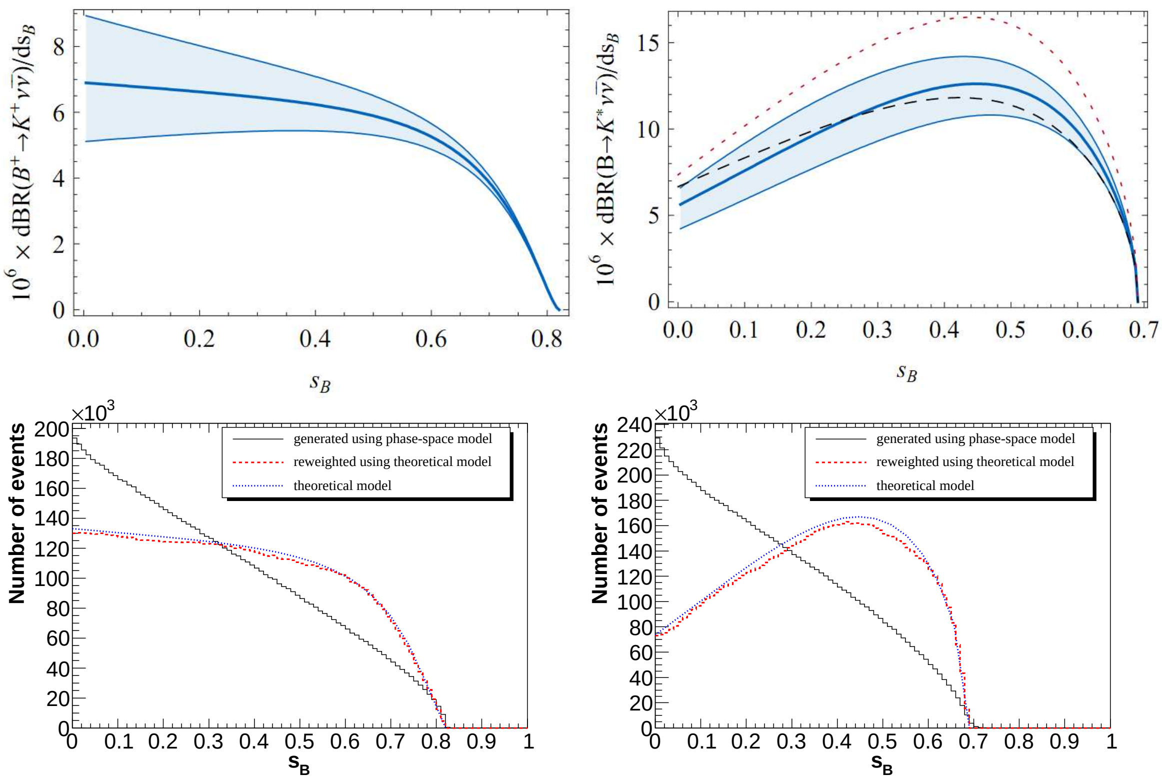

Figure 6–5: The theoretical SM distribution of s_B for (top left) $B \to K\nu\overline{\nu}$ and (top right) $B \to K^*\nu\overline{\nu}$ [47]. The blue-shaded area represents the SM theoretical uncertainty and the black-dashed and red-dotted lines illustrate two other form-factor models as discussed in Ref. [47]. The distribution of s_B within the (bottom left) $B^+ \to K^+\nu\overline{\nu}$ and (bottom right) $B^+ \to K^{*+}\nu\overline{\nu}$ unskimmed signal MC before s_B-reweighting (black solid) and after sB-reweighting (red dashed).

helicity-reweighting can be seen in the bottom right plot of Figure 6–6, which shows only events with $s_B < 0.01$.

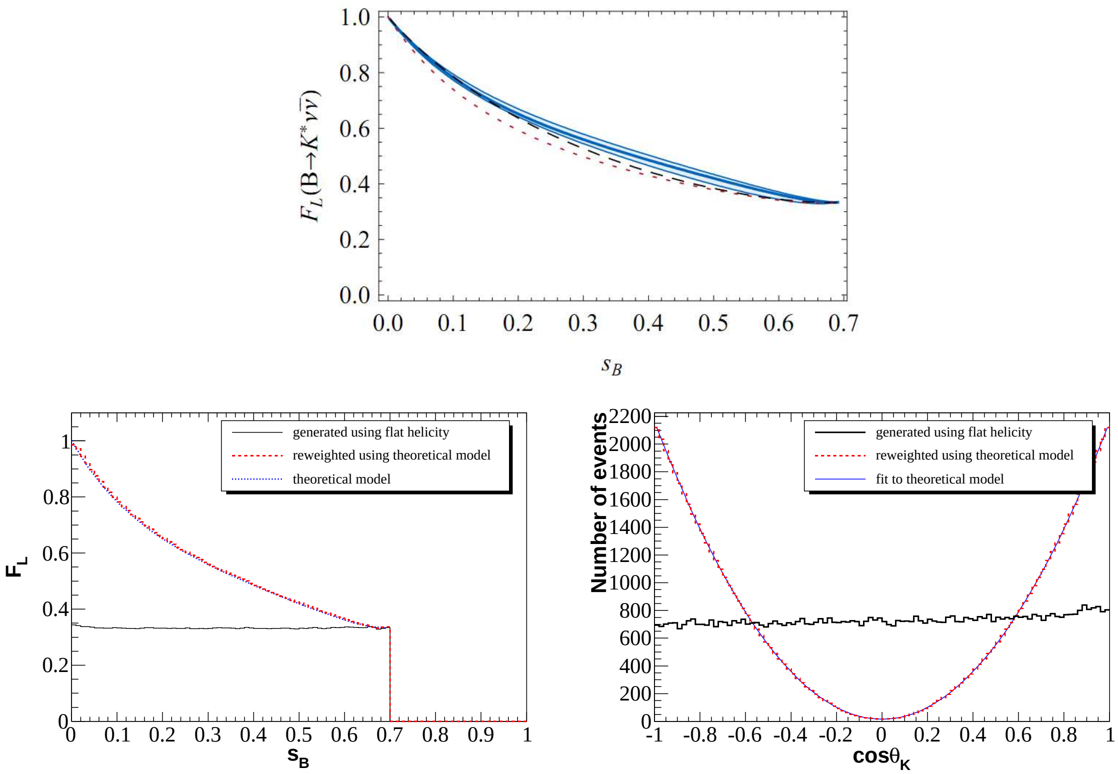

Figure 6–6: (top) The theoretical F_L distribution for SM $B \to K^*\nu\overline{\nu}$, as given by Ref. [47]. (bottom left) The distribution of F_L, and (bottom right) the distribution of $\cos\theta_K$ for events with $s_B < 0.01$. Both bottom plots compare the $B^+ \to K^{*+}\nu\overline{\nu}$ unskimmed signal MC before helicity-reweighting (black solid) and after helicity-reweighting (red dashed).

6.2.2 Kinematic Selection

Because $B \to K^{(*)}\nu\overline{\nu}$ events are three-body decays, with the B meson decaying into a kaon[1] and two massless neutrinos, the kaon tends to be higher in momentum than kaons from other B meson events, the majority of which come from the decay

[1]Within this section, "kaon" refers to the K^*, K^0_S, or K^+ meson which decays directly from the B_{sig}.

of a D meson in $B \to D^{(*)}X$ events. The s_B value of the event is indirectly correlated with the momentum of the kaon, as shown in Figure 6–7. Therefore, both the kaon momentum and the s_B value are valuable discriminators between signal and background. The s_B variable is preferable over the kaon momentum because it is an invariant quantity and is the more commonly used variable in theoretical papers discussing $B \to K^{(*)}\nu\overline{\nu}$. Unlike the true-$s_B$ values derived from the generator-truth information of the neutrinos for s_B- and helicity-reweighting, the "observed"-s_B variable must be determined from observables in the detector. Since one cannot detect the neutrinos, the observed s_B is calculated as:

$$s_B = \frac{(p_{B_{\mathrm{sig}}} - p_K)^2}{(m_B c)^2} \tag{6.3}$$

where m_B is the nominal mass of the B meson, $p_{B_{\mathrm{sig}}}$ is the four-momentum of the B_{sig} as determined by reconstructing the B_{tag}, and p_K is the four-momentum of the kaon candidate. The energy of these kaon candidates are corrected to correspond to the nominal kaon mass. Therefore, the recovered "kaon clusters" (discussed in Section 6.1.2) have no effect on this variable.

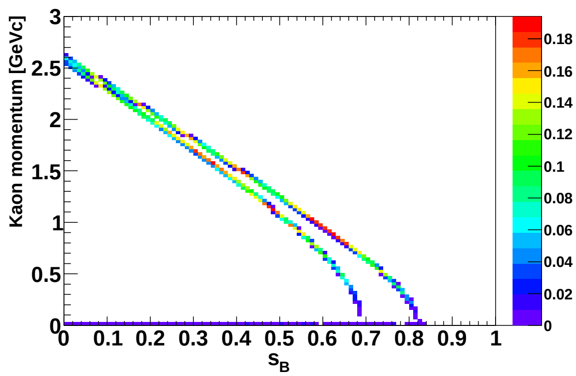

Figure 6–7: The two-dimensional distribution of kaon momentum versus s_B values, for signal MC only, which demonstrates the correlation between the two variables. The top "line" corresponds to $B^+ \to K^+\nu\overline{\nu}$ and $B^0 \to K^0_S\nu\overline{\nu}$, while the bottom "line" corresponds to the four K^* channels. This plot was produced after applying loose requirements on the B_{tag}, on K^0_S and K^* reconstructions, and on PID.

Figure 6–8 shows the distribution of the s_B values. Because the low-s_B region has little background and thus provides the most sensitivity to $B \to K^{(*)}\nu\overline{\nu}$, the SM branching fraction is found in this analysis by restricting the signal selection to the low-s_B region. Events are required to have $s_B < 0.3$, which corresponds to a kaon momentum greater than about 1.8 (1.7) GeV/c for $B \to K\nu\overline{\nu}$ ($B \to K^*\nu\overline{\nu}$) events. Although this removes about 54 (62)% of signal $B \to K\nu\overline{\nu}$ ($B \to K^*\nu\overline{\nu}$) events, it also removes over 90% of the background. Although such a requirement is ideal to maximize SM sensitivity, there are New Physics possibilities that would be noticeable in the higher s_B region, as discussed in Section 2.4. Therefore, this analysis also measures partial branching fractions over the full s_B distribution by removing this s_B restriction. This is discussed in more detail in Section 6.8.1

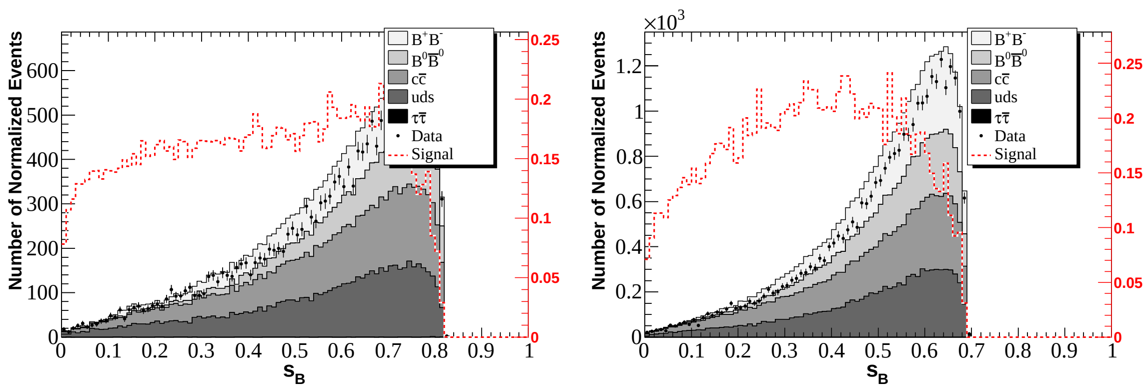

Figure 6–8: The distribution of s_B for (left) $B^+ \to K^+\nu\overline{\nu}$ and $B^0 \to K^0_S\nu\overline{\nu}$, and (right) the four K^* channels. These plots compare the data (points) with the generic background MC, and show the signal MC distributions (red dashed), after applying loose requirements on the B_{tag}, on K^0_S and K^* reconstructions, and on PID. The signal MC distribution is affected by the signal cross-feed between channels.

The helicity angle θ_K would be a valuable observable to measure, in order to confirm or exclude various theoretical predictions of the K^* polarization F_L. However, in order to extract F_L, one must have enough statistics to fit the $\cos\theta_K$ distribution in the data to Equation (6.2). However, with the current experimental sensitivity, insufficient signal events are present in the data to satisfactorily provide a fit for such a measurement.

6.3 Peaking Background Estimation

Unlike the $B^+ \to \ell^+\nu_\ell\gamma$ analysis, which has powerful kinematic and topological handles to reduce the background, the two neutrinos in the final state of $B \to K^{(*)}\nu\overline{\nu}$ prevent the use of such handles. Instead, this $B \to K^{(*)}\nu\overline{\nu}$ analysis relies mainly on the kaon identification, the E_{extra} variable, and the low-s_B restrictions. However, any event with a reconstructed kaon and little additional detected energy could potentially pass the signal selection. The primary background events that pass the signal selection are from $B \to D^{(*)}\ell\nu$ events, where the D meson decays via a kaon. However, there is also a large variety of other $B\overline{B}$ backgrounds, with well-reconstructed B_{tag} candidates, which tend to peak within the signal region of the B_{tag} m_{ES} distribution. Therefore, the number of events in the peaking background (N_i^{peak}) is estimated primarily from the $B\overline{B}$ generic MC. The branching fractions of the dominant decay modes are corrected to agree with the most up-to-date experimental averages, as outlined in Table 6–2.

Table 6–2: The branching fractions for the dominant background mode events, including the values used in generating the generic MC ($\mathcal{B}_{\text{genMC}}$) and the correct up-to-date measurement values used to weight the background MC samples ($\mathcal{B}_{\text{meas}}$) [2]. The table is split into "B^+" and "B^0" channels where, for example, the B^+ channel for $B \to De\nu$ is $B^+ \to D^0e^+\nu$ and the B^0 channel is $B^0 \to D^-e^+\nu$. All branching fractions are given as ($\times 10^{-3}$).

Decay	$\mathcal{B}_{\text{genMC}}(B^+)$	$\mathcal{B}_{\text{meas}}(B^+)$	$\mathcal{B}_{\text{genMC}}(B^0)$	$\mathcal{B}_{\text{pdg}}(B^0)$
$B \to D\ell\nu$	22.4	(22.3 ± 1.1)	20.7	(21.7 ± 1.2)
$B \to D^*\ell\nu$	61.7	(56.8 ± 1.9)	57.0	(51.1 ± 2.3)
$B \to D\tau\nu$	7.0	(7.7 ± 2.5)	7.0	(15 ± 5)
$B \to D^*\tau\nu$	16.0	$(21 \pm 4\ \ )$	6.0	(11 ± 4)
$B \to D\pi^+$	5.0	(4.84 ± 0.15)	2.8	(2.68 ± 0.13)
$B \to DK^+$	0.41	(0.368 ± 0.033)	0.20	(0.2 ± 0.06)
$B \to D^*K^+$	0.36	(0.421 ± 0.035)	0.17	(0.214 ± 0.016)
$B \to DK^{*+}$	0.61	(0.53 ± 0.04)	0.37	(0.45 ± 0.07)
$B \to D^*K^{*+}$	0.77	(0.81 ± 0.14)	0.38	(0.33 ± 0.06)
$B^+ \to \tau^+\nu_\tau$	0.093	(0.165 ± 0.034)	—	—

One potential background is from $B^+ \to \tau^+\nu_\tau$, where $\tau^+ \to K^{(*)+}\overline{\nu}_\tau$, since the final decay products are exactly the same as in the $K^{(*)+}\nu\overline{\nu}$ signal decays, neglecting neutrino flavour. Such events tend to have lower-momentum kaons than in signal decays and are thus suppressed by the low-s_B restriction. Even so, the product branching fraction $\mathcal{B}(B^+ \to \tau\nu_\tau)\cdot\mathcal{B}(\tau \to K^{(*)+}\overline{\nu}_\tau) = 3.2\times10^{-6}$ [2] is at the same order as the SM prediction of the signal mode. Therefore, it is important to have a good estimate and understanding of this background, especially as some theorists claim that this may be an underestimated background in previous experimental $B^+ \to K^+\nu\overline{\nu}$ results [48]. To increase the statistics of the $B^+ \to \tau^+\nu_\tau, \tau^+ \to K^{(*)+}\overline{\nu}_\tau$ background estimate, an exclusive MC sample is used in which one B meson decays via $\tau^+\nu_\tau$ while the other decays generically. The τ also decays generically. The $\tau^+ \to K^{(*)+}\overline{\nu}_\tau$ branching fractions in the MC are consistent with current experimental averages [2]. For the estimate of N_i^{peak}, the exclusive $B^+ \to \tau^+\nu_\tau$ MC is used to estimate this background. Therefore, all instances of $B^+ \to \tau^+\nu_\tau$ events are removed from the generic B^+B^- MC in order to avoid double-counting, and are replaced with the higher statistics from the exclusive $B^+ \to \tau^+\nu_\tau$ MC. The number of expected $B^+ \to \tau^+\nu_\tau$ events, as well as other types of background events, according to the MC samples, are given in Table 6–3.

In addition, the decays $B \to \pi\tau^+\nu_\tau$, $\tau^+ \to K^+\overline{\nu}_\tau$ are also considered, since their final decay products are the same as $B^+ \to [K^+\pi^0]\nu\overline{\nu}$ and $B^0 \to [K^+\pi^-]\nu\overline{\nu}$ signal decays. However, these decays have product branching fractions of order 10^{-7}, which are at least an order of magnitude lower than the corresponding signal channels. In addition, because the K^+ and pion are not formed through a K^* resonance, these semileptonic decays are less likely to pass the K^* mass requirements within the signal selection.

Finally, two-body decays such as $B \to D^{(*)}K^{(*)}$ are also problematic as they tend to contain high momentum kaons, and thus fall in the low s_B region where the signal

Table 6–3: The expected number of background decay modes in the different signal channels, determined directly from the generic background MC and exclusive $B^+ \to \tau^+\nu_\tau$ MC after the full signal selection and the branching fraction corrections. The uncertainties are only statistical.

Mode	$B^+ \to K^+\nu\overline{\nu}$	$B^0 \to K^0\nu\overline{\nu}$	$B^+ \to K^{*+}\nu\overline{\nu}$	$B^0 \to K^{*0}\nu\overline{\nu}$
$B \to \tau^+\nu_\tau$	0.42 ± 0.07	0	0.21 ± 0.05	0.01 ± 0.01
$B \to D^{(*)}e^+\nu_e$	0.39 ± 0.19	0.49 ± 0.22	0.58 ± 0.23	1.33 ± 0.37
$B \to D^{(*)}\mu^+\nu_\mu$	0.89 ± 0.30	0.52 ± 0.23	1.15 ± 0.33	1.30 ± 0.35
$B \to D^{(*)}\pi^+$	0.10 ± 0.10	0.09 ± 0.09	0.10 ± 0.10	0.39 ± 0.19
$B \to D^{(*)}a_1^+$	0	0.19 ± 0.14	0.10 ± 0.10	0.39 ± 0.19
$B \to D^{(*)}\rho^+$	0	0.30 ± 0.17	0	0.40 ± 0.20
$B \to K^{(*)}\gamma$	0	0	0.10 ± 0.10	0.19 ± 0.14
$B \to K^0K^0K^{(*)}$	0	0.10 ± 0.10	0.31 ± 0.18	0.30 ± 0.17
$B \to D^{(*)}K^{(*)+}$	0.09 ± 0.09	0	0	0
$B \to J/\psi K^{(*)}$	0	0	0	0.10 ± 0.10
$B \to \pi\tau^+\nu_\tau$	0	0	0	0.10 ± 0.10
Other $B\overline{B}$	0.10 ± 0.10	0.49 ± 0.22	0.50 ± 0.22	1.81 ± 0.42
$c\overline{c}$	0.10 ± 0.10	0.30 ± 0.17	0.20 ± 0.14	0.70 ± 0.26
$u\overline{u}, d\overline{d}, s\overline{s}$	0.26 ± 0.26	0	0.26 ± 0.26	0
$\tau^+\tau^-$	0.26 ± 0.26	0	0	0

should lie. For example, $B \to D^{(*)}K^+$ events decay to monochromatic kaons with momenta of 2.28 (2.23) GeV/c and a corresponding s_B value of 0.125 (0.143). The large peak in the s_B signal region is clear in Figure 6–9, which shows the $B^+ \to D^{(*)0}K^{(*)}$ background contribution in the E_{extra} sideband of $E_{\text{extra}} > 0.4\,\text{GeV}$. However, in the low E_{extra} signal region, few of these events are expected, since all of the detectable daughters of the $D^{(*)0}$ would have to produce a total energy of less than a few hundred MeV in order to pass the full signal selection. The $B \to D^{(*)}K^{(*)}$ background contribution within N_i^{peak} is estimated from the generic MC.

6.4 $B \to K^{(*)}\nu\overline{\nu}$ Selection Optimization

As in the $B^+ \to \ell^+\nu_\ell\gamma$ analysis, the $B \to K^{(*)}\nu\overline{\nu}$ analysis also uses the Punzi figure of merit in order to optimize the signal selection values, as well as to decide which variables should be included in the selection process. The figure of merit is maximized using an iterative algorithm. The optimization uses the generic background

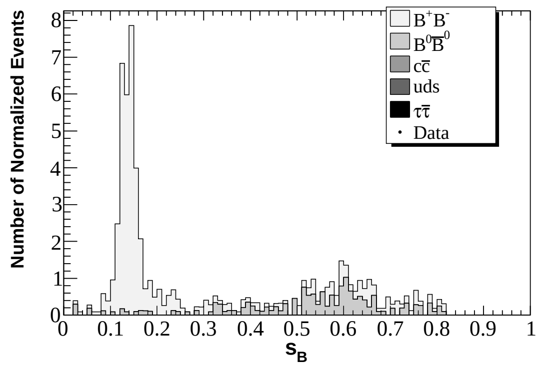

Figure 6–9: The distribution of s_B for $B \to D^{(*)0}K^{(*)}$ events, within the E_{extra} sideband of $E_{\text{extra}} > 0.4\,\text{GeV}$, after all other signal selection requirements are applied. The plot only shows $B \to D^{(*)0}K^{(*)}$ within the generic MC in order to demonstrate the tendency of the decay to peak at low-s_B values.

MC to determine $N^{\text{MC}}_{\text{bkg}}$ of Equation (3.2). In order to avoid statistical fluctuations that may cause localized maxima, the background and signal MC samples provide enough statistics to split into four equal parts for use in the optimization algorithm. In addition, systematic uncertainties are also considered, such as maintaining mass windows that avoid cutting significantly into the mass peaks, even if the optimization indicates otherwise. All six signal channels are optimized together for the B_{tag} selection criteria (m_{ES}, continuum likelihood, and low-multiplicity purity), as well as the tight K^0_S and K^* mass windows, the PID selectors, and the s_B requirement. The E_{extra} thresholds are optimized separately for each signal channel.

6.5 Combinatoric Background Estimation

The expected background for each signal channel (N_i^{bkg}) consists of events that peak within the B_{tag} m_{ES} signal region (N_i^{peak}) and non-peaking combinatoric events (N_i^{comb}). The generic $B\overline{B}$ MC is used to determine N_i^{peak}, while N_i^{comb} is determined directly from the m_{ES} sideband (SB) data in much the same way as in the $B^+ \to \ell^+\nu_\ell\gamma$ analysis. As discussed in Section 5.5, N_i^{comb} is normalized using the Combinatoric Ratio (R_{comb} in Equation (5.6)), and N_i^{peak} and ϵ_i^{sig} are normalized with the B_{tag} Yield Correction (C_{yield} in Equation (5.9)). To avoid double-counting the combinatoric component in the generic $B\overline{B}$ MC, N_i^{peak} is determined using the mis-charged $B\overline{B}$ shape and the generic MC. For the three "charged" $B^+ \to K^{(*)+}\nu\overline{\nu}$ channels, the mis-charged $B^0\overline{B}^0$ shape is employed:

$$N_i^{\text{peak}} \equiv (N_{B^+B^-}^{SR} - N_{B^+B^-}^{SB} \times R_{B^0\overline{B}^0}) \times C_{\text{yield}} \tag{6.4}$$

For the three "neutral" $B^0 \to K^{(*)0}\nu\overline{\nu}$ signal channels, all instances of $R_{B^0\overline{B}^0}$ in Equations (5.6), (5.9), and (6.4) are replaced with:

$$R_{B^+B^-} \equiv \frac{N_{B^+B^-}^{SR}}{N_{B^+B^-}^{SB}} \tag{6.5}$$

Similar to $R_{B^0\overline{B}^0}$, $R_{B^+B^-}$ quantifies the shape of the mis-charged[2] B^+B^- distribution, since the combinatoric component in the $B^0\overline{B}^0$ MC is assumed to have the same shape as that of the mis-charged B^+B^- MC.

Two sets of the R_{comb} and C_{yield} ratios are determined, one for the charged $B^+ \to K^{(*)+}\nu\overline{\nu}$ channels and one for the neutral $B^0 \to K^{(*)0}\nu\overline{\nu}$ channels. Certainly, the C_{yield} correction must be determined using enough statistics that the signal contribution is negligible compared to the background contribution; otherwise, the normalization would artificially produce a signal yield of zero by forcing the background estimate to equal the data yield. Therefore, all three ratios are determined without any requirement on E_{extra} or s_B, and with the loose K_S^0 and K^* mass windows. By normalizing the generic MC to the data using a C_{yield} that is found after applying most of the signal-side reconstruction, many of the systematics involved with the reconstruction are incorporated into this Yield Correction, which also ultimately improves the overall agreement between the data and the MC. The comparison of the

[2]For consistency with $B^+ \to \ell^+\nu_\ell\gamma$, the term "mis-charged" refers to when the absolute value of the B_{tag} candidate charge is incorrectly reconstructed. Thus, $B^\pm$ mesons that are reconstructed as $B_{\text{tag}}^\mp$ candidates do not fall into this category.

peaking yields in the data and the generic MC are shown in Figure 6–10. Charged events use an $R_{\mathrm{B^0\overline{B}^0}}$ value of 15.2%, R_{comb} of 12.5%, and a C_{yield} value of 102.6%; neutral events use $R_{\mathrm{B^+B^-}}$ = 16.4%, R_{comb} =13.1%, and C_{yield} =101.8%.

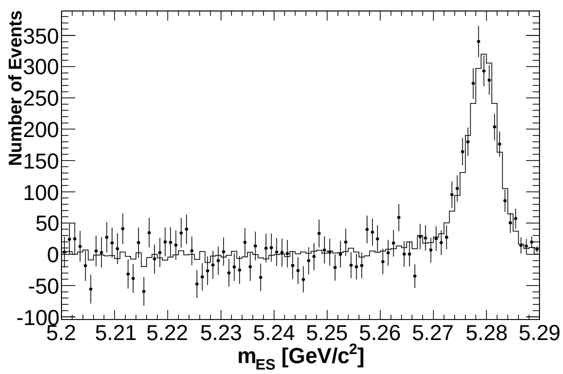

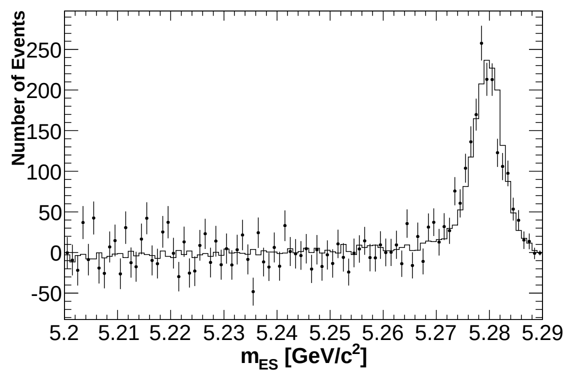

Figure 6–10: The m_{ES} peaking yields of the (left) charged and (right) neutral B_{tag} candidates, within the generic MC (solid) and the data (points). The peaking yields are used to determine the B_{tag} Yield Correction (C_{yield}) in order to normalize the MC to the data. They are produced by subtracting out the estimated combinatoric components within the data and MC (discussed in Section 5.5).

6.6 $B \to K^{(*)}\nu\overline{\nu}$ Systematic Studies

Any discrepancies in the $B \to K^{(*)}\nu\overline{\nu}$ analysis between the MC and data must be accounted for by determining systematic uncertainties. The uncertainty on the B_{tag} Yield Correction contributes to the systematic uncertainty associated with both $\epsilon_i^{\mathrm{sig}}$ and N_i^{peak}, as well as from the signal selection criteria that are applied after determining C_{yield}. Branching fraction uncertainties of background decay modes also contribute to the uncertainty in N_i^{peak}. These uncertainties are added in quadrature with the statistical uncertainty. In addition, the systematic uncertainty on the Combinatoric Ratio is evaluated and added in quadrature to the SB data statistical uncertainty.

6.6.1 Background Estimate Uncertainties

The systematic uncertainty on C_{yield} and R_{comb} are correlated with each other, since both variables use the same mis-charged $B\overline{B}$ shape. For example, if a larger

$R_{B^0\overline{B}^0}$ ratio is assumed, more of the peaking background will be subtracted out of the B^+B^- MC, but also more sideband data would be added in, thereby partly canceling the effect. To determine the systematic uncertainty associated with the total number of background events, the continuum shape ($R_{f\overline{f}}$) is used in place of the mis-charged $B\overline{B}$ shape, to model the combinatoric $B\overline{B}$ distribution. The final number of estimated background events are then compared between the two shape assumptions, with the relative difference taken as the systematic uncertainty. This uncertainty is applied to both N_i^{peak} and N_i^{comb}, and is found to be 2.6 (5.8)% for charged (neutral) channels. Since the signal efficiency is only affected by the uncertainty on C_{yield}, a separate systematic uncertainty of 8.9 (9.1)%, for the charged (neutral) signal channels, is found by comparing the relative difference in the final signal efficiencies.

In addition, since the MC is relied on to determine the peaking component of the background, the assumed branching fractions within the MC can produce discrepancies with the data. Although the branching fractions are corrected in the MC to match the current world averages, there are uncertainties on these averages that must be addressed. Therefore, the branching fractions of all the dominant background modes listed in Table 6–2 are varied by their uncertainties, either upwards or downwards simultaneously. This is an overestimate of the uncertainty, since this assumes 100% correlation between the branching fractions, so the difference in the final background estimate between the two extremes is divided by $\sqrt{12}$ [88]. This results in a systematic uncertainty of 2.8%, which is applied to N_i^{peak}.

6.6.2 Control Sample and E_{extra} Uncertainty

To verify the signal efficiency and agreement between data and MC, this analysis uses a control sample of $B^+ \to D^0\ell\nu$, with $D^0 \to K^-\pi^+$, in place of the $B^0 \to [K^+\pi^-]\nu\overline{\nu}$ signal channel. Two additional control samples are also investigated, $B^0 \to D^-\ell\nu$ with $D^- \to K^+\pi^-\pi^-$ and $B^0 \to D^-\ell\nu$ with $D^- \to K_S^0\pi^-$. These clean semileptonic samples have well-measured branching fractions that are orders of magnitude larger than $B \to K^{(*)}\nu\overline{\nu}$, thus providing reliable, high-statistical comparisons between the data and the MC. These decays are also the dominant background in the $B \to K^{(*)}\nu\overline{\nu}$ analysis, indicating that the control samples are similar enough to the signal channels that they can mimic the signature and characteristics of $B \to K^{(*)}\nu\overline{\nu}$ decays. Thus, if the MC is poorly modeling one of the signal selection variables, a discrepancy between data and the MC is expected to appear within the control samples as well. The control samples also enable the validation of the background-estimation algorithm, or the *SB-data substitution*, in which the sideband data is used in place of the combinatoric background, and the peaking yield is normalized with the C_{yield} correction, as discussed in Section 5.5.

The $D^0\ell\nu$ ($D^-\ell\nu$) candidates are reconstructed by requiring three (four) tracks, one of which must pass either a muon or electron PID selector. This leptonic track is removed from the list of signal-side tracks, and the full analysis is then performed exactly as in the $B \to K^{(*)}\nu\overline{\nu}$ selection. The only difference is that instead of requiring the invariant mass of the remaining tracks to be within the K^* mass window, they must instead be consistent with a D meson, specifically within $\pm 35\,\text{MeV}/c^2$ of the D^0 or D^- nominal masses. In addition, the SB-data substitution is performed using the same $R_{\mathrm{B^0\overline{B}^0}}$, $R_{\mathrm{B^+B^-}}$, and R_{comb} values that are used in the signal selection. However, the B_{tag} reconstruction is expected to be significantly different for $B \to D\ell\nu$ events than for $B \to K^{(*)}\nu\overline{\nu}$ events, since the D mesons from the B_{tag} and B_{sig} (or their daughters) are more likely to be swapped than in signal events. Therefore, the B_{tag} Yield Correction values are re-evaluated for the control samples using the same procedure, assumptions, and signal selection criteria as in the $B \to K^{(*)}\nu\overline{\nu}$ analyses. The C_{yield} values are found to be 90 (84)% for the $B^+ \to D^0\ell\nu$ ($B^0 \to D^-\ell\nu$) modes.

The invariant mass distribution of the non-lepton tracks, provided in Figure 6–11, show some disagreement between the data and the MC. However, the blue-dashed lines in Figure 6–11 also demonstrate that the agreement is significantly improved after the SB-data substitution. In fact, after the full signal selection, the data yield within the D-mass peak agrees with the $N_i^{\rm bkg}$ yield using SB data substitution within the statistical uncertainty of the data. This is true in all three control samples, both with and without a restriction on s_B.

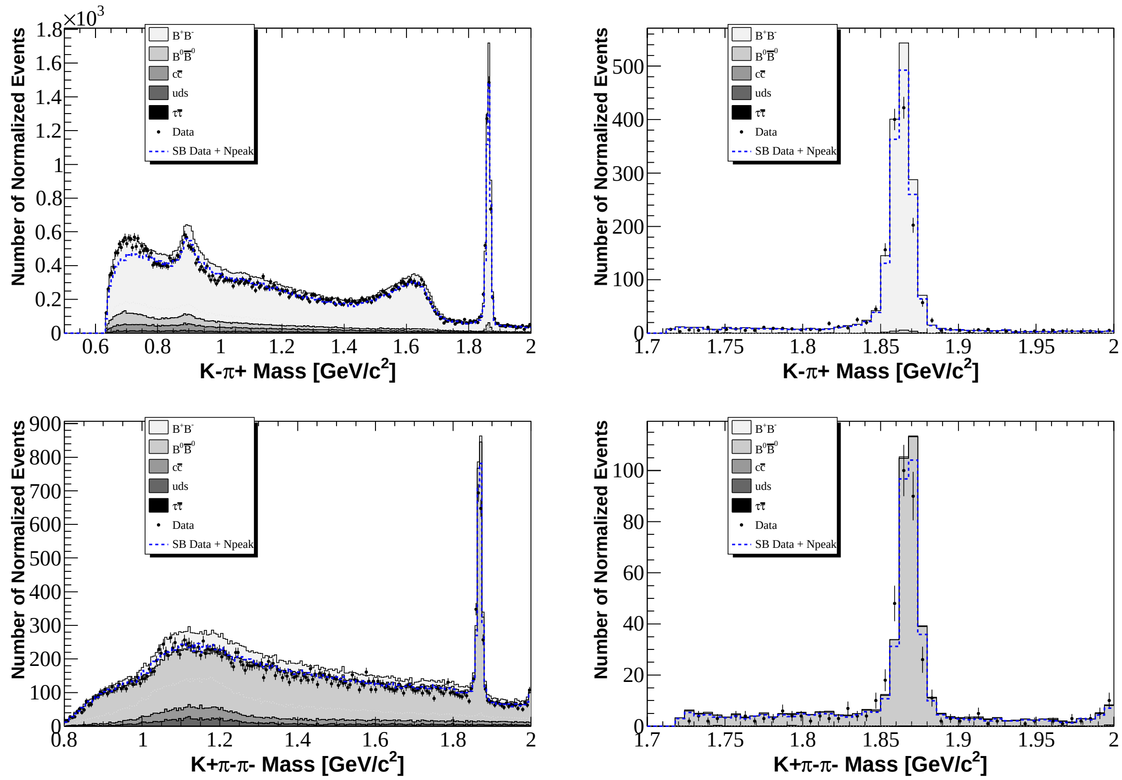

Figure 6–11: The invariant mass distribution within the (top) $B^+ \to [K^-\pi^+]\ell\nu$ and (bottom) $B^0 \to [K^+\pi^-\pi^-]\ell\nu$ control samples, produced (left) after loose $B_{\rm tag}$ requirements, and (right) after the full selection except the s_B and tight D-mass requirement. The blue-dashed lines plot the SB-data substituted $N_i^{\rm bkg} = (N_i^{\rm comb} + N_i^{\rm peak})$, which demonstrates the improved agreement with data (points) when compared with the stacked MC samples (shaded).

The $B \to D\ell\nu_\ell$ control samples are ideal for quantifying how accurately the MC models the $E_{\rm extra}$ variable, since after the $B_{\rm tag}$ candidate is identified and the semileptonic $B_{\rm sig}$ is reconstructed using only tracks, there should be no detected energy remaining in the event. The $E_{\rm extra}$ distribution of the $B^+ \to D^0\ell\nu, D^0 \to K^-\pi^+$

and $B^0 \to D^- \ell \nu, D^- \to K^+ \pi^- \pi^-$ control samples are shown in Figure 6–12, with the s_B and E_{extra} selection requirements removed. After applying the SB-data substitution, these two control samples are used to determine the E_{extra} systematic by comparing, between data and N_i^{bkg}, the partial efficiencies at each signal channel's E_{extra} requirement listed in Table 6–1. The systematic uncertainties are taken as the average relative differences within the two control samples and are presented in Table 6–4. The $B^0 \to D^- \ell \nu$, $D^- \to K_S^0 \pi^-$ control sample is not used due to the lower statistics from both a smaller D branching fraction and the reconstruction efficiency of the K_S^0.

Table 6–4: The systematic uncertainty due to the E_{extra} requirement for each of the six signal channels. These values are determined by comparing the data and the MC partial efficiencies within the control samples.

Channel	E_{extra} uncertainty (%)
$K^+ \nu \overline{\nu}$	4.5
$[K^+ \pi^0] \nu \overline{\nu}$	6
$[K_S^0 \pi^+] \nu \overline{\nu}$	5.75
$K_S^0 \nu \overline{\nu}$	6
$[K^+ \pi^-] \nu \overline{\nu}$	6
$[K_S^0 \pi^0] \nu \overline{\nu}$	6.5

6.6.3 s_B Uncertainty

Because the neutrinos are undetected, the observed-s_B is computed from the four-momenta of the reconstructed $K^{(*)}$ and the B_{sig}. The imperfect resolution of these two four-vectors introduces an uncertainty on the estimated s_B value, which leads to a systematic uncertainty of the signal efficiency. Using generator-truth information in the signal MC, the generated true-s_B value is compared with that of the observed-s_B value. The difference is shown in Figure 6–13, where the resolution is taken as the full-width at half-maximum. The s_B requirement is then shifted by this resolution of about 1.0%, in both directions, in order to calculate the relative difference in the final signal efficiency. The systematic uncertainty is determined to be 3.6%.

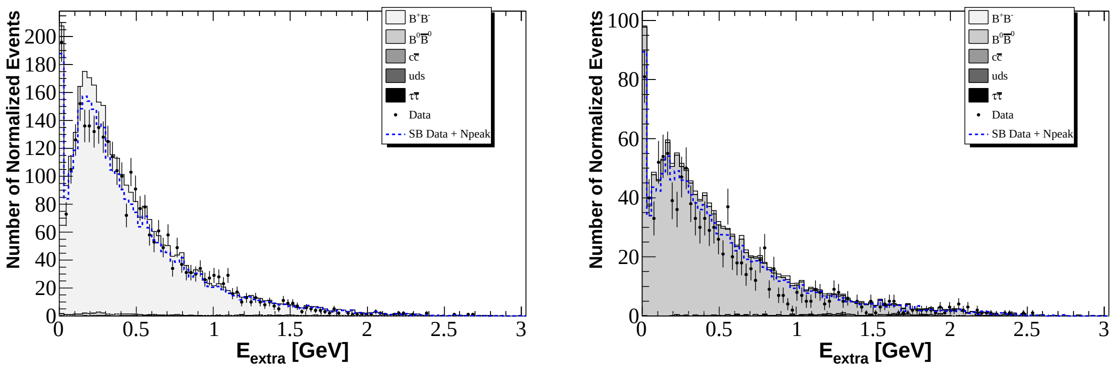

Figure 6–12: The E_{extra} distribution within the (top) $B^+ \to [K^-\pi^+]\ell\nu$ and (bottom) $B^0 \to [K^+\pi^-\pi^-]\ell\nu$ control samples, after applying all selection requirements except those on s_B and E_{extra}. The blue-dashed lines plot the SB-data substituted N_i^{bkg} $=(N_i^{\mathrm{comb}} + N_i^{\mathrm{peak}})$, which demonstrates the improved agreement with data (points) when compared with the stacked MC samples (shaded).

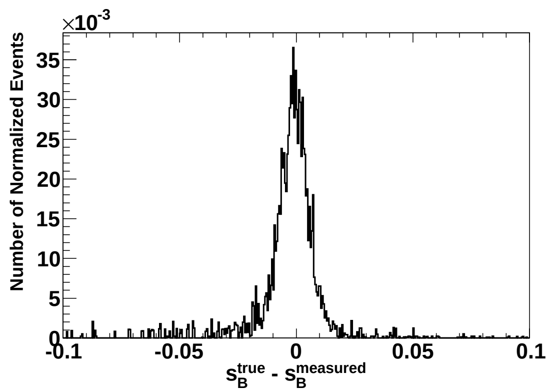

Figure 6–13: The resolution of the s_B variable, determined by subtracting the true-s_B value from the observed-s_B value in the signal MC, and fit with a peaking distribution to find the full-width at half-maximum.

Because the signal MC reweighting of the K^* polarization is related to the s_B variable, it is important to ensure that the analysis sensitivity to both SM $B \to K^{(*)}\nu\overline{\nu}$ and New Physics events is not overly dependent on the assumed SM shape of f_L versus s_B. The final signal efficiencies are compared with those obtained, assuming various arbitrarily chosen f_L distributions. The efficiency consistently changes by less than 3% within the low-s_B region, and less than 2% over the full-s_B spectrum. This indicates that the signal selection within the $B \to K^{(*)}\nu\overline{\nu}$ analysis is essentially independent of the f_L distribution and is sensitive to any realistic variation from possible New Physics contributions.

6.6.4 Additional Uncertainties

Because the C_{yield} normalization is determined after much of the signal selection is performed, uncertainties relating to much of the signal selection are already incorporated, including: the B_{tag} reconstruction, the Continuum Likelihood, low-multiplicity purity, signal-side track multiplicity, and PID requirements, as well as the K^0_S and K^* reconstructions.

However, there is still uncertainty due to the tight K^0_S and K^* mass windows, which are applied after the C_{yield} normalization is found. Since the reconstruction of the K^0_S and K^* candidates are independent of E_{extra}, the E_{extra} sideband is used to quantify the agreement between the data and the MC. The agreement within the mass peaks are shown in Figure 6–14. Breit-Wigner fits to the mass peaks in Figure 6–14 indicate a K^0_S mean mass of 0.497 GeV/c^2 for both modes in both data and SB-data substitution, and a width of 5.5 (6.4) MeV/c^2 for $B^+ \to [K^0_S\pi^+]\nu\overline{\nu}$ and 4.6 (4.5) MeV/c^2 for $B^0 \to K^0_S\nu\overline{\nu}$ for the SB-data substitution (data) peaks. Breit-Wigner fits to the K^* mass peaks for $B^0 \to [K^+\pi^-]\nu\overline{\nu}$ results indicate a mean mass of 0.89 (0.88) GeV/c^2 and a width of 8.5 (11.2) MeV/c^2 for the SB-data substitution (data) peaks. After applying the signal selection and the SB-data substitution, the partial efficiency from the tight K^0_S and K^* mass windows are determined in the data and

N_i^{bkg}. The stability of the partial efficiencies around the mass window are investigated, as well as the difference in the partial efficiency between different signal channels. Since the K_S^0 and K^* mass selection windows are relatively loose, at about 3σ and 2σ respectively, the uncertainties are low. The K_S^0 mass systematic uncertainty is taken to be 1.4%, and is applied to the $B^+ \to [K_S^0\pi^+]\nu\overline{\nu}$, $B^0 \to K_S^0\nu\overline{\nu}$, and $B^0 \to [K_S^0\pi^0]\nu\overline{\nu}$ channels. The K^* mass systematic uncertainty is taken to be 2.8%, which is applied to the $B^+ \to [K^+\pi^0]\nu\overline{\nu}$, $B^+ \to [K_S^0\pi^+]\nu\overline{\nu}$, $B^0 \to [K^+\pi^-]\nu\overline{\nu}$, and $B^0 \to [K_S^0\pi^0]\nu\overline{\nu}$ channels.

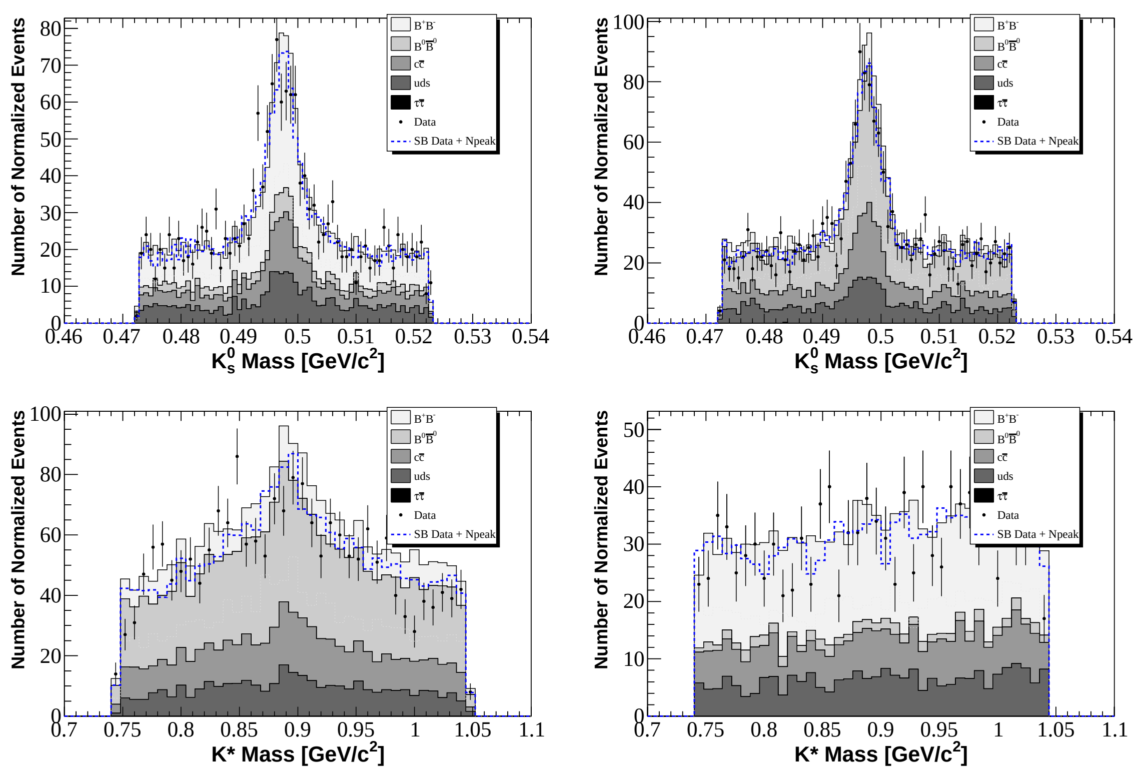

Figure 6–14: Distributions of the reconstructed (top) K_S^0 and (bottom) K^* invariant masses in the E_{extra} sideband of $E_{\mathrm{extra}} > 0.4\,\mathrm{GeV}$, after all other selection criteria are applied (except on s_B). The $B^+ \to [K_S^0\pi^+]\nu\overline{\nu}$ (top left), $B^0 \to K_S^0\nu\overline{\nu}$ (top right), $B^0 \to [K^+\pi^-]\nu\overline{\nu}$ (bottom left), and $B^+ \to [K^+\pi^0]\nu\overline{\nu}$ (bottom right) channels are shown. The blue-dashed lines plot the SB-data substituted $N_i^{\mathrm{bkg}} = (N_i^{\mathrm{comb}} + N_i^{\mathrm{peak}})$, which demonstrates the improved agreement with data (points) when compared with the stacked MC samples (shaded).

6.7 Branching Fraction Extraction

The $B \to K^{(*)}\nu\overline{\nu}$ analysis uses a cut-and-count technique, calculates the branching-fraction central value using Equation (5.12), and determines the branching-fraction upper limits using the Barlow method, as described in Section 5.7. Upper limits are determined for each of the six $B \to K^{(*)}\nu\overline{\nu}$ channels, as well as combined branching fractions for $B \to K\nu\overline{\nu}$, $B^+ \to K^{*+}\nu\overline{\nu}$, and $B^0 \to K^{*0}\nu\overline{\nu}$.

6.7.1 Signal Cross-Feed

In the $B \to K^{(*)}\nu\overline{\nu}$ analysis, there are cross-feed contributions between signal channels that must be incorporated into the determination of the branching fractions. There is significant cross-feed from $B^+ \to [K^+\pi^0]\nu\overline{\nu}$ into $B^+ \to K^+\nu\overline{\nu}$, and $B^0 \to [K^0_S\pi^0]\nu\overline{\nu}$ into $B^0 \to K^0_S\nu\overline{\nu}$, as well as non-negligible contributions from $B^+ \to K^+\nu\overline{\nu}$ into $B^+ \to [K^+\pi^0]\nu\overline{\nu}$, $B^0 \to K^0_S\nu\overline{\nu}$ into $B^0 \to [K^0_S\pi^0]\nu\overline{\nu}$, and $B^0 \to [K^+\pi^-]\nu\overline{\nu}$ into $B^0 \to K^0_S\nu\overline{\nu}$. To determine the branching fraction of a channel, $N_i^{\rm bkg}$ must be well-determined, but with cross-feed, $N_i^{\rm peak}$ depends on the branching fraction of the other signal channels that contribute to it.

This feed-back loop is combatted by simultaneously determining the branching fraction of all six $B \to K^{(*)}\nu\overline{\nu}$ signal channels. One can do this by solving a system of equations with a 6×6 matrix of the final signal efficiencies ($\epsilon_{ij}^{\rm sig}$ where i are the columns and j are the rows) given in Table 6–5. Equation (5.12) can be rewritten as:

$$\frac{N_j^{\rm sig}}{N_{B\overline{B}}} = \sum_i \mathcal{B}_i \epsilon_{ij}^{\rm sig} \tag{6.6}$$

where the subscript j refers to the observed signal yield in each channel (containing cross-feed from other signal channels) and the subscript i refers to the signal channel on which the signal efficiency is based. If the cross-feed were zero, the matrix would be diagonal. One can rearrange equation (6.6) as

$$\mathcal{B}_i = \sum_j \frac{N_j^{\rm sig}(\epsilon_{ij}^{\rm sig})^{-1}}{N_{B\overline{B}}} \tag{6.7}$$

where $(\epsilon_{ij}^{\text{sig}})^{-1}$ is the matrix inverse of Table 6–5.

Using Equation (6.7) and the inverse of the efficiency matrix, the branching-fraction central values for $B^+ \to K^+\nu\overline{\nu}$, $B^0 \to K^0\nu\overline{\nu}$, $B^+ \to K^{*+}\nu\overline{\nu}$, and $B^0 \to K^{*0}\nu\overline{\nu}$ are simultaneously calculated. The two $B^+ \to K^{*+}\nu\overline{\nu}$ ($B^0 \to K^{*0}\nu\overline{\nu}$) channels are combined in order to obtain a single $B^+ \to K^{*+}\nu\overline{\nu}$ ($B^0 \to K^{*0}\nu\overline{\nu}$) central value. Using these branching fractions, N_i^{peak} is re-evaluated using the new estimated number of cross-feed events within each channel, and the process is repeated. Although a total of five iterations are applied, the values essentially converge after only two.

Table 6–5: The efficiency values of signal events and cross-feed events between the various signal channels. The rows represent the observed signal channels in which an event is reconstructed, and the columns represent the actual signal decay as generated in the MC.

Actual → Observed ↓	$K^+\nu\overline{\nu}$	$[K^+\pi^0]\nu\overline{\nu}$	$[K^0_S\pi^+]\nu\overline{\nu}$	$K^0_S\nu\overline{\nu}$	$[K^+\pi^-]\nu\overline{\nu}$	$[K^0_S\pi^0]\nu\overline{\nu}$
$K^+\nu\overline{\nu}$	4.27×10^{-4}	4.24×10^{-6}	0	0	2.37×10^{-7}	0
$[K^+\pi^0]\nu\overline{\nu}$	1.05×10^{-5}	5.81×10^{-5}	0	0	0	0
$[K^0_S\pi^+]\nu\overline{\nu}$	0	0	4.81×10^{-5}	9.06×10^{-8}	0	8.95×10^{-8}
$K^0_S\nu\overline{\nu}$	0	0	4.79×10^{-7}	1.01×10^{-4}	2.25×10^{-7}	4.06×10^{-6}
$[K^+\pi^-]\nu\overline{\nu}$	3.99×10^{-7}	1.76×10^{-7}	9.69×10^{-8}	5.68×10^{-7}	1.20×10^{-4}	0
$[K^0_S\pi^0]\nu\overline{\nu}$	0	0	9.79×10^{-8}	3.15×10^{-6}	0	1.15×10^{-5}

6.8 $B \to K^{(*)}\nu\overline{\nu}$ Results

The SM-predicted branching fractions for $B \to K\nu\overline{\nu}$ ranges between 3.6×10^{-6} and 5.3×10^{-6}, and for $B \to K^*\nu\overline{\nu}$ between 7×10^{-6} and 13×10^{-6}. This analysis expects to produce at least one event in either $B \to K\nu\overline{\nu}$ channel if the branching fraction is above 1.6×10^{-6}, and at least one event in any of the four $B \to K^*\nu\overline{\nu}$ channels if the branching fraction is above 3.5×10^{-6}. Upon unblinding the data, the Barlow method is employed to find the upper limits at 90% CL (see Section 5.7). For the evaluation of $\mathcal{B}(B^+ \to K^0\nu\nu)$, the branching fraction of $K^0 \to K^0_S$ is assumed to be 50%. The number of observed events, as well as the branching-fraction central values and upper limits, are provided in Tables 6–6 and 6–7.

Table 6–6: The expected $B \to K\nu\overline{\nu}$ background yields ($N_i^{\rm bkg} = N_i^{\rm comb} + N_i^{\rm peak}$), signal efficiencies ($\epsilon_i^{\rm sig}$), number of signal events ($N_i^{\rm sig}$) assuming $\mathcal{B}(B \to K\nu\overline{\nu}) = 4\times10^{-6}$, number of observed data events ($N_i^{\rm obs}$) and their corresponding significance, and the resulting branching-fraction central values ($\mathcal{B}_i$) and limits at 90% CL. The average central value and combined limits are also provided. Uncertainties are given as statistical ± systematic.

	$B^+ \to K^+\nu\overline{\nu}$	$B^0 \to K^0\nu\overline{\nu}$
$\epsilon_i^{\rm sig}$ ($\times10^{-5}$)	$43.8 \pm 0.7 \pm 3.0$	$10.3 \pm 0.2 \pm 1.0$
Expected $N_i^{\rm sig}$	$0.83 \pm 0.01 \pm 0.06$	$0.19 \pm 0.00 \pm 0.02$
$N_i^{\rm comb}$	$1.1 \pm 0.4 \pm 0.0$	$0.9 \pm 0.4 \pm 0.1$
$N_i^{\rm peak}$	$1.8 \pm 0.4 \pm 0.1$	$2.0 \pm 0.5 \pm 0.2$
$N_i^{\rm bkg}$	$2.9 \pm 0.6 \pm 0.1$	$2.9 \pm 0.6 \pm 0.2$
$N_i^{\rm obs}$	6	3
Significance	1.55σ	0.12σ
Limits	$(> 0.4, < 3.7) \times 10^{-5}$	$< 8.0 \times 10^{-5}$
$\mathcal{B}_i$	$(1.5^{+1.7+0.3}_{-0.8-0.2}) \times 10^{-5}$	$(0.14^{+6.0+1.5}_{-1.9-0.9}) \times 10^{-5}$
Combined Limits	$(> 0.2, < 3.2) \times 10^{-5}$	
$\mathcal{B}(B \to K\nu\overline{\nu})$	$(1.4^{+1.4+0.3}_{-0.9-0.2}) \times 10^{-5}$	

Table 6–7: The expected $B \to K^*\nu\overline{\nu}$ background yields ($N_i^{\rm bkg} = N_i^{\rm comb} + N_i^{\rm peak}$), signal efficiencies ($\epsilon_i^{\rm sig}$), number of signal events ($N_i^{\rm sig}$) assuming $\mathcal{B}(B \to K^*\nu\overline{\nu}) = 13\times10^{-6}$, number of observed data events ($N_i^{\rm obs}$) and their corresponding significance, and the resulting branching-fraction central values ($\mathcal{B}_i$) and limits at 90% CL. The average central values and combined limits are also provided. Uncertainties are given as statistical ± systematic.

	$B^+ \to [K^+\pi^0]\nu\overline{\nu}$	$B^+ \to [K^0_S\pi^+]\nu\overline{\nu}$	$B^0 \to [K^+\pi^-]\nu\overline{\nu}$	$B^0 \to [K^0_S\pi^0]\nu\overline{\nu}$
$\epsilon_i^{\rm sig}$ ($\times10^{-5}$)	$6.0 \pm 0.2 \pm 0.5$	$4.9 \pm 0.2 \pm 0.4$	$12.2 \pm 0.3 \pm 1.1$	$1.2 \pm 0.1 \pm 0.1$
Expected $N_i^{\rm sig}$	$0.37 \pm 0.01 \pm 0.03$	$0.30 \pm 0.01 \pm 0.03$	$0.75 \pm 0.02 \pm 0.07$	$0.07 \pm 0.01 \pm 0.01$
$N_i^{\rm comb}$	$0.8 \pm 0.3 \pm 0.0$	$1.1 \pm 0.4 \pm 0.0$	$2.0 \pm 0.5 \pm 0.1$	$0.5 \pm 0.3 \pm 0.0$
$N_i^{\rm peak}$	$1.3 \pm 0.4 \pm 0.1$	$1.2 \pm 0.4 \pm 0.1$	$5.0 \pm 0.8 \pm 0.6$	$0.2 \pm 0.2 \pm 0.0$
$N_i^{\rm bkg}$	$2.0 \pm 0.5 \pm 0.1$	$2.3 \pm 0.5 \pm 0.1$	$7.0 \pm 0.9 \pm 0.6$	$0.7 \pm 0.3 \pm 0.0$
$N_i^{\rm obs}$	3	3	7	2
Significance	0.68σ	0.50σ	0.10σ	1.14σ
Limits	$< 16.9 \times 10^{-5}$	$< 19.2 \times 10^{-5}$	$< 8.7 \times 10^{-5}$	$< 84 \times 10^{-5}$
$\mathcal{B}_i$	$(3.5^{+10.3+2.1}_{-3.2\ -1.2})\times10^{-5}$	$(3.0^{+12.5+2.7}_{-3.9\ -1.5})\times10^{-5}$	$(0.08^{+6.6+2.2}_{-3.1-1.4})\times10^{-5}$	$(23^{+47+11}_{-11-4})\times10^{-5}$
Combined Limits	$< 11.5 \times 10^{-5}$		$< 9.2 \times 10^{-5}$	
$\mathcal{B}(B^{+/0} \to K^{*+/0}\nu\overline{\nu})$	$(3.3^{+6.2+1.6}_{-3.6-1.3}) \times 10^{-5}$		$(2.0^{+5.2+1.7}_{-4.3-1.7}) \times 10^{-5}$	
Combined Limits	$< 7.8 \times 10^{-5}$			
$\mathcal{B}(B \to K^*\nu\overline{\nu})$	$(2.9^{+2.8+1.1}_{-3.8-1.0}) \times 10^{-5}$			

Overall, the number and distribution of the observed data is consistent with the expected background within various sideband regions, as well as within the signal region. The resulting branching-fraction upper limits are consistent with SM predictions. There is a slight excess of data events within the $B^+ \to K^+\nu\overline{\nu}$ channel. However, the two-sided limits are still consistent with the expected SM branching fraction. Five of the six observed events in the $B^+ \to K^+\nu\overline{\nu}$ channel have an E_{extra} of zero, as shown in Figure 6–15, which suggests that the excess may be, in part, due to signal events, particularly since approximately one signal event is expected at the SM-predicted branching fraction rates.

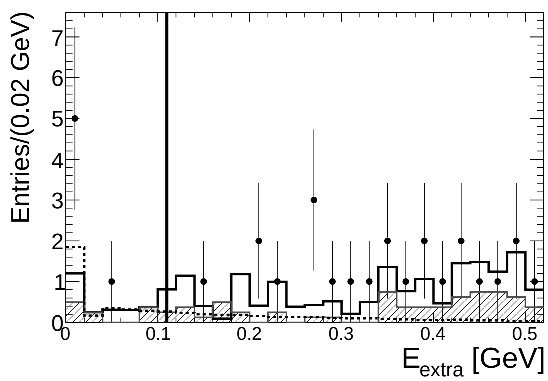

Figure 6–15: The distribution of E_{extra} after the full signal selection in the $B^+ \to K^+\nu\overline{\nu}$ channel. The m_{ES}-peaking background contribution (solid) is added atop the non-peaking background component (shaded) and overlayed with the data (points). The signal MC (dashed) is normalized to $\mathcal{B} = 1.55 \times 10^{-5}$. Events to the left of the vertical lines are selected.

The previous constraints on New Physics that may appear within the Wilson coefficients, as given in Fig. 2–5, are improved slightly by the upper limits from this $B \to K^*\nu\overline{\nu}$ analysis. In addition, the lower limits, obtained in both the $B^+ \to K^+\nu\overline{\nu}$ and the combined $B \to K\nu\overline{\nu}$ results, reduce a significant portion of the Wilson coefficient parameter-space, as shown in Figure 6–16. These constraints are still consistent with the SM expected values.

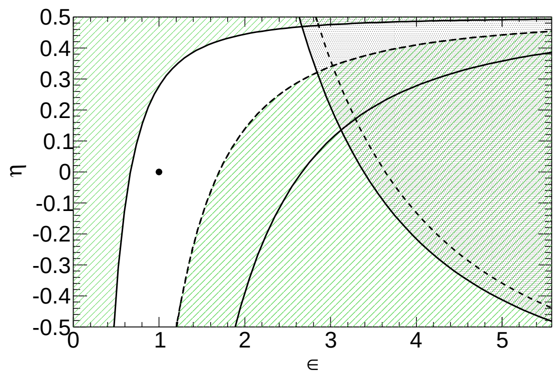

Figure 6–16: The updated constraints at 90% CL on ϵ and η of Equations (2.19) and (2.20), following the example of Fig. 2–5. The $B \to K\nu\overline{\nu}$ (green shading) and $B \to K^{*}\nu\overline{\nu}$ (grey shading) excluded areas are determined from the upper and lower combined-channel limits of this $B \to K^{(*)}\nu\overline{\nu}$ analysis (solid line) and from the most-stringent upper limits from the previous semileptonic-tag analyses listed in Table 2–5 (dashed line). The dot shows the SM expected values.

6.8.1 Partial Branching Fraction Results

There are many New Physics models of the $B \to K^{(*)}\nu\overline{\nu}$ process, all of which show alterations to the s_B distribution, some of which are most significant in the high-s_B region, as shown in Figure 2–7. By restricting the search to the low-s_B region, the sensitivity to the SM-predicted decay would be maximized, but this analysis would miss any evidence of New Physics in the higher-s_B region. Therefore, in addition to measuring an upper limit on the SM $B \to K^{(*)}\nu\overline{\nu}$ decays within the low-s_B region, partial branching fractions are determined over the full s_B distribution. The distributions of the data and the expected background and signal events, over the full s_B distribution, are provided in Figure 6–17.

After the full signal selection, the signal efficiency as a function of the s_B distribution is found to be approximately flat (within one sigma) over most of the s_B range,

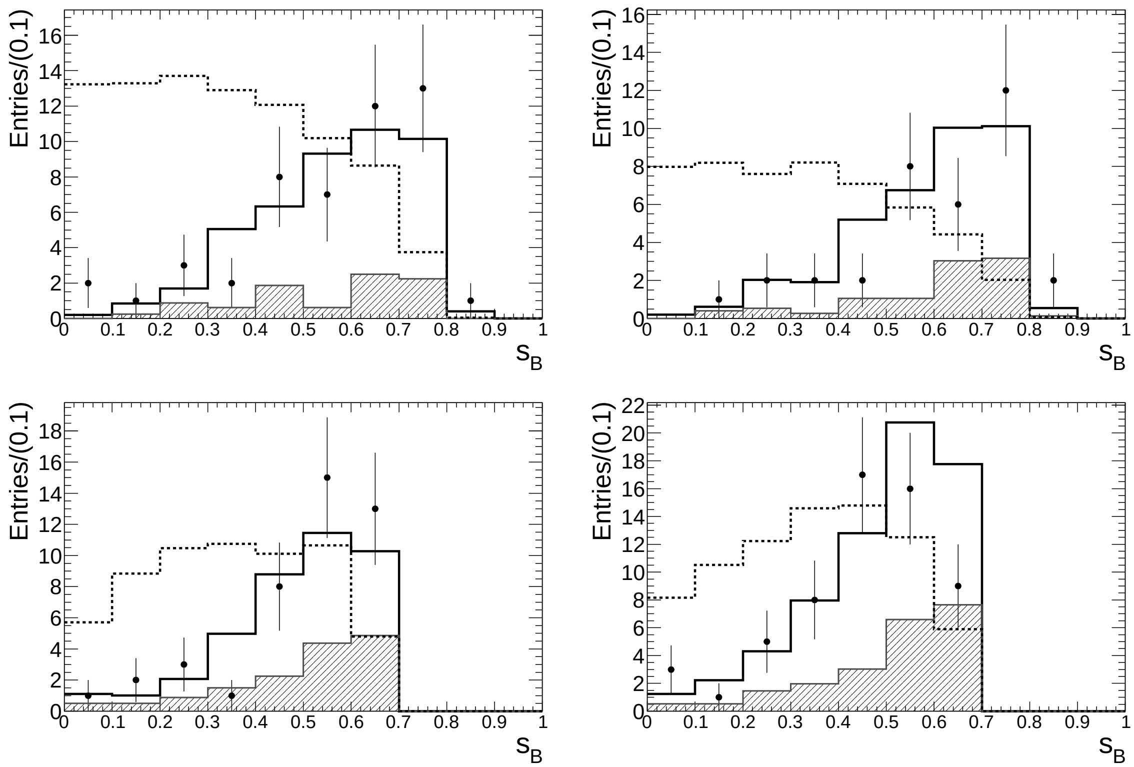

Figure 6–17: The distribution of s_B after the full signal selection in the four signal channels: (top left) $B^+ \to K^+\nu\overline{\nu}$, (top right) $B^0 \to K^0\nu\overline{\nu}$, (bottom left) $B^+ \to K^{*+}\nu\overline{\nu}$, and (bottom right) $B^0 \to K^{*0}\nu\overline{\nu}$. The m_{ES}-peaking background contribution (solid) is added atop the non-peaking background component (shaded) and overlayed with the data (points). For visibility, the SM-predicted distribution of the signal MC (dashed) is normalized to $\mathcal{B} = 20 \times 10^{-5}$ in $B^+ \to K^+\nu\overline{\nu}$ and $\mathcal{B} = 50 \times 10^{-5}$ in the other three channels. The signal region is defined as $s_B < 0.3$, but the full spectrum is used to determine partial branching fractions.

as shown in Figure 6–18.[3] A flat efficiency indicates that the analysis without the s_B requirement is essentially independent of signal kinematics and theoretical models and, therefore, can provide easy-to-interpret partial branching fraction results.

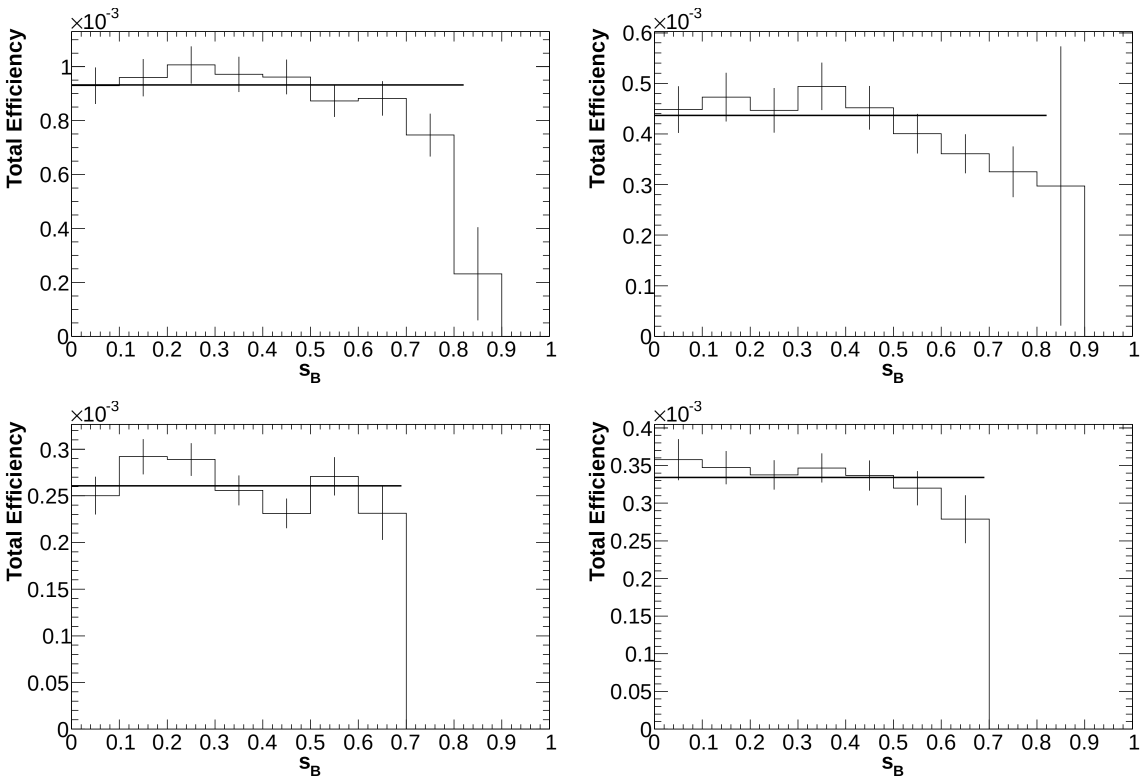

Figure 6–18: The total signal efficiency versus the observable-s_B after the full signal selection in the four signal channels: (top left) $B^+ \to K^+\nu\overline{\nu}$, (top right) $B^0 \to K^0\nu\overline{\nu}$, (bottom left) $B^+ \to K^{*+}\nu\overline{\nu}$, and (bottom right) $B^0 \to K^{*0}\nu\overline{\nu}$. The horizontal line is the value of the total signal efficiency over the full s_B spectrum.

The partial branching fractions are determined using the same signal selection values that were optimized within the low s_B region, except for the $s_B < 0.3$ restriction. The s_B distribution is split into bins of 0.1 and a partial branching fraction is

[3]The drop in the last bin is due to the kinematic cut-off of s_B within this bin. The decrease in the last few bins is likely due to lower PID efficiencies with low-momentum particles.

calculated in each bin using:

$$\Delta\mathcal{B}(B \to K^{(*)}\nu\overline{\nu})_{\rm bin} = \frac{(N_i^{\rm obs} - N_i^{\rm bkg})_{\rm bin}}{N_{B\overline{B}} \times \epsilon_i^{\rm sigFull}} \tag{6.8}$$

where the numerator refers to the number of observed and expected background events within a given bin, and $\epsilon_i^{\rm sigFull}$ is the signal efficiency over the full s_B distribution. Thus, one could sum the partial branching fractions in each bin (and add the uncertainties in quadrature) to obtain a model-independent branching fraction over the whole s_B distribution. The partial branching fractions also provide theorists with the means to place their own limits on various New Physics models that distort the SM s_B distribution. Model-specific branching-fraction central values and one-sigma uncertainties can be computed by summing the central values within the bins that are dominant in that model, and dividing the sum by the fraction of the signal distribution that is expected by that model to lie within those same s_B bins. The partial branching-fraction central values and asymmetric one-sigma uncertainties are given in Figure 6–19. Because a frequentist method of measurement is used, with no Bayesian priors, the branching-fraction central values and uncertainties can extend into the negative, unphysical regions. Nevertheless, almost all of the upper values on the uncertainties are positive, which results in positive upper limits at the 90% CL.

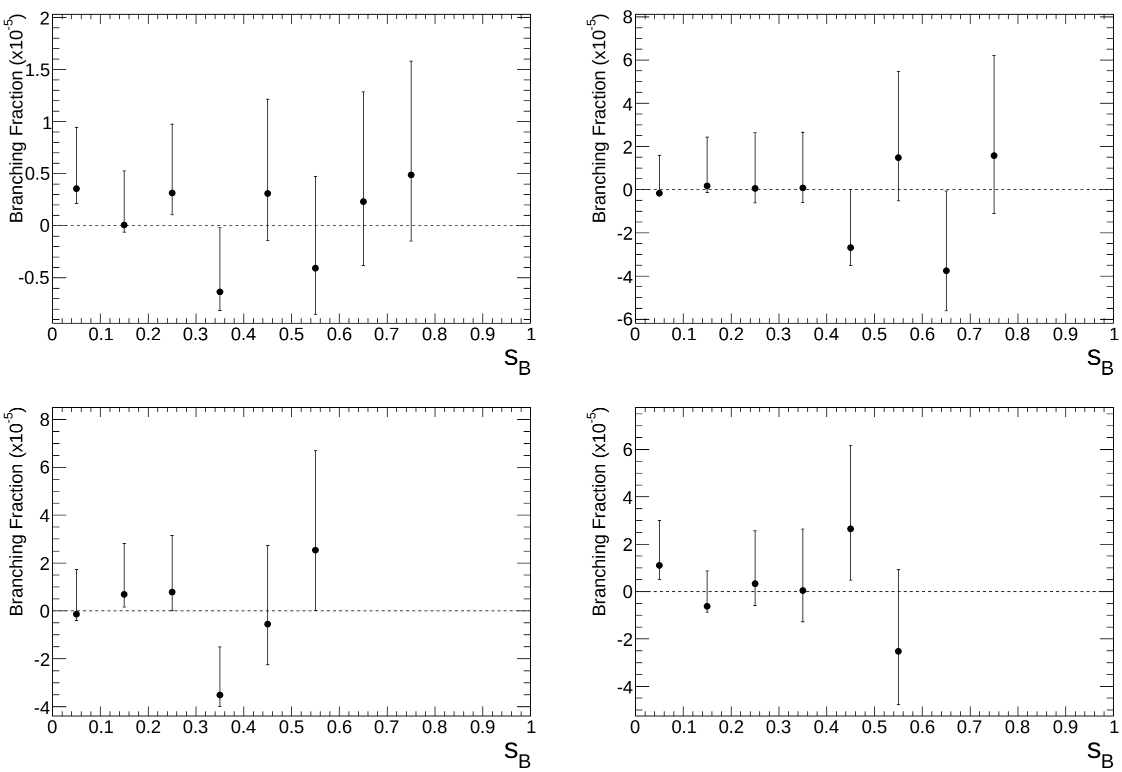

Figure 6–19: The central values (points with $1\,\sigma$ error bars) of the partial branching fraction versus s_B, for the four signal channels: (top left) $B^+ \to K^+\nu\overline{\nu}$, (top right) $B^0 \to K^0\nu\overline{\nu}$, (bottom left) $B^+ \to K^{*+}\nu\overline{\nu}$, and (bottom right) $B^0 \to K^{*0}\nu\overline{\nu}$.

CHAPTER 7
Conclusions

This thesis presents the searches of the rare decays $B^+ \to \ell^+\nu_\ell\gamma$ and $B \to K^{(*)}\nu\overline{\nu}$, using the full BABAR dataset. Both searches employ the hadronic-tag reconstruction technique, in which one B meson is fully reconstructed from several hadronic final states, and evidence of a signal decay is searched for in the rest of the event. Various signal selection criteria are utilized and optimized in order to maximize the signal efficiency while minimizing the number of background events. The estimate of the background events uses a combination of $B\overline{B}$ MC samples and sideband data.

Measurements of the $B^+ \to \ell^+\nu_\ell\gamma$ branching fractions are important for extracting the value of the first inverse-moment of the B meson wave function, which is of theoretical importance but has large uncertainty. In the $B^+ \to \ell^+\nu_\ell\gamma$ analysis, after identifying the signal lepton and photon, the selection mainly relies on two variables which ensure that the kinematics resemble a three-body decay ($\cos\theta_{\ell\nu}$) with the reconstructed mass of the neutrino (m_ν^2) near zero. The primary background is from $B^+ \to X_u^0\ell^+\nu_\ell$ events, which are further suppressed with additional selection criteria. Since no restrictions are placed on the signal lepton or photon energies, the selection is valid over the full phase-space and is thus considered independent of the $B \to \gamma$ form-factor model. No signal events are observed, but branching-fraction upper limits, at 90% CL, are set at $\mathcal{B}(B^+ \to e^+\nu_e\gamma) < 17 \times 10^{-6}$, $\mathcal{B}(B^+ \to \mu^+\nu_\mu\gamma) < 24 \times 10^{-6}$, and $\mathcal{B}(B^+ \to \ell^+\nu_\ell\gamma) < 15.6 \times 10^{-6}$ [19]. These are not only the most stringent published upper limits for $B^+ \to \ell^+\nu_\ell\gamma$, but they are also the only model-independent limits. Model-specific limits are determined, as well as a limit that requires the signal photon to be relatively large.

Since the $B \to K^{(*)}\nu\overline{\nu}$ decays are forbidden at tree-level in the SM, various New Physics scenarios can contribute to enhancements in the SM branching fraction prediction, as well as alter the kinematic distribution of the decay. In the $B \to K^{(*)}\nu\overline{\nu}$ analysis, a $K^{(*)}$ meson is reconstructed and the unaccounted-for energy in the rest of the event (E_{extra}) is required to be minimal. Furthermore, the momentum of the reconstructed $K^{(*)}$ is required to be relatively large, as predicted by the SM. No signal events are observed, but branching-fraction upper limits, at 90% CL, are set at $\mathcal{B}(B^+ \to K^+\nu\overline{\nu}) < 3.7 \times 10^{-5}$, $\mathcal{B}(B^0 \to K^0\nu\overline{\nu}) < 8.0 \times 10^{-5}$, $\mathcal{B}(B^+ \to K^{*+}\nu\overline{\nu}) < 11.5 \times 10^{-5}$, and $\mathcal{B}(B^0 \to K^{*0}\nu\overline{\nu}) < 9.2 \times 10^{-5}$, all at the 90% confidence level. Except for the $B^+ \to K^+\nu\overline{\nu}$ channel, these upper limits are currently the world's most stringent upper limits using the hadronic-tag reconstruction method. This analysis also determines the first *BABAR* upper limits on $B^0 \to K^0_S\nu\overline{\nu}$ using the hadronic tag reconstruction. The upper and lower limits from this analysis tighten the constraints on the Wilson coefficient parameter-space, as shown in Figure 6–16. However, because the selection requires a high-momentum kaon, the New Physics scenarios that suggest enhancements in the region of high missing-momentum are not strongly constrained by these limits. Therefore, this is the only search that provides partial $B \to K^{(*)}\nu\overline{\nu}$ branching-fractions over the full $K^{(*)}$ kinematic range, explicitly providing sensitivity to New Physics possibilities that may enhance the kinematic spectrum. These partial branching fractions provide limits to some of these New Physics scenarios, such as scalar invisible particles, at the level of a few $\times 10^{-5}$.

Neither of the rare decays $B^+ \to \ell^+\nu_\ell\gamma$ and $B \to K^{(*)}\nu\overline{\nu}$ have been observed yet. However, the upper limits on these decays are approaching the SM-predicted branching fractions, and there is possibility that several signal events have already been detected, although with insignificant statistics to claim observation. Since these decays contain neutrinos in their final state, detecting them requires a hermetic detector similar to *BABAR*. The additional statistics needed for observation of these decays are expected to be produced at the next-generation B Factories, SuperB [93] and Belle II [94], which are similar in design to BABAR but anticipate approximately 100 times the current B Factory statistics. With such a large data sample, one expects that $B^+ \to \ell^+ \nu_\ell \gamma$ decays will not only be observed, but the branching fraction measurements will be able to constrain SM parameters, such as the B-meson distribution amplitude λ_B. Likewise, $B \to K^{(*)} \nu \overline{\nu}$ decays are expected to be observed, hopefully with enough statistics to determine the K^* polarization fraction f_L, in order to further constrain New Physics models. Until then, however, the $B^+ \to \ell^+ \nu_\ell \gamma$ and $B \to K^{(*)} \nu \overline{\nu}$ branching-fraction upper limits that are discussed in this thesis can and will be used to improve our understanding of the Standard Model and beyond.

Appendix: Author Declaration

This thesis has been written entirely by the author while in candidature for a Ph.D. degree at McGill University. The physics analyses presented from Chapter 5 onwards, as well as Sections 4.3 and 4.4, were performed predominantly by the author. Unless otherwise referenced, all the plots within the thesis were also made by the author. The hadronic-tag reconstruction algorithm, described in 4.1, was developed by members of the *BABAR* Collaboration. The MC and data samples used in the $B^+ \to \ell^+ \nu_\ell \gamma$ analysis were produced using the *BABAR* software, along with code written by the thesis supervisor, Professor Steven Robertson. The samples used in the $B \to K^{(*)} \nu \overline{\nu}$ analysis were produced by the author after editing this same code. Neither the theoretical summaries in Chapter 2 nor the *BABAR* experiment description in Chapter 3 contain any original work of the author. However, the author did perform studies on the energy correction algorithm, used within the *BABAR* MC simulations of neutral clusters within the EMC, in order to improve agreement with data.

References

[1] E. Noether. Invariant variation problems. *Gott. Nachr.*, 1918:235, 1918.

[2] K. Nakamura et al. Review of particle physics. *J. Phys.*, G37:075021, 2010. 2011 partial update for 2012 edition.

[3] Y. Fukuda et al. Measurements of the solar neutrino flux from Super-Kamiokande's first 300 days. *Phys. Rev. Lett.*, 81:1158–1162, 1998.

[4] G. Aad et al. Combined search for the Standard Model Higgs boson using up to 4.9 fb-1 of pp collision data at sqrt(s) = 7 TeV with the ATLAS detector at the LHC. *Phys. Lett.*, B710:49, 2012.

[5] S. Chatrchyan et al. Combined results of searches for the standard model Higgs boson in pp collisions at sqrt(s) = 7 TeV. *Phys. Lett.*, B710:26, 2012.

[6] R. Barate et al. Search for the standard model Higgs boson at LEP. *Phys. Lett.*, B565:61, 2003.

[7] E. Eichten, K. Gottfried, T. Kinoshita, K. D. Lane, and T. M. Yan. Charmonium: The model. *Phys. Rev. D*, 17:3090–3117, 1978.

[8] B. R. Martin and G. Shaw. *Particle Physics*. John Wiley, Chichester, second edition, 1992.

[9] P. Higgs. Broken symmetries and the masses of gauge bosons. *Phys. Rev. Lett.*, 13:508, 1964.

[10] S. L. Glashow. Partial-symmetries of weak interactions. *Nuclear Physics*, 22(4):579, 1961.

[11] M. Kobayashi and T. Maskawa. CP-Violation in the renormalizable theory of weak interaction. *Prog. Theor. Phys.*, 49:652, 1973.

[12] L. Wolfenstein. Parametrization of the Kobayashi-Maskawa matrix. *Phys. Rev. Lett.*, 51:1945, 1983.

[13] J. H. Christenson, J. W. Cronin, V. L. Fitch, and R. Turlay. Evidence for the 2π decay of the K_2^0 meson. *Phys. Rev. Lett.*, 13:138, 1964.

[14] A. D. Sakharov. Violation of CP in variance, C asymmetry, and baryon asymmetry of the universe. *Soviet Physics Uspekhi*, 34:392, 1991.

[15] G. Buchalla, A. J. Buras, and M. E. Lautenbacher. Weak decays beyond leading logarithms. *Rev. Mod. Phys.*, 68:1125, 1996.

[16] P. Minkowski. Mu $\to$ e gamma at a rate of one out of 1-billion muon decays? *Phys. Lett.*, B67:421, 1977.

[17] S. Dimopoulos and H. Georgi. Softly broken supersymmetry and SU(5). *Nuclear Physics B*, 193:150, 1981.

[18] G. Bertone, D. Hooper, and J. Silk. Particle dark matter: Evidence, candidates and constraints. *Phys. Rept.*, 405:279–390, 2005.

[19] B. Aubert et al. A Model-independent search for the decay B+ $\to$ l+ nu$_l$ gamma. *Phys. Rev.*, D80:111105, 2009.

[20] T. E. Browder et al. Search for B $\to$ mu anti-nu/mu gamma and B $\to$ e anti-nu/e gamma. *Phys. Rev.*, D56:11, 1997.

[21] K. Abe et al. Search for B+ $\to$ mu+ nu and B+ $\to$ l+ nu gamma) decays. arXiv:hep-ex/0408132, 2004.

[22] B. Aubert et al. Search for the radiative leptonic decay B+ $\to$ gamma l+ nu$_l$. arXiv:0704.1478 [hep-ex], 2007.

[23] B. Aubert et al. A Search for the decay B+ $\to$ K+ nu anti-nu. *Phys. Rev. Lett.*, 94:101801, 2005.

[24] K. F. Chen et al. Search for B $\to$ h(*) nu nubar Decays at Belle. *Phys. Rev. Lett.*, 99:221802, 2007.

[25] B. Aubert et al. Search for B $\to$ K* nu anti-nu decays. *Phys. Rev.*, D78:072007, 2008.

[26] P. del Amo Sanchez et al. Search for the rare decay B $\to$ K nu nubar. *Phys. Rev.*, D82:112002, 2010.

[27] A. Gray et al. The B meson decay constant from unquenched lattice QCD. *Phys. Rev. Lett.*, 95:212001, 2005.

[28] X. G. Wu, Y. Yu, G. Chen, and H. Y. Han. A Comparative study of f_B within QCD sum rules with two typical correlators up to next-to-leading rrder. *Commun. Theor. Phys.*, 55:635–639, 2011.

[29] A. Bazavov et al. B- and D-meson decay constants from three-flavor lattice QCD. arXiv:1112.3051 [hep-lat], 2011.

[30] H. Na et al. The B and B_s meson decay constants from lattice QCD. arXiv:1202.4914 [hep-lat], 2012.

[31] Bernard Aubert et al. A Search for B+ $\rightarrow$ l+ nu recoiling against B- $\rightarrow$ D0 l-anti-nu X. *Phys. Rev.*, D81:051101, 2010.

[32] K. Hara et al. Evidence for $B^- \rightarrow \tau^- \bar{\nu}$ with a semileptonic tagging method. *Phys. Rev.*, D82:071101, 2010.

[33] G. Burdman, J. T. Goldman, and D. Wyler. Radiative leptonic decays of heavy mesons. *Phys. Rev.*, D51:111, 1995.

[34] D. Atwood, G. Eilam, and A. Soni. Pure leptonic radiative decays $B^{\pm}$, $D_s \rightarrow \ell\nu\gamma$ and the annihilation graph. *Mod. Phys. Lett.*, A11:1061, 1996.

[35] P. Colangelo, F. De Fazio, and G. Nardulli. On the decay mode B- $\rightarrow$ mu- anti-nu gamma. *Phys. Lett.*, B386:328–334, 1996.

[36] C. W. Hwang. Radiative leptonic decays of heavy mesons in heavy quark limit. *Eur. Phys. J.*, C46:379, 2006.

[37] M. Beneke and J. Rohrwild. B meson distribution amplitude from B $\rightarrow$ gamma l nu. *Eur. Phys. J.*, C71:1818, 2011.

[38] G. P. Korchemsky, D. Pirjol, and T. M. Yan. Radiative leptonic decays of B mesons in QCD. *Phys. Rev.*, D61:114510, 2000.

[39] Y. Y. Charng and H. N. Li. B meson wave function from the B $\rightarrow$ gamma l nu decay. *Phys. Rev.*, D72:014003, 2005.

[40] A. Le Yaouanc, L. Oliver, and J. C. Raynal. Relation between light cone distribution amplitudes and shape function in B mesons. *Phys. Rev.*, D77:034005, 2008.

[41] M. Beneke, T. Huber, and Xin-Qiang Li. NNLO vertex corrections to non-leptonic B decays: Tree amplitudes. *Nucl. Phys.*, B832:109–151, 2010.

[42] P. Ball and E. Kou. B $\rightarrow$ gamma e nu transitions from QCD sum rules on the light-cone. *JHEP*, 04:029, 2003.

[43] S. Descotes-Genon and C. T. Sachrajda. Factorization, the light-cone distribution amplitude of the B-meson and the radiative decay B *to* gamma l nu. *Nucl. Phys.*, B650:356–390, 2003.

[44] E. Lunghi, D. Pirjol, and D. Wyler. Factorization in leptonic radiative B $\rightarrow$ gamma e nu decays. *Nucl. Phys.*, B649:349, 2003.

[45] D. Becirevic, B. Haas, and E. Kou. Soft photon problem in leptonic B-decays. *Phys. Lett.*, B681:257, 2009.

[46] M. S. Khan, M. J. Aslam, A. H. S. Gilani, and Riazuddin. Form factors and branching ratio for the B $\rightarrow$ l nu gamma decay. *Eur. Phys. J.*, C49:665–674, 2007.

[47] W. Altmannshofer, A. J. Buras, D. M. Straub, and M. Wick. New strategies for New Physics search in B → K* nu anti-nu, B → K nu anti-nu and B → X(s) nu anti-nu decays. *JHEP*, 04:022, 2009.

[48] M. Bartsch, M. Beylich, G. Buchalla, and D. N. Gao. Precision flavour physics with $B \to K\nu\bar{\nu}$ and $B \to Kl^+l^-$. *JHEP*, 11:011, 2009.

[49] T. Hurth, G. Isidori, J. F. Kamenik, and F. Mescia. Constraints on new physics in MFV models: A Model- independent analysis of Delta F = 1 processes. *Nucl. Phys.*, B808:326, 2009.

[50] G. Buchalla, G. Hiller, and G. Isidori. Phenomenology of nonstandard Z couplings in exclusive semileptonic b → s transitions. *Phys. Rev.*, D63:014015, 2000.

[51] X. Q. Li, Y. D. Yang, and X. B. Yuan. Anomalous tqZ coupling effects in rare B- and K-meson decays. *JHEP*, 03:018, 2012.

[52] C. Bird, R. V. Kowalewski, and M. Pospelov. Dark matter pair-production in b → s transitions. *Mod. Phys. Lett.*, A21:457, 2006. See also C. Bird et al., *Phys. Rev. Lett.*, 93:201803, 2004.

[53] P. Ball and R. Zwicky. New results on B → pi, K, eta decay form factors from light- cone sum rules. *Phys. Rev.*, D71:014015, 2005.

[54] J. H. Jeon, C. S. Kim, J. Lee, and C. Yu. Exclusive B → M nu anti-nu (M= pi, K, rho, K*) decays and leptophobic Z' model. *Phys. Lett.*, B636:270, 2006.

[55] P. Colangelo, F. De Fazio, R. Ferrandes, and T. N. Pham. Exclusive B → K(*) l+ l-, B → K(*) nu anti-nu and B → K* gamma transitions in a scenario with a single universal extra dimension. *Phys. Rev.*, D73:115006, 2006.

[56] B. Aubert et al. Direct CP, lepton flavor and isospin asymmetries in the decays $B \to K^{(*)}\ell^+\ell^-$. *Phys. Rev. Lett.*, 102:091803, 2009.

[57] J. F. Kamenik and C. Smith. FCNC portals to the dark sector. *JHEP*, 03:090, 2012.

[58] D. McKeen. WIMPless dark matter and meson decays with missing energy. *Phys. Rev.*, D79:114001, 2009.

[59] H. Davoudiasl, H. S. Lee, and W. J. Marciano. 'Dark' Z implications for parity violation, rare meson decays, and Higgs physics. arXiv:1203.2947 [hep-ph], 2012.

[60] T. M. Aliev, A. S. Cornell, and N. Gaur. B to K(K*) missing energy in Unparticle physics. *JHEP*, 07:072, 2007.

[61] G. Finocchiaro et al. Observation of the Υ''' at the Cornell Electron Storage Ring. *Phys. Rev. Lett.*, 45:222, 1980. Image found at http://www.lns.cornell.edu/public/lab-info/upsilon.html.

[62] No author given. PEP-II: An Asymmetric B factory. Conceptual design report. SLAC-418, 1993.

[63] B. Aubert et al. The BaBar detector. *Nucl. Instrum. Meth.*, A479:1, 2002.

[64] ed. Harrison, P. F. and ed. Quinn, Helen R. The BABAR physics book: Physics at an asymmetric B factory. *SLAC-R-504*, 1998.

[65] I. Adam et al. The DIRC particle identification system for the BaBar experiment. *Nuclear Instruments and Methods in Physics Research Section A: Accelerators, Spectrometers, Detectors and Associated Equipment*, 538(13):281, 2005.

[66] B. Aubert et al. The babar detector: upgrades, operation and performance. Will be published in 2012.

[67] P. Billoir. Track fitting with multiple scattering: A new method. *Nuclear Instruments and Methods in Physics Research*, 225(2):352, 1984.

[68] D. J. Lange. The EvtGen particle decay simulation package. *Nucl. Instrum. Meth.*, A462:152–155, 2001.

[69] T. Sjostrand, S. Mrenna, and P. Z. Skands. PYTHIA 6.4 physics and manual. *JHEP*, 05:026, 2006.

[70] P. Golonka and Z. Was. PHOTOS Monte Carlo: A Precision tool for QED corrections in Z and W decays. *Eur. Phys. J.*, C45:97, 2006.

[71] J. Allison et al. Geant4 developments and applications. *Nuclear Science, IEEE Transactions on*, 53(1):270, 2006.

[72] D. Lindemann. Smearing of Monte Carlo calorimeter simulation – Updated using R24c. Internal BABAR Analysis Document #2278, 2010.

[73] G. Punzi. Sensitivity of searches for new signals and its optimization. arXiv:physics/0308063, 2003.

[74] I. Antcheva et al. ROOT A C++ framework for petabyte data storage, statistical analysis and visualization. *Comp. Phys. Comm.*, 180(12):2499, 2009.

[75] G. C. Fox and S. Wolfram. Observables for the analysis of event shapes in e^+e^- annihilation and other processes. *Phys. Rev. Lett.*, 41:1581, 1978.

[76] B. Aubert et al. Measurements of B $\rightarrow$ pi, eta, eta-prime l nu$_l$ branching fractions and determination of |V(ub)| with semileptonically tagged B mesons. *Phys. Rev. Lett.*, 101:081801, 2008.

[77] N. E. Adam et al. A Study of Exclusive Charmless Semileptonic B Decay and $|V_{ub}|$. *Phys. Rev. Lett.*, 99:041802, 2007.

[78] C. Schwanda et al. Evidence for B+ $\rightarrow \omega$l+ν. *Phys. Rev. Lett.*, 93:131803, 2004.

[79] F. De Fazio and M. Neubert. B $\rightarrow$ X_u l anti-nu_l decay distributions to order alpha(s). *JHEP*, 06:017, 1999.

[80] E. Dalgic et al. B meson semileptonic form factors from unquenched lattice QCD. *Phys. Rev.*, D73:074502, 2006.

[81] D. Cote. Reweighting of the form factors in exclusive b $\rightarrow$ x l nu decays. Internal BABAR Analysis Document #809, 2004.

[82] B. Aubert et al. Measurement of the B0 $\rightarrow$ pi- l+ nu form-factor shape and branching fraction, and determination of |V(ub)| with a loose neutrino reconstruction technique. *Phys. Rev. Lett.*, 98:091801, 2007. See also arXiv:hep-ex/0607060.

[83] R. J. Hill. Heavy-to-light meson form factors at large recoil. *Phys. Rev.*, D73:014012, 2006.

[84] P. Ball and G. W. Jones. B$\rightarrow$eta$^{(\prime)}$ form factors in QCD. *JHEP*, 08:025, 2007.

[85] D. Scora and N. Isgur. Semileptonic meson decays in the quark model: An update. *Phys. Rev. D*, 52:2783, 1995.

[86] B. Aubert et al. Study of $B \rightarrow \pi\ell\nu$ and $B \rightarrow \rho\ell\nu$ decays and determination of $|V_{ub}|$. *Phys. Rev.*, D72:051102, 2005.

[87] C. Anders, C. Langenbruch, J. Dingfelder, and U. Uwer. Measurement of the $b^+ \rightarrow \omega\ell^+\nu$ and $b^+ \rightarrow \eta\ell^+\nu$ branching fractions using neutrino reconstruction. Internal BABAR Analysis Document #2007, 2008.

[88] R. Barlow et al. Recommended statistical procedures for *BABAR*. BABAR Analysis Document #318, Accessed Apr 2012 at http://www.slac.stanford.edu/BFROOT/www/Statistics/Report/report.pdf.

[89] R. Barlow. A calculator for confidence intervals. *Comput. Phys. Commun.*, 149:97, 2002.

[90] G. J. Feldman and R. D. Cousins. A Unified approach to the classical statistical analysis of small signals. *Phys. Rev.*, D57:3873, 1998.

[91] G. D. Thomas and B. Ghulum. Solving multiclass learning problems via error-correcting output codes. *J. Artif. Intell. Res. (JAIR)*, 2:263, 1995.

[92] B. Aubert et al. Angular distributions in the decays $B \rightarrow K^*\ell^+\ell^-$. *Phys. Rev.*, D79:031102, 2009.

[93] M. Bona et al. SuperB: A high-luminosity asymmetric e+ e- super flavor factory. Conceptual design report. arXiv:0709.0451 [hep-ex], 2007.

[94] B. Golob. Super KEKB / Belle II project. *Nuovo Cim.*, C33:319, 2010.